A STATISTICAL-DYNAMICAL STUDY OF THE LARGE-SCALE INTRASEASONAL VARIABILITY OF THE NORTHERN HEMISPHERE WINTER CIRCULATION

by
Siegfried D. Schubert

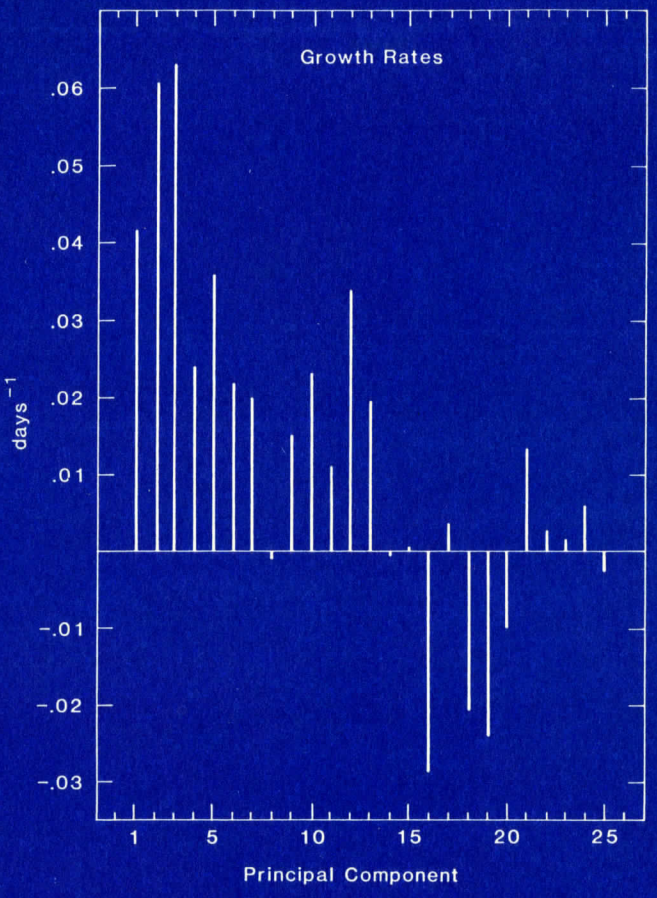

Scientific Report #3
June, 1983

The research reported here has been supported by NASA grant NSG-5223

Gerald F. Herman
Principal Investigator

Department of Meteorology
University of Wisconsin—Madison
1225 W. Dayton St.
Madison, Wisconsin 53706

Department of Meteorology

University of Wisconsin-Madison

Madison, Wisconsin 53706

A STATISTICAL-DYNAMICAL STUDY OF THE LARGE-SCALE INTRASEASONAL VARIABILITY OF THE NORTHERN HEMISPHERE WINTER CIRCULATION

by

Siegfried D. Schubert

Scientific Report #3

June, 1983

Support for this work was provided by the National Aeronautics and Space Administration under Grant NSG-5223

Gerald F. Herman, Principal Investigator

FOREWARD

A principal goal of general circulation modeling has been the prediction of atmospheric flow anomalies over time periods ranging from several weeks to a season or more. Recent work, both observational and theoretical, has suggested that in fact there may exist certain classes of flows which may be more potentially predictable than others. Ideally, an increased understanding of the nature of these special flows will aid in their numerical modeling, and aid in the definition of observational data requirements. These, hopefully, would lead to an enhanced predictive capability.

Our ongoing research in this area has focused on the applications of the general circulation models used at NASA's Goddard Laboratory for Atmospheric Science. As part of this effort, Dr. Siegfried Schubert has undertaken a detailed observational and theoretical study of large-scale atmospheric flow anomalies. The following report, which contains the Ph.D. thesis research of Dr. Schubert, describes an attempt to represent the structure of the anomalies in terms of empirical orthogonal functions (EOFs), and determine stability of the EOF's and their correspondence to actually-occurring structures.

The research described herein was funded under NASA grant NSG-5223, "The effect of synoptic scale processes in GCM modeling," and relied heavily upon the computational resources provided by the Modeling and Simulation Branch of Goddard's Laboratory for Atmospheric Science (GLAS). We are indebted to Dr. M. Halem and the staff of that branch for their dedicated support of this research.

Gerald F. Herman
Associate Professor
1 June 1983

A STATISTICAL-DYNAMICAL STUDY OF THE LARGE-SCALE INTRASEASONAL VARIABILITY OF THE NORTHERN HEMISPHERE WINTER CIRCULATION

Siegfried Dieter Schubert

ABSTRACT

The observed wintertime intraseasonal variability of the Northern Hemisphere mid-tropospheric circulation is analyzed using a combined statistical and dynamical approach. The statistical analysis is based on an empirical orthogonal function (EOF) expansion of the 500 mb streamfunction anomalies (deviations from the climatological seasonal cycle) and includes a description and interpretation of the dominant modes. The dynamical analysis involves entering these modes into an equivalent barotropic model in an attempt to gain further insight into the important dynamical processes governing their behavior. The importance of the terms involving boundary parameterizations is determined from a least squares fit.

A major result of this study is the identification

of the zonally varying wintertime mean flow as a potentially important energy source for some of the dominant EOF's: these include the first three EOF's which are associated with a range of behavior encompassing an index cycle, the Pacific/North American pattern, and the North Atlantic oscillation.

Nonlinear aspects of the model were also investigated and these include the interaction between EOF's, the stability of base states involving fixed EOF's, and multiple equilibria. The strongest interactions were found to involve the second and ninth EOF's. The latter is associated with North Atlantic blocking and the former is associated with fluctuations in the North American east coast jet. The North Atlantic blocking mode was found to be very unstable as a result of interactions with the dominant EOF's which act to destroy this pattern.

A comparison with spatially and temporally uncorrelated noise suggests that the first twelve principal components (PC's) are significant; however, the limited temporal extent of the data allows only a marginal resolution of the individual modes.

A study of very low order models (without orography) shows that, while multiple equilibria are possible, they

are generally found for parameter values associated with unrealistically weak decay rates and/or unrealistically strong forcing. In the present model blocking is most likely to occur as a quasi-linear response to the inhomogeneous forcing which enters into the model as a residual calculation due to the fact that the mean flow, by itself, does not satisfy the vorticity equation.

TABLE OF CONTENTS

LIST OF FIGURES

LIST OF TABLES

LIST OF SYMBOLS AND ABBREVIATIONS

General

λ	longitude
ϕ	latitude
r	(λ, ϕ)
p	pressure
ρ	density (also correlation in section 2.3)
t	time
ψ	stream function
χ	velocity potential
Φ	geopotential
ω	pressure vertical velocity (dp/dt)
w	vertical velocity (dz/dt)
h	height of the Earth's surface
Y_n^m	spherical harmonic with zonal wave number m and total wave number n
γ	(n_γ, m_γ), similarly for α, β and δ
c_γ	$n_\gamma(n_\gamma + 1)$
ψ_γ	spectral coefficient of the stream function expansion
$E_i(\lambda, \phi)$	the ith empirical orthogonal function (EOF)
$e_i(\gamma)$	the ith EOF in the wave domain
$z_i(t)$	the ith principal component (PC)
λ_i	the eigenvalue associated with the ith EOF

δ_{ij}	Kronecker delta function
A(p)	vertical structure function
f	coriolis parameter (sin ϕ)
g	gravity (9.80 m/sec^2)
a	mean radius of the Earth (6365 km)
Ω	angular speed of the Earth's rotation (2π/day)
< >	ensemble or time average
[ ]	vertical average
$(\bar{\ })$	complex conjugate
$(\ )^T$	transpose or complex conjugate transpose
∇	gradient
∇^2	Laplacian
J	Jacobian
$\tilde{(\ )}$	denotes a vector
$(\dot{\ })$	denotes a time derivative d/dt( )
T	a unitary matrix
$\ddagger$	a covariance matrix
KE	kinetic energy
MSV	mean square velocity
ENS	enstrophy
ZWN	zonal wave number
RHS	right hand side
LHS	left hand side
PBL	planetary boundary layer

The EOF model

a_{kj}	coefficients involved in the tendency, dissipation and MSV formulation (A in matrix notation)
b_{kj}	coefficients involved in the ENS formulation
u_{kj}	coefficients involved in the long wave correction formulation
d_{kji}	EOF interaction coefficients
rl_{kj}	coefficients involved in the advection of mean flow vorticity by the anomalous wind term (Rl in matrix notation)
$r2_{kj}$	coefficients involved in the mean flow advection of the anomalous vorticity term (R2 in matrix notation)
r_{kj}	$rl_{kj} + r2_{kj}$ (R in matrix notation)
f_{kj}	coefficients involved in the orography term
g_{kj}	coefficients involved in the beta term (G in matrix notation)
p_{kj}	$a_{kj} - r_{kj} - g_{kj}$ (P in matrix notation)
z^*_k	the inhomogeneous forcing (S) projected onto the EOF's
H*	a scale height parameter
N	long wave correction parameter
M	a/H*
$(1 + \varepsilon)$	a lower boundary correction factor involving the beta term
κ	the frictional decay rate
α	forcing strength

1. INTRODUCTION

A key aspect of the extended range predictability problem concerns the difficulties encountered in the prediction of the large-scale slowly varying features which typically dominate the middle latitude circulation. In a recent review of the progress made in medium range numerical weather forecasting, Bengtsson (1981) noted that significant improvement may come from a reduction of the systematic errors involved in predicting the large-scale quasi-stationary flow. Vital to such error reduction is a better understanding of both the spatial structure of these flows and the mechanisms which produce and maintain them.

A number of recent theoretical and observational studies have either directly or indirectly contributed to prospects for improved extended range forecasts by providing a clearer insight into the nature of the large-scale intraseasonal variations of the atmosphere. Observational studies have emphasized the identification and description of coherent hemispheric, as well as near global scale modes of variability, while theoretical studies have focused on the nature of the processes governing their behavior.

Using a 15 year NMC data set consisting of monthly

mean sea level pressure and 500 mb height analyses, Wallace and Gutzler (1981) found strong support for teleconnections (measured by mid-tropospheric spatial correlations) involving the North Atlantic Oscillation and Pacific/North American patterns. The former is characterized by fluctuations in the western Atlantic mean jet and the latter involves an alternation between a high amplitude wave structure and a more zonal flow over the North Pacific and North America. These modes were found to have a predominantly equivalent barotropic structure. A study by Weickmann (1982) using winter NMC analyzed circulation fields (85°N - 30°S) and satellite-derived outgoing longwave radiation fields found evidence for near global scale oscillations characterized by an index cycle involving the middle latitude and subtropical jet streams of both hemispheres. In a study of recurring anomalies in a 15 year GFDL model simulation, Lau (1981) found strong similarities between the dominant winter modes of variability of the model simulation and observations. The simulation did not allow nonseasonal perturbations in the prescribed model forcing, yet substantial variability was found on monthly time scales.

Much of the theoretical work concerning large-scale low-frequency variability has centered on barotropic

dynamics. Charney and DeVore (1979) showed the existence of multiple equilibria in a low order barotropic channel model with orography and a barotropic analogue to thermal driving. Crucial for the existence of large amplitude equilibria is linear resonance of a stationary Rossby wave in the presence of orography. Källén (1981) extended these results to the sphere and showed that a properly placed wave vorticity source could increase the efficiency of producing multiple equilibria.

Lorenz (1972) examined the stability of Rossby waves on a β-plane. His results showed that for sufficiently small wave lengths and large amplitudes the waves were barotropically unstable, and Lorenz postulated that this may be the primary cause of the unpredictability of the atmosphere. Baines (1976) examined the stability of free planetary waves on the sphere and found that all waves with total wave number greater than 2 are unstable if their amplitudes are large enough. For zonal flows the critical amplitudes are close to those obtained by Rayleigh's criterion; whereas, for some of the traveling waves the critical amplitudes are approximately those obtained from triad interactions.

Simmons et al. (1982) examined a barotropic model linearized about the 300 mb climatological mean January

flow in their study of barotropic instability and teleconnections. Results showed that the structure of the responses to localized forcings in the tropics and subtropics were related to the most rapidly growing mode associated with barotropic instability of the zonally-varying base state. They further suggested that much of the low frequency variability of the Northern Hemisphere wintertime circulation derives its energy from the base state through barotropic instability.

In order to define more clearly the applicability and important processes of these simple models, Kruse (1983) performed a detailed statistical analysis of a spectral equivalent barotropic model. The model allowed a crude representation of baroclinic effects and an inhomogeneous term which was interpreted as a thermal forcing. Results of this study showed the equivalent barotropic model is capable of explaining a significant fraction of the large-scale variability, and emphasized the importance of the beta effect, wave/zonal flow and wave/wave interactions, and thermal forcing in the development of planetary waves. Furthermore, these results showed the orographic term to be less important, particularly for the zonally asymmetric modes. Friction was found to be practically negligible, and the effect of

the baroclinic modes, through the surface tendency term, led to almost dispersion-free Rossby speeds.

The present work involves a combined observational, statistical and modeling approach in an attempt to close the gap between some of the basically heuristic studies involving highly simplified models and the observational studies of the atmosphere. The main objective is to identify the important mechanisms responsible for the initiation and maintenance of the observed modes of variation within a dynamical framework. The first part of this work involves the identification and description of the dominant modes of variability of the extratropical atmosphere in terms of empirical orthogonal functions (EOF's). Subsequently, the EOF's are entered into an equivalent barotropic model, which in its basic form is similar to that in the Kruse (1983) study. However, the model used here does not explicitly include the effects of baroclinic modes or thermal processes. The model is formulated in terms of deviations from the climatological seasonal cycle, which enters into the anomaly equations via the advective terms and as a residual inhomogeneous forcing term.

Sellers (1957) was the first to formulate a dynamical model based on atmospheric EOF's. However,

predictions of the 500 mb anomaly field over a limited area, based on the barotropic vorticity equation, showed poorer results for the EOF model than for the standard barotropic model. Sellers pointed to difficulties in the evaluation of the prediction coefficients associated with the higher order derivatives as a possible reason for the poor results. More recently, Rinne and Karhila (1975) developed a similar limited area barotropic model which exhibited a forecast skill at least as good as the standard finite difference model. However, the model exhibited some rather strong spurious oscillations in an energy invariant, which were attributed to the level of EOF truncation.

The present study overcomes some of these difficulties by formulating the EOF's in the wave domain. This allows a significant simplification of the higher order derivative terms through the use of identities satisfied by the harmonic functions on a sphere. Analogous to the spectral form of the advective terms, interaction coefficients may be defined for the EOF's. Unlike the grid point formulation, the EOF's in the wave domain are governed by interactions which explicitly take into account the interaction rules of the spectral formulation. This allows for an analytic

analysis of the conservative properties of the truncated EOF model and provides a basis for making decisions concerning the proper model formulation.

2.0 DATA ANALYSIS AND INTERPRETATION

2.1. Description of the data

The data consist of twice daily 500 mb values of the streamfunction for the Northern Hemisphere for the ten year period beginning January 1, 1967 and ending December 31, 1976. The original data were provided by the Deutscher Wetterdienst (DWD) as geopotential heights on a rectangular grid (381 x 381 sq km at 60°N) analyzed for the area north of approximately 12.5° latitude. These data were converted to the spectral domain assuming symmetry with respect to the equator and employing triangular truncation at total wave number 16, by E. Kirk and P. Speth (Institut für Geophysik und Meteorologie in Köln). The geopotential coefficients were converted to streamfunction coefficients (odd harmonics) by Harald Kruse (1983) through the linear balance equation. The recurrence relation involved in this transformation uses a geostrophic constraint on the mean angular momentum to provide a starting point for the purely zonal modes. Extrapolation to the equator was done by assuming a constant value equal to the zonal average computed from the southernmost data points.

The orographic data consist of 5° longitude by 2.5° latitude values provided by E. Maier-Reimer (Max-Planck-

Institut für Meteorologie, Hamburg). This is a smoothed version of a 1° by 1° grid produced at the Geophysical Fluid Dynamics Laboratory. The orographic heights are normalized by the Earth's radius and converted to the spectral domain with even harmonics and triangular truncation at total wave number 16. A plot of the orography is presented in Figure 1. While there is a considerable amount of smoothing to the gridpoint data (not shown), the major land masses and mountain chains are reasonably well represented.

2.2. The empirical orthogonal functions

a) Theoretical background

Empirical orthogonal functions (EOF's) provide a very useful tool for the analysis of very large data sets. The data transformation associated with the dominant EOF's aligns the coordinate axes (defined by grid points or spectral coefficients) in the directions of greatest variability, allowing for a very efficient representation of the data. One of the disadvantages of EOF's (particularly when based on gridded data) is their lack of a well defined functional form and the associated difficulty in dealing with them in mathematical equations. In the present study this limitation is in part overcome

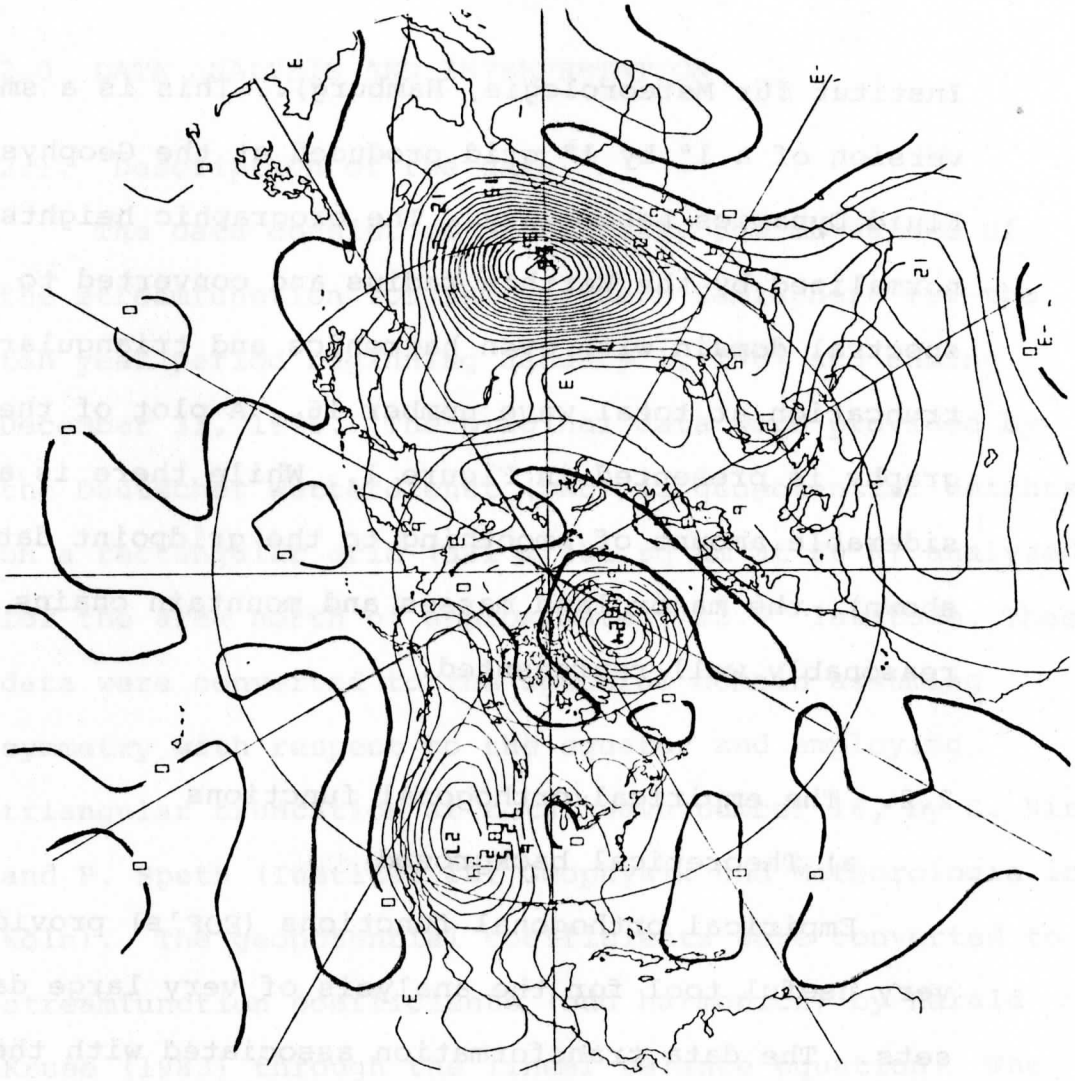

Figure 1. The orography (normalized by the Earth's radius) based on a spherical harmonic expansion with triangular truncation at total wave number 16 assuming symmetry with respect to the equator. Units: non-dimensional, contour interval is 3×10^{-5}. Heavy contours are the zero lines.

by formulating the EOF's in the spectral domain and using spherical harmonic identities in order to simplify the mathematical expressions.

The various properties of EOF's have been discussed in detail in previous studies (e.g. Kutzbach (1967), Davis (1976), North et al. (1981)). Here only the properties pertinent to the present study will be briefly reviewed. The discussion will follow the development of North et al. for a continuous two-dimensional field in order to show more clearly the relationship between EOF's in the wave domain and EOF's in physical space.

The EOF analysis summarizes the information contained in the data in terms of the covariance function, C, defined as

$$C(\underset{\sim}{r},\underset{\sim}{r}',t) = \langle \psi(\underset{\sim}{r},t)\psi(\underset{\sim}{r}',t) \rangle \qquad (2.2.1)$$

where the angular brackets represent an ensemble average and ψ is a continuous two-dimensional field (e.g. streamfunction) referenced by position $\underset{\sim}{r}$ and time t. It is assumed that $\langle \psi(\underset{\sim}{r},t) \rangle = 0$. The basis functions are the eigenfunctions (E_i) of the integral equation

$$A^{-1} \int_A C(\underset{\sim}{r},\underset{\sim}{r}',t) E_i(\underset{\sim}{r}',t) d\underset{\sim}{r}' = \lambda_i(t)\ E_i(\underset{\sim}{r},t) \qquad (2.2.2)$$

where A defines the domain of integration and the λ_i are the eigenvalues. An important property of the eigenfunctions (EOF's) is the dual orthogonality

$$A^{-1} \int_A E_i(\underset{\sim}{r},t)\, E_j(\underset{\sim}{r},t)\, d\underset{\sim}{r} = \delta_{ij} \qquad (2.2.3a)$$

and

$$\sum_{i=1}^{\infty} E_i(\underset{\sim}{r},t)\, E_i(\underset{\sim}{r}',t) = \delta_{\underset{\sim}{r}\underset{\sim}{r}'} \qquad (2.2.3b)$$

The latter property is of particular importance in the present study for the investigation of the EOF model's integral constraints (see 3.2b). (2.2.3) insures that the E_i form a basis set and

$$\psi(\underset{\sim}{r},t) = \sum_{i=1}^{\infty} z_i(t)\, E_i(\underset{\sim}{r},t) \qquad (2.2.4a)$$

where the z_i are the coefficients of the EOF's and are called principal components (PC's) given by

$$z_i(t) = A^{-1} \int_A E_i(\underset{\sim}{r},t)\, \psi(\underset{\sim}{r},t)\, d\underset{\sim}{r} \qquad (2.2.4b)$$

Additional properties are: the orthogonality of the PC's

$$\langle z_i \, z_j \rangle = \lambda_i \, \delta_{ij} \tag{2.2.5}$$

where $\langle z_i \rangle = 0$; the total (or mean) variance relation

$$A^{-1} \int_A \langle \psi^2 \rangle \, d\underset{\sim}{r} = \sum_{i=1}^{\infty} \lambda_i \tag{2.2.6a}$$

and the local variance given by

$$\langle \psi^2(\underset{\sim}{r},t) \rangle = \sum_{i=1}^{\infty} \lambda_i E_i^2(\underset{\sim}{r},t) \tag{2.2.6b}$$

Since the variance associated with the ith PC is λ_i, the fraction of the total variance represented by this mode is the ratio of this eigenvalue to the sum of the eigenvalues. A very useful property of the PC's is that, when ordered by the amount of variance explained, they are the most efficient representation of the data in the sense that for a given subset of the expansion, no other set of basis functions can explain a greater fraction of the total variance. Another property, not often mentioned in the meteorological literature, concerns the correlation between ψ and the PC's and is given as

$$\rho(\psi, z_i) = E_i \, \lambda_i^{\frac{1}{2}} \langle \psi^2 \rangle^{-\frac{1}{2}} \tag{2.2.7}$$

This property becomes more useful when treated in the wave domain (cf. 2.3.2).

In practice the ensemble averages are replaced by time averages under the assumption of stationarity (see 2.2b). Then the eigenfunctions and eigenvalues in (2.2.1) - (2.2.7) lose their time dependence. Furthermore, one usually does not deal with continuous functions. In the case of grid point data, (2.2.2) must be approximated by finite differences, and North et al. (loc. cit.) has discussed the proper scaling for spherical geometry. For the present study the data are expanded in spherical harmonics

$$\psi(\underset{\sim}{r},t) = \sum_{\gamma} \psi_{\gamma}(t)\, Y_{\gamma}(\underset{\sim}{r}) \qquad (2.2.8)$$

where the Y_{γ} are spherical harmonics (see 3.1c) with zonal wave number m and total wave number n and the ψ_{γ} are the spectral coefficients. The spectral expansion of E_i is then

$$E_i(\underset{\sim}{r}) = \sum_{\gamma} e_i(\gamma)\, Y_{\gamma}(\underset{\sim}{r}) \qquad (2.2.9)$$

where $e_i(\overline{\gamma}) \equiv \overline{e}_i(\gamma)$; the bar indicates a complex conjugate and $\overline{\gamma} = (n_{\gamma}, -m_{\gamma})$. Substituting (2.2.8) and

and (2.2.9) into (2.2.2) leads to the spectral EOF eigenvalue problem

$$\sum_{\gamma} \langle \bar{\psi}_{\gamma} \psi_{\beta} \rangle e_i(\gamma) = \lambda_i e_i(\beta) \qquad (2.2.10)$$

where*

$$e_i(\gamma) = A^{-1} \int_A \bar{Y}_{\gamma}(\underset{\sim}{r}) E_i(\underset{\sim}{r}) d\underset{\sim}{r} \qquad (2.2.11)$$

The $e_i(\gamma)$ are the complex EOF's in the wave domain. The spectral versions of the properties (2.2.3) - (2.2.7) may be obtained by substitution of (2.2.8) and (2.2.9). In particular, (2.2.3) becomes

$$\sum_{\gamma} \bar{e}_i(\gamma) e_j(\gamma) = \delta_{ij} \qquad (2.2.12a)$$

and

$$\sum_{i} \bar{e}_i(\gamma) e_i(\beta) = \delta_{\gamma\beta} \qquad (2.2.12b)$$

(2.2.4) becomes

$$\psi_{\gamma}(t) = \sum_{i} z_i e_i(\gamma) \qquad (2.2.13a)$$

and

---

*In practice the $e_i(\gamma)$ are computed from (2.2.10).

$$z_i(t) = \sum_{\gamma} \bar{e}_i(\gamma)\psi_\gamma \qquad (2.2.13b)$$

A schematic view of the various data transformations involved in this study is shown in Figure 2. The actual data field is assumed to be continuous and exhibits variations characterized by the covariance function (A) defined in (2.2.1). The spectral expansion of the data leads to covariance relationships defined by an infinite dimensional matrix (B) involving covariances between the spectral coefficients. In practice, the spectral expansion is based on gridded data and is limited to a finite number of harmonics leading to the finite dimensional covariance matrix (C). The spectral representation is ordered by spatial scale and therefore provides a natural choice for truncation based on the spatial resolution desired or obtainable from an observational network. The fact that a wave expansion involving just a few hundred modes or less provides a very good representation of the large-scale atmospheric fields is in large part due to the observed tendency for the motions to be wave-like. The spectral representation implicitly takes into account the spatial covariances associated with wave motions, allowing for a large reduction in the number of degrees of freedom.

DATA TRANSFORMATIONS AND COVARIANCES

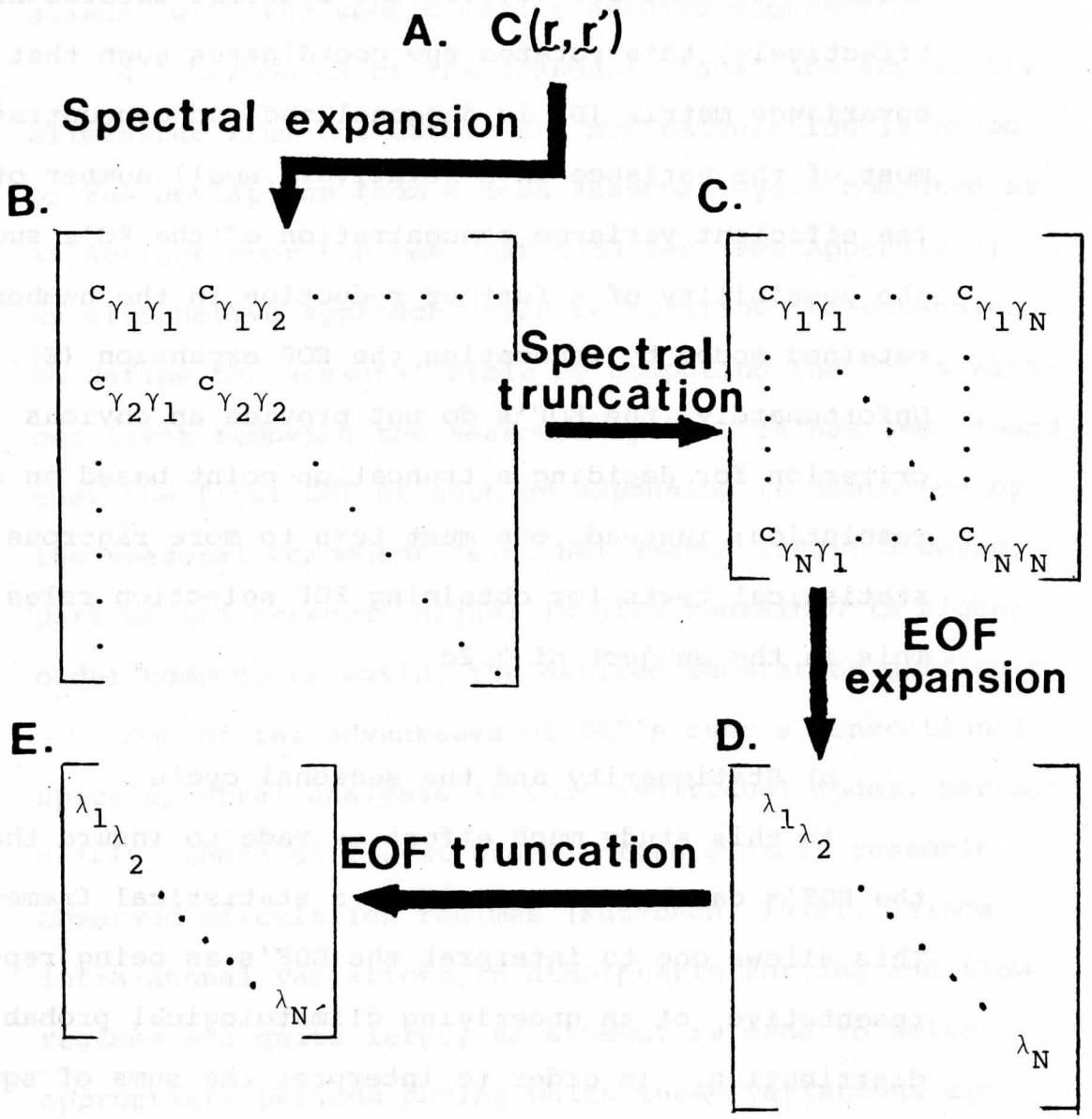

Figure 2. A schematic view of the data transformations and expansion truncations as they are reflected in the covariance function (see text for details).

The EOF expansion, in turn, takes into account the observed covariances between the spectral coefficients. Effectively, this rotates the coordinates such that the covariance matrix (D) is diagonalized and concentrates most of the variance in a relatively small number of modes. The efficient variance concentration of the PC's suggests the possibility of a further reduction in the number of retained modes by truncating the EOF expansion (E). Unfortunately, the EOF's do not provide an obvious criterion for deciding a truncation point based on spatial resolution; instead, one must turn to more rigorous statistical tests for obtaining EOF selection rules. This is the subject of 2.2c.

b) Stationarity and the seasonal cycle

In this study much effort is made to insure that the EOF's can be treated within a statistical framework. This allows one to interpret the EOF's as being representative of an underlying climatological probability distribution. In order to interpret the sums of squares and cross products of the data as variances and covariances, each year is assumed to be a realization of a stationary stochastic process. Stationarity is achieved by removing the seasonal cycle (with the first

moment a constant) and limiting the analysis to one season (with the second moment assumed constant).

All harmonics of the seasonal signal are explicitly eliminated from the data: the EOF calculation is based on the deviations from a mean seasonal cycle computed as an average over the ten year data set (see Appendix A). An alternative approach would be to allow the expansion to define the seasonal cycle by computing the EOF's without first removing the seasonal cycle. It has been found that the first EOF of such an expansion is dominated by the seasonal component (e.g. Weickmann, 1982); however, part of the seasonal signal is also contained in higher order components making the desired separation difficult.

One of the advantages of EOF's over a conventional space spectral analysis is that individual modes, particularly those of lowest order, often closely resemble observed circulation regimes (Kutzbach, 1970). Since intra-annual variations in atmospheric forcing and flow regimes are quite large, an attempt is made to select appropriate periods during which these variations are minimized. The consequence of such a selection should be to enhance the physical interpretation of the EOF's. The concept of a "natural" calendar dividing the year into segments of similar weather patterns which change

abruptly (rather than slowly following the gradual change in solar radiation) was studied by Bryson and Lahey (1958). Their study supported the idea that there are statistically similar flow regimes separated by abrupt changes in circulation patterns, allowing for the definition of a "natural" calendar of seasons. Using these results as a guide the present definition of the seasons is based primarily on the variations of the m = 0 (zonal) flow components which seem most closely linked to variations in solar radiation and are the major contributors to the seasonal cycle. The winter season (Dec. 2 - March 31 as compared with Nov. 1 - March 21 for the Bryson study), which is the focus of this study, is chosen in an effort to minimize the variations of these components.

c) Expansion truncation

The higher frequency modes associated with day to day weather variations are filtered from the expansion by computing the EOF's from 10-day averages of the stream function anomalies. Details of the EOF calculations and the relationship between the real and complex representations are given in Appendix A. A major advantage of an EOF representation is the efficiency with which it is

capable of reconstructing the variance of a data set (see 2.2a). Figure 3 (large dots) shows the percent variance explained by each PC of the observations on a semi-logarithmic plot. The first PC explains 16% of the observed variance. The first 25 PC's explain about 92% and the first 40 PC's explain more than 97% of the observed variance in the 10 day averaged streamfunction anomalies. This plot suggests that very little additional information is gained by including more than say the first 25 modes since more than 100 modes are required to explain the remaining 8% of the observed variance.

In order to make a more objective assessment of the EOF representation and provide a framework for making decisions concerning truncation of the EOF expansion it is necessary to develop more rigorous statistical tests concerning the nature of the noise and information signal in the data. Preisendorfer et al. (1981) have developed an extensive set of statistical tests designed to provide a criterion for EOF truncation. The test used for this study is one of the dominant variance rules (rule N) developed by Preisendorfer et al. under the assumption that all the useful information is contained in the modes with the greatest variability. The null hypothesis is that the eigenvalues come from spatially and temporally

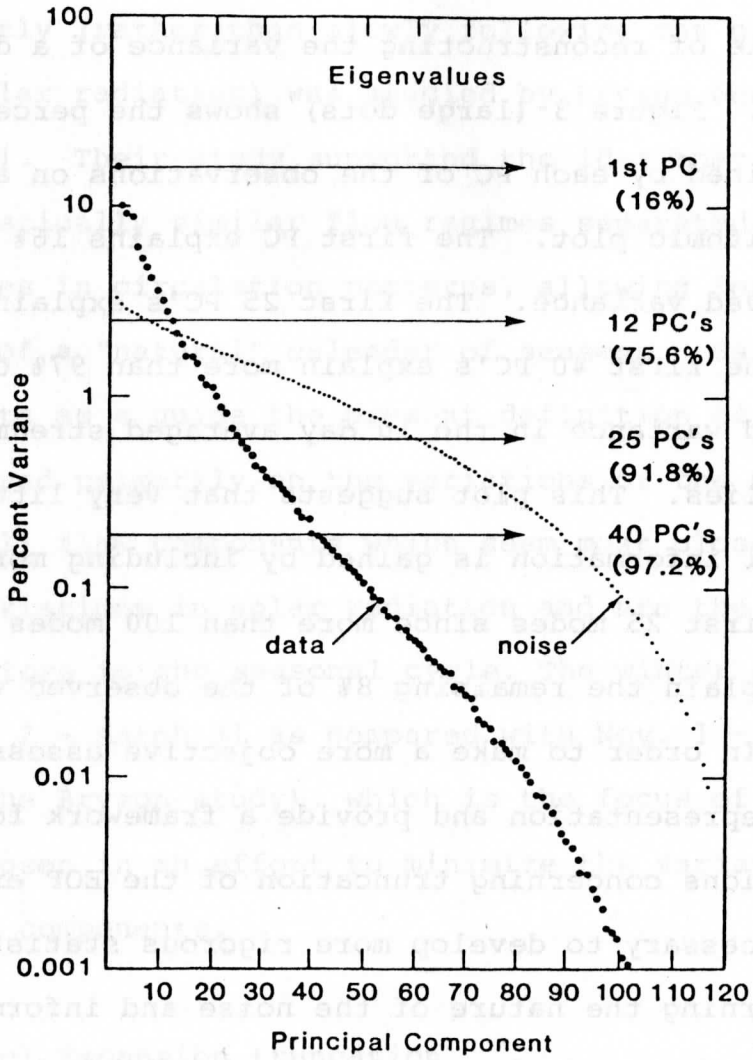

Figure 3. The percent variance explained for the PC's computed from the observations (large dots) and a simulated noise process (small dots). For the noise, the values are the upper 5% points on a cumulative distribution of the normalized eigenvalues. The values in parentheses are the cumulative variances explained by the data PC's.

uncorrelated noise, and only those modes are retained which have eigenvalues larger than the noise process. The computations involve Monte Carlo simulations of the noise process with sample size (P) and dimension (N) identical to those for the data eigenvalue calculations (P = 120, N = 135).

In order to generate realizations from a Gaussian probability distribution in N-space with a known covariance matrix, $\ddagger$, one need only generate N × P independent Gaussian variates, $u_n(p)$, with 0 mean and unit variance arranged in P vectors of length N. The realizations are then given by

$$\underset{\sim}{x}(p) = \sum_{n=1}^{N} \sigma_n^{\frac{1}{2}} u_n(p) \underset{\sim}{g}_n , \quad p = 1,2...,P \qquad (2.2.14)$$

where σ_n and $\underset{\sim}{g}_n$ are the eigenvalues and eigenvectors of $\ddagger$, respectively. As shown by Preisendorfer *et al.* (*loc. cit.*), these realizations have a sample covariance matrix which has an expected value of $\ddagger$. The spectral criteria for spatial white noise on the sphere is (see North and Cahalan, 1981)

$$\langle \psi_\gamma \bar{\psi}_\beta \rangle = \sigma \delta_{\gamma\beta} \qquad (2.2.15)$$

where ψ_γ are the coefficients of the spherical harmonic expansion and σ is independent of γ. Therefore, for the present study $\underset{\sim}{\Sigma} = \sigma I$ and (2.2.14) may be reduced to

$$\underset{\sim}{x}(p) = \sigma^{\frac{1}{2}}(u_1(p), u_2(p), \ldots, u_N(p))^T \qquad (2.2.16)$$

The noise and data eigenvalues are each normalized by the sum of the eigenvalues to eliminate the dependence on the unknown magnitude of the noise variance. Confidence intervals for the noise eigenvalues are constructed from 100 noise simulations and compared to the data eigenvalues. The upper 5% points on the cumulative distribution of the noise process* (small dots in Figure 3) superimposed on the normalized (percent variance) data eigenvalues suggests that approximately the first 12 PC's have variability significantly larger than would be expected from a noise process. These modes together explain about 76% of the observed variance.

2.3. Description and interpretation of the dominant EOF's

c) Mean energy spectrum

To the extent that the EOF's are estimates of the true climatological modes of variability exhibited by

*Note that as P/N becomes large, one would expect the noise curve to become approximately horizontal.

the atmosphere, a thorough analysis of the structures of the dominant EOF's should provide insight into the nature of preferred modes of the Northern Hemisphere winter circulation. While there is a significant amount of sampling error involved in the EOF's (see 2.3c), it is nevertheless of value to document the characteristics of the dominant EOF's since this will be helpful for understanding the modeling results of chapters 3 and 4.

A straightforward method of analyzing the EOF structures is simply to examine their spectral weighting. Such an analysis is done here for the first 12 EOF's in the context of the time and spatial mean kinetic energy (KE) together with a description of the hemispheric maps of the anomaly patterns. The time and spatial mean square nondivergent velocity (MSV) of the anomalies in non-dimensional form is given by (see 3.2b)

$$\langle MSV \rangle = \sum_k a_{kk} \lambda_k \qquad (2.3.1a)$$

where

$$a_{kk} = \sum_\gamma c_\gamma \bar{e}_k(\gamma)\, e_k(\gamma) \qquad (2.3.1b)$$

and $c_\gamma = n_\gamma(n_\gamma + 1)$. Here λ_k is the variance of the kth

PC and $a_{kk}\lambda_k$ is the fraction of the MSV of the anomalies associated with the kth PC. Furthermore, $c_\gamma \bar{e}_k(\gamma)\ e_k(\gamma)$ is the fraction of the kth PC MSV associated with spectral component γ. The anomalies account for approximately 24% of the total mean KE.

For each EOF, graphs of the percent mean KE as a function of m (zonal wave number, ZWN) and meridional wave number index (n - m) are presented along with the corresponding anomaly flow patterns. In addition, the individual wave contributions are presented in tabular form. The percentages are based on a total of 40 PC's. The meridional structure of Y_n^m for various values of n - m for the case m = 0 is shown schematically in Figure 4. The index n - m denotes the number of zeros of the meridional structure between the North and South Poles.

The first EOF (5a-b) accounts for about 10% of the mean KE of the anomalies and is dominated by zonal wave numbers 0 and 2 and meridional indices 3, 5, and 7. The most important spectral contributions come from Y_7^0 and Y_7^2. The meridional structure of the zonally symmetric component (see Figure 4) suggests a coupling between high and low latitude wind changes which act in opposition to changes in the middle latitude zonal wind. The spatial pattern of EOF 1 shows the largest zonal anomaly occurs

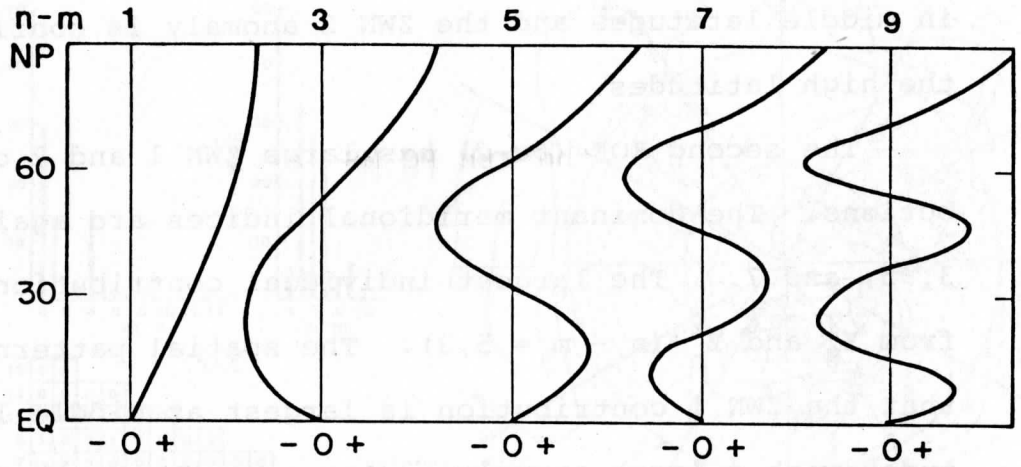

Figure 4. A schematic of the meridional structure of the spherical harmonics for various values of n - m with m = 0.

in middle latitudes and the ZWN 2 anomaly is confined to the high latitudes.

The second EOF (5c-d) has large ZWN 1 and 2 contributions. The dominant meridional indices are again 3, 5, and 7. The largest individual contributions come from Y_8^1 and Y_n^2 (n - m = 5,3). The spatial pattern shows that the ZWN 1 contribution is largest at middle latitudes with a large anomaly center over the North Atlantic. The high latitudes show a more pronounced ZWN 2.

The third EOF (6a-b) is dominated by ZWN's 1 and 3 and meridional indices 3 and 5. Important spectral contributions come from Y_6^1 and Y_6^3. The ZWN 1 pattern is most evident at high latitudes while the ZWN 3 pattern predominates in middle latitudes with large anomalies over the North Pacific, western North America and the western North Atlantic.

The fourth EOF (6c-d) has a zonal and meridional wave dependence similar to the third EOF. However, the individual spectral contributions show a smaller meridional scale for the fourth EOF, having dominant waves Y_8^1 and Y_8^3. The spatial pattern is dominated by a large anomaly over the Arctic extending into Asia and the Bering Sea.

The fifth EOF (7a-b) is predominatly made up of

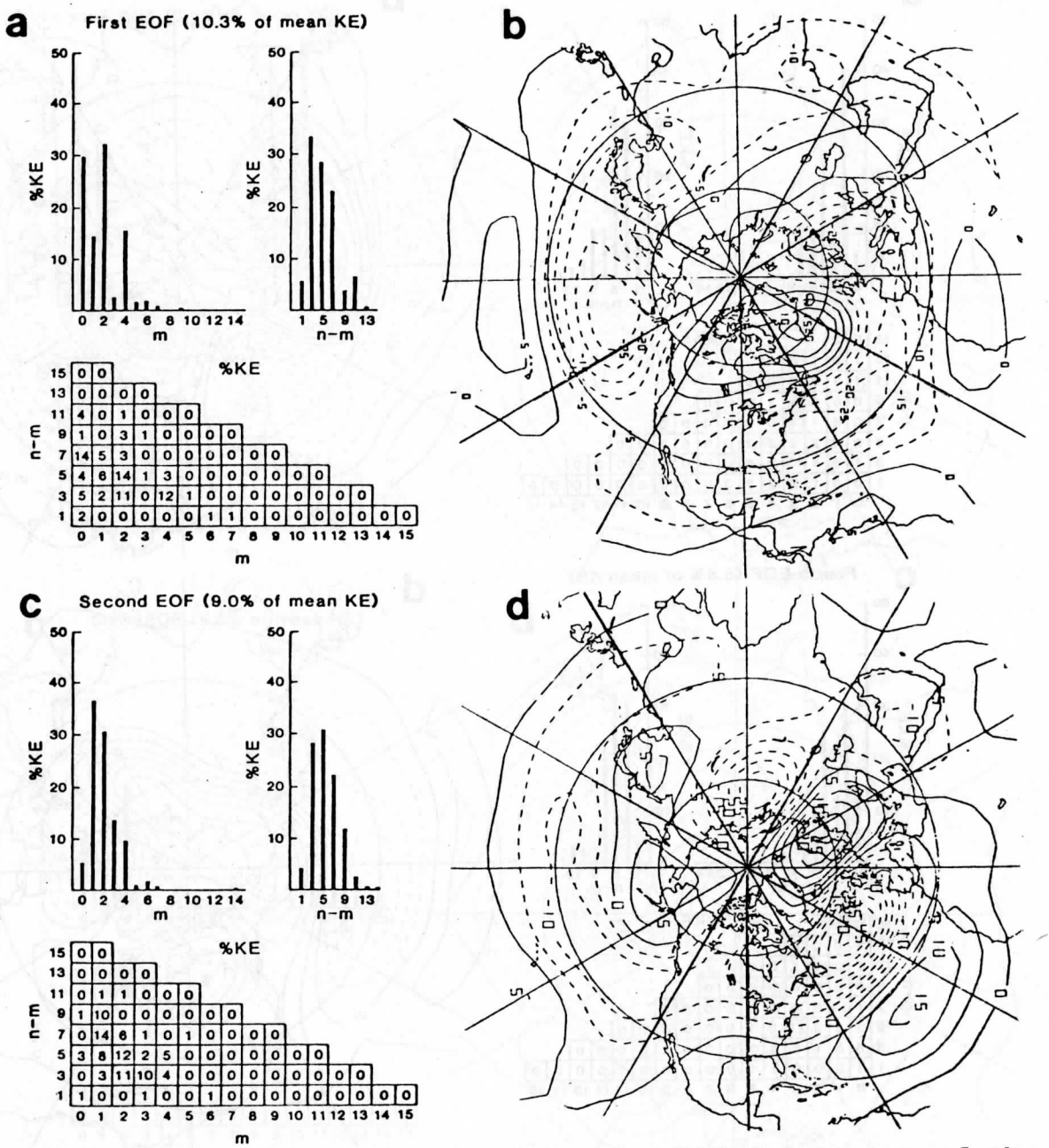

Figure 5. Spectral distribution and spatial patterns of the first two EOF's. The zonal dependence (m) obtained by summing over n, meridional dependence (n-m) obtained by summing over the appropriate n and m, and individual wave dependences are presented as a fraction of the mean anomaly KE associated with each EOF. EOF 1 (Fig.a-b) and EOF 2 (Fig. c-d) account for 10.3 and 9.0% of the total mean anomaly KE, respectively. The stream function is non-dimensional and the EOF's are normalized such that the squared values integrate to 4π. Contour interval is 5×10^{-1}.

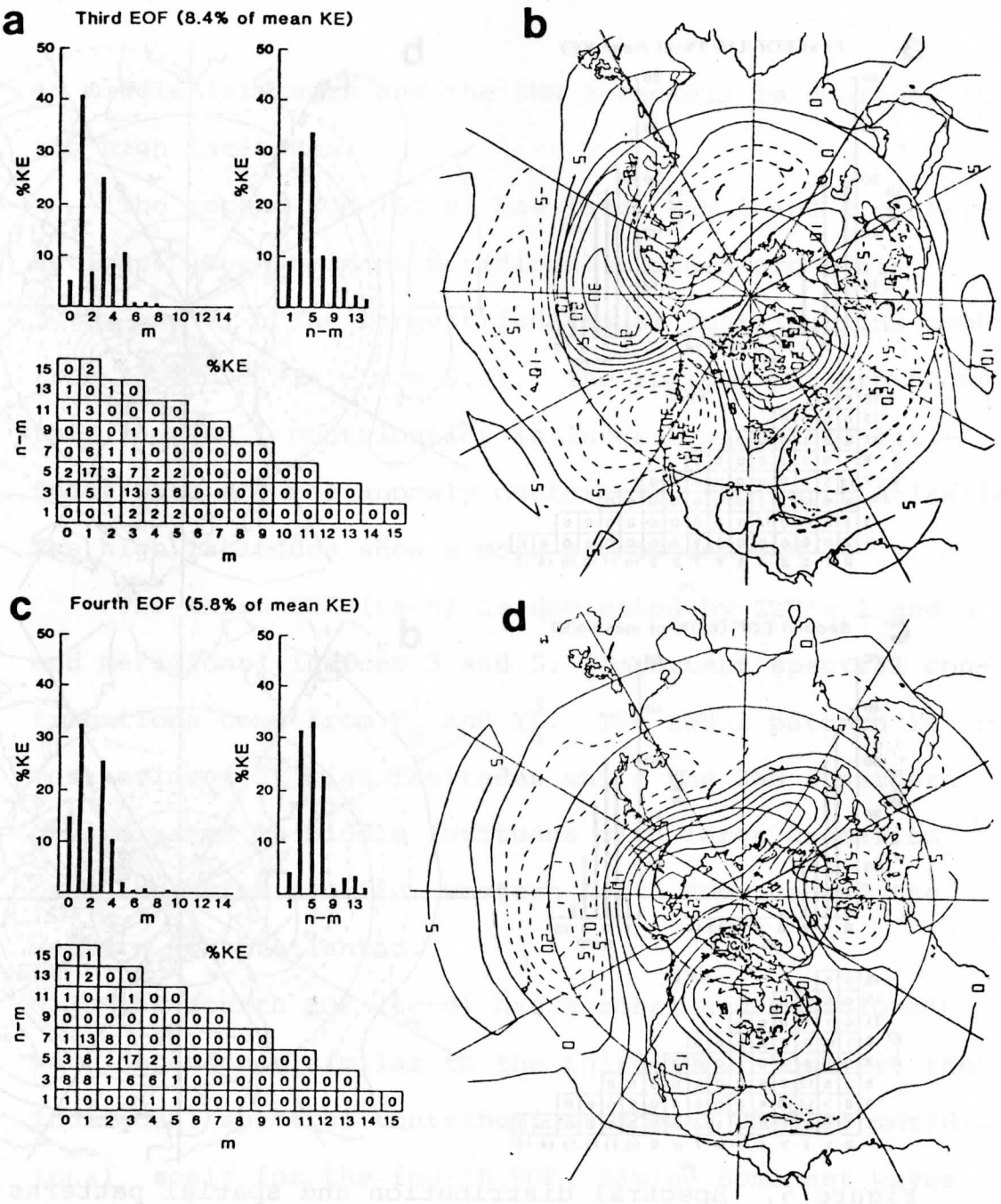

Figure 6. As in Fig. 5, except for the third and fourth EOF's which account for 8.4 and 5.8% of the total mean anomaly KE, respectively.

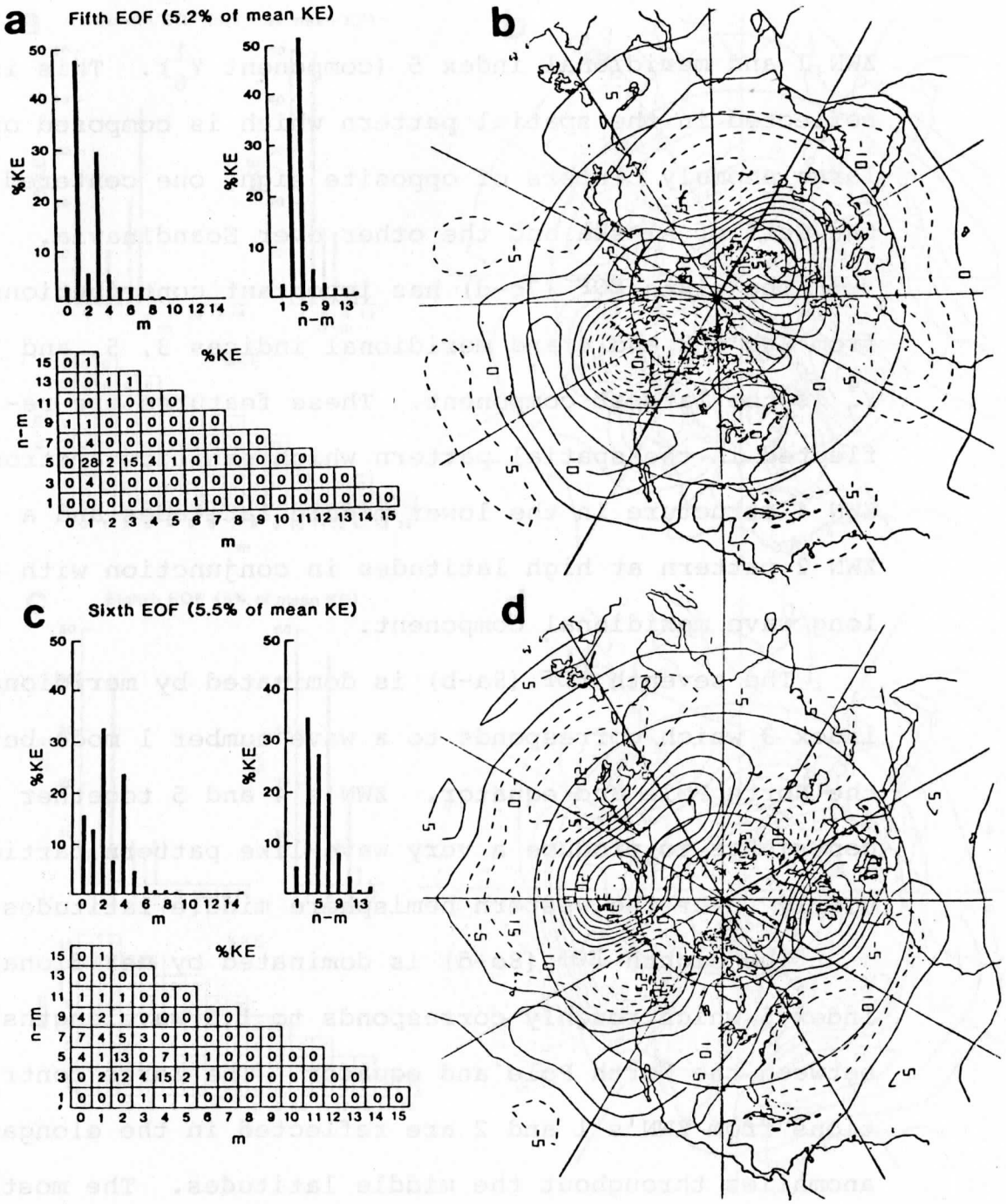

Figure 7. As in Fig. 5, except for the fifth and sixth EOF's which account for 5.2 and 5.5% of the total mean anomaly KE, respectively.

ZWN 1 and meridional index 5 (component Y_6^1). This is reflected in the spatial pattern which is composed of 2 large anomaly centers of opposite sign, one centered over the Gulf of Alaska and the other over Scandinavia.

The sixth EOF (7c-d) has important contributions from ZWN's 2 and 4 and meridional indices 3, 5, and 7. Y_7^4 is the largest component. These features are reflected in the spatial pattern which exhibits a strong ZWN 4 structure in the lower middle latitudes and a ZWN 2 pattern at high latitudes in conjunction with a long wave meridional component.

The seventh EOF (8a-b) is dominated by meridional index 3 which corresponds to a wave number 1 mode between the North Pole and equator. ZWN's 4 and 5 together contribute to produce a very wave-like pattern particularly over the western hemisphere middle latitudes.

The eighth EOF (8c-d) is dominated by meridional index 5 which roughly corresponds to 1.5 wavelengths between the North Pole and equator. The large contributions from ZWN's 1 and 2 are reflected in the elongated anomalies throughout the middle latitudes. The most intense anomaly center is located over the eastern North Pacific Ocean with an anomaly of opposite sign to the south.

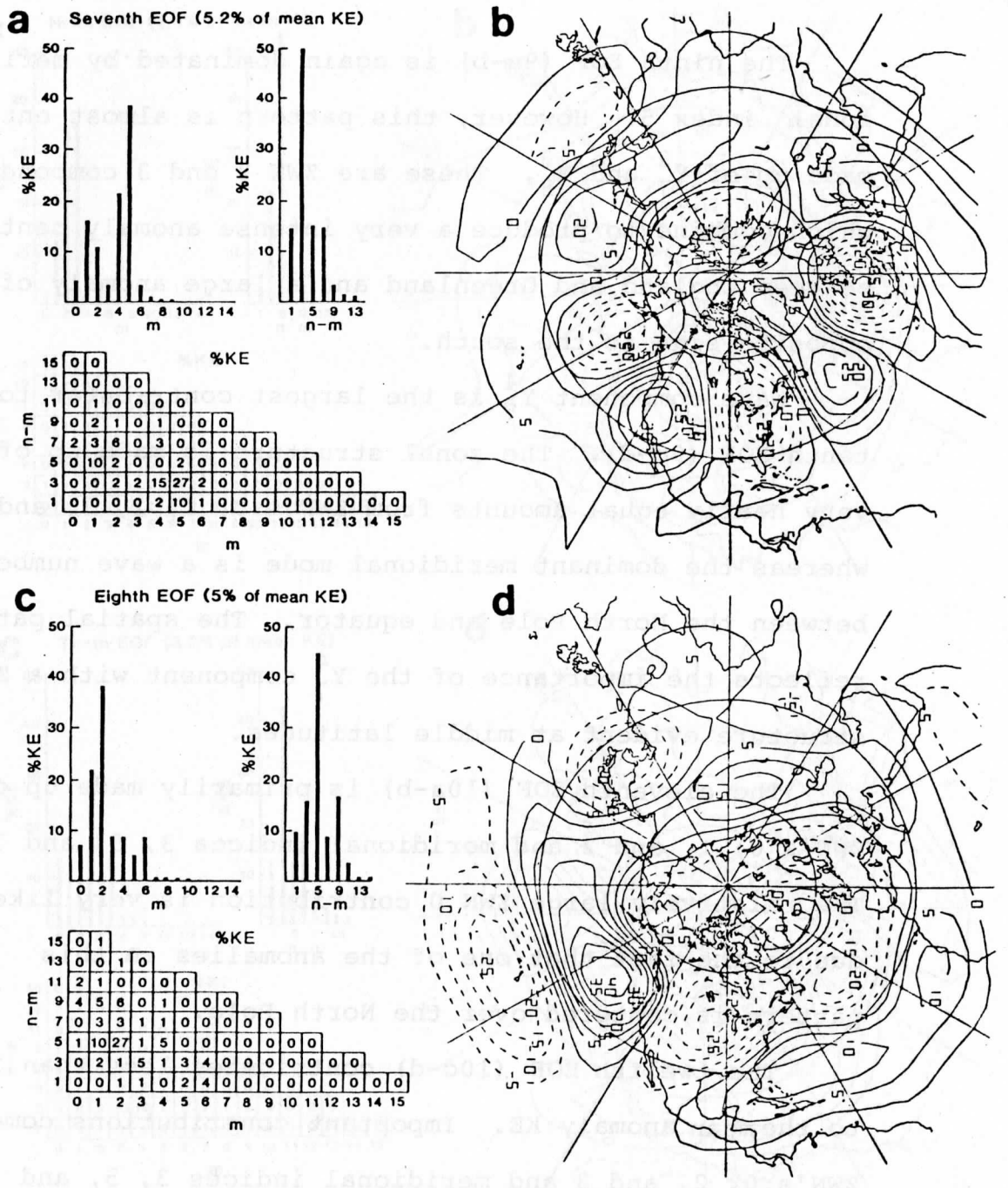

Figure 8. As in Fig. 5, except for the seventh and eighth EOF's which account for 5.2 and 5.0% of the total mean anomaly KE, respectively.

The ninth EOF (9a-b) is again dominated by meridional index 5. However, this pattern is almost entirely made up of Y_7^2 and Y_8^3. These are ZWN 2 and 3 components which combine to produce a very intense anomaly centered between England and Greenland and a large anomaly of opposite sign to the south.

Wave component Y_7^4 is the largest contributor to the tenth EOF (9c-d). The zonal structure is made up of very nearly equal amounts from ZWN's 0, 1, 2, 3, and 5, whereas the dominant meridional mode is a wave number 1 between the North Pole and equator. The spatial pattern reflects the importance of the Y_7^4 component with a ZWN 4 structure evident at middle latitudes.

The eleventh EOF (10a-b) is primarily made up of ZWN's 0, 1, and 2 and meridional indices 3, 5, and 7. The relatively large ZWN 0 contribution is very likely due to the fact that one of the anomalies in this pattern is centered over the North Pole.

The twelfth EOF (10c-d) contributes less than 3% to the mean anomaly KE. Important contributions come from ZWN's 0, 2, and 3 and meridional indices 3, 5, and 7. The dominant spectral component is Y_6^3. The strong ZWN 3 dependence is clearly evident in the middle latitude anomaly pattern.

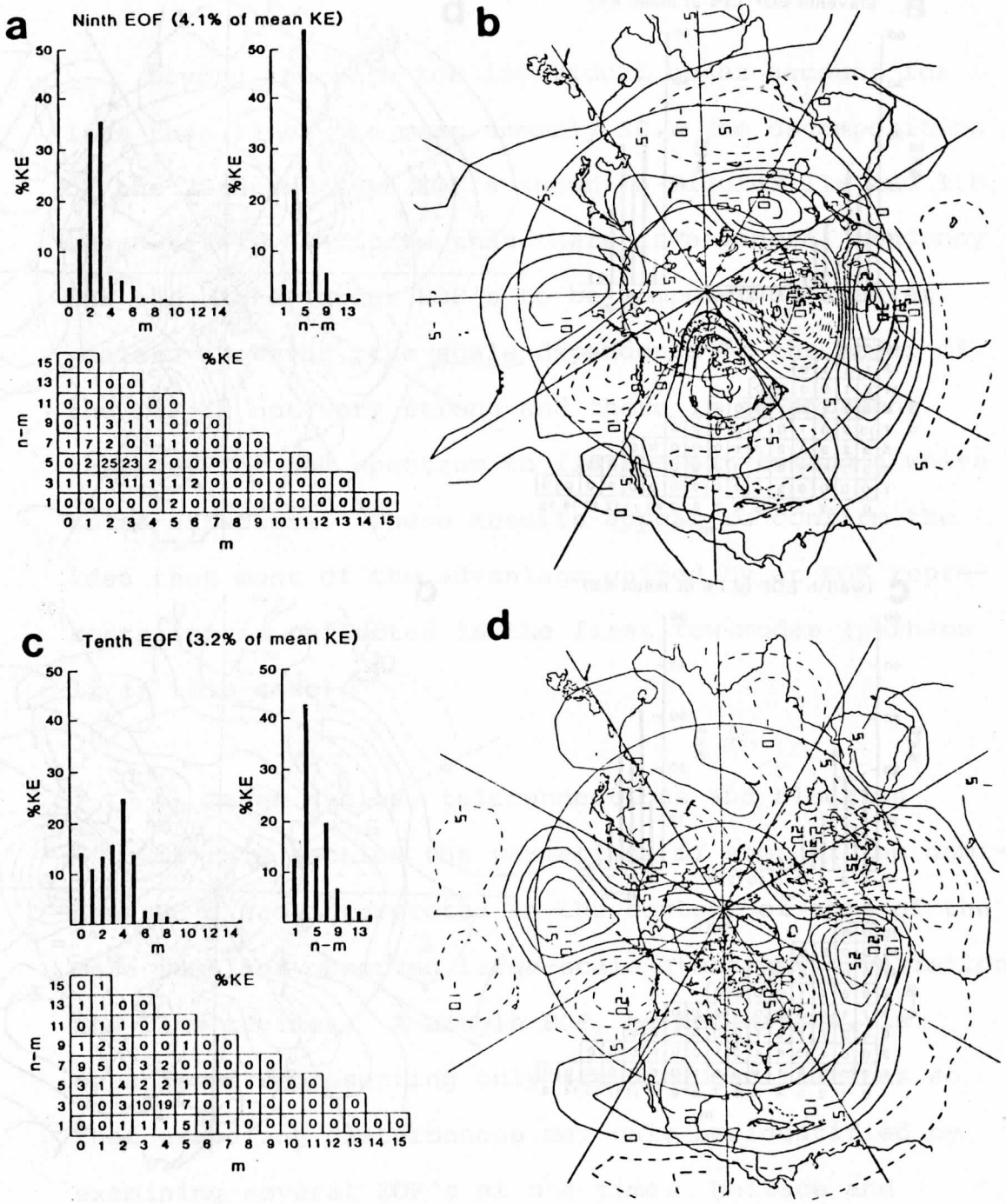

Figure 9. As in Fig. 5, except for the ninth and tenth EOF's which account for 4.1 and 3.2% of the total mean anomaly KE, respectively.

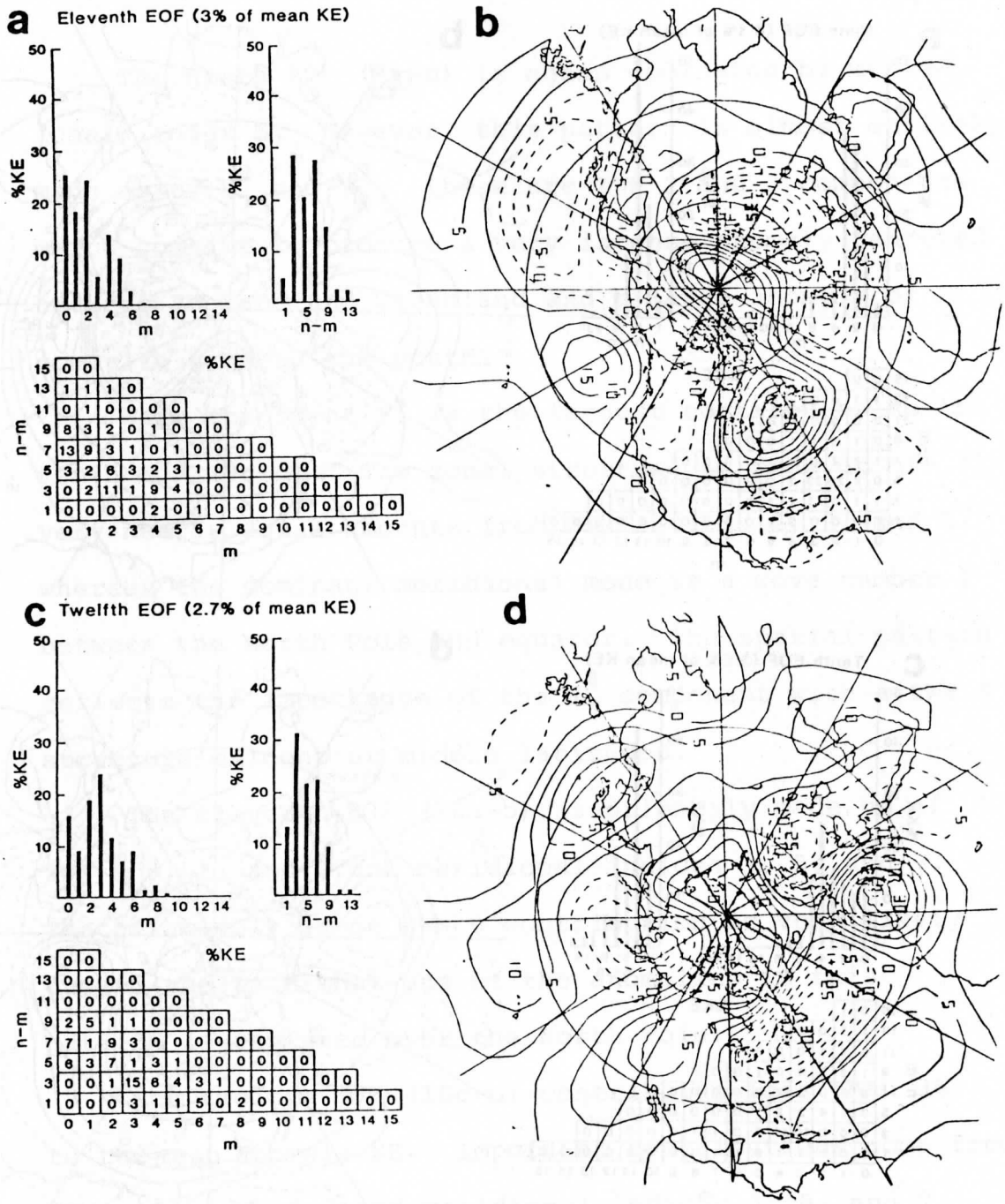

Figure 10. As in Fig. 5, except for the eleventh and twelfth EOF's which account for 3.0 and 2.7% of the total mean anomaly KE, respectively.

Beyond the 25th EOF individual modes account for less than 1% of the mean anomaly KE. The decomposition of the 25th and 40th EOF's shown in Figures 11a and 11b, respectively, indicate that there is a general tendency for the higher order EOF's to be composed of smaller scales. However, the scale dependence on the order of the EOF is not very strong and there is an apparent tendency for the spectrum to flatten out toward a white noise structure. These results appear to confirm the idea that most of the advantage gained by an EOF representation is reflected in the first few modes (perhaps 12 in this case).

b) Index cycles, teleconnections and blocking

In this section the variations of some of the dominant PC's are interpreted in the context of some of the more familiar observed large-scale atmospheric variations and flow regimes. A single EOF, by definition, is capable of representing only standing oscillations so that traveling disturbances may only be identified by examining several EOF's at one time. Wallace and Dickinson (1972) have developed an alternative EOF representation in which the eigenvectors of the cross-spectrum matrix are applied to a time series consisting

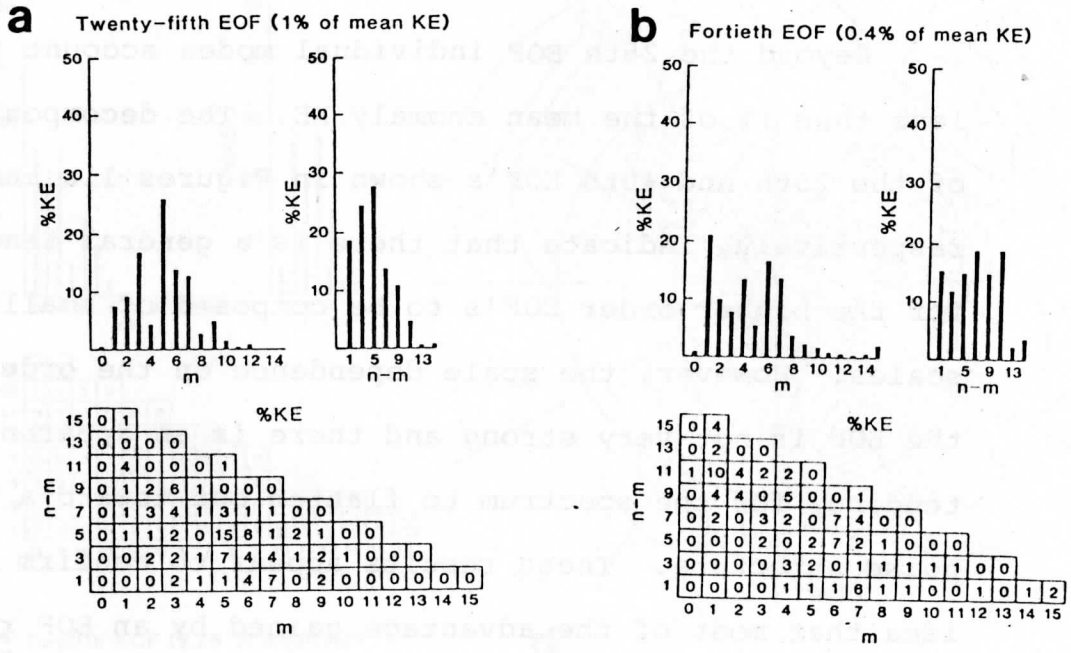

Figure 11. As in Fig. 5a, except for the twentyfifth and fortieth EOF's which account for 1.0 and 0.4% of the total mean anomaly KE, respectively.

of the original time series and its time derivative. Such an approach is more suitable for investigating wave disturbances; however, since the present analysis is primarily concerned with isolating the dominant modes of variability and using them as the dependent variables in a dynamical model, the somewhat simpler EOF approach based on the covariance matrix has been used.

In order to understand better the nature of the PC fluctuations, large positive and negative values of the PC's (equal to $\pm 10^{-3}$ and corresponding to approximately 2.5 standard deviations for the first PC and up to 5 for the ninth PC) are used to superimpose the anomaly patterns on the winter mean flow; these will be referred to as the positive and negative instances of the EOF's. The 500 mb mean flow (Figure 12a) with its characteristic wintertime east coast jets is shown to provide a reference for the following discussion. Figure 12b shows this flow is dominated by ZWN 0 and has small contributions from ZWN's 1, 2, and 3.

Figure 13 shows the positive and negative instances of the first EOF. The basic behavior of this mode is an expansion (positive value of the associated PC -- Figure 13a) or contraction (negative value--Figure 13b) of the circumpolar vortex. The expanded vortex is characterized

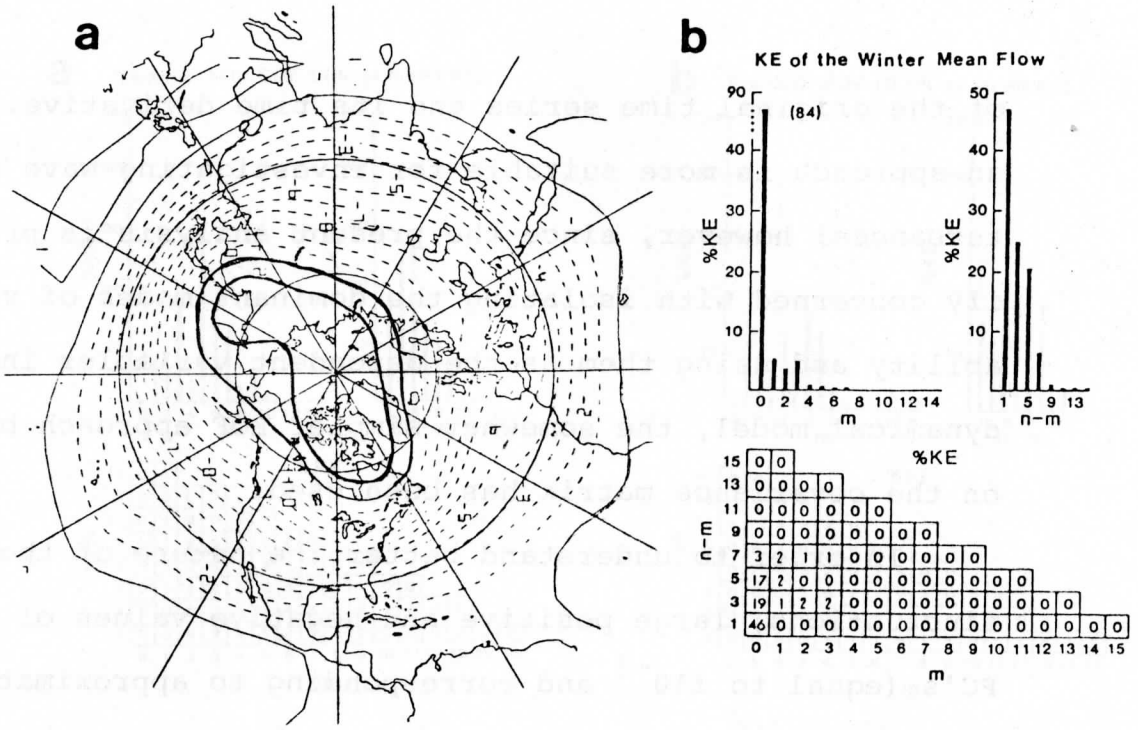

Figure 12. (a) The spatial pattern and (b) the spectral distribution of the climatological mean winter 500 mb stream function. The zonal (m), meridional (n - m) and individual wave dependences are presented as a fraction of the mean flow KE. The mean flow accounts for approximately 76% of the total mean KE. Heavy contours are shown for emphasis. Units: non-dimensional, contour interval is 10^{-3}.

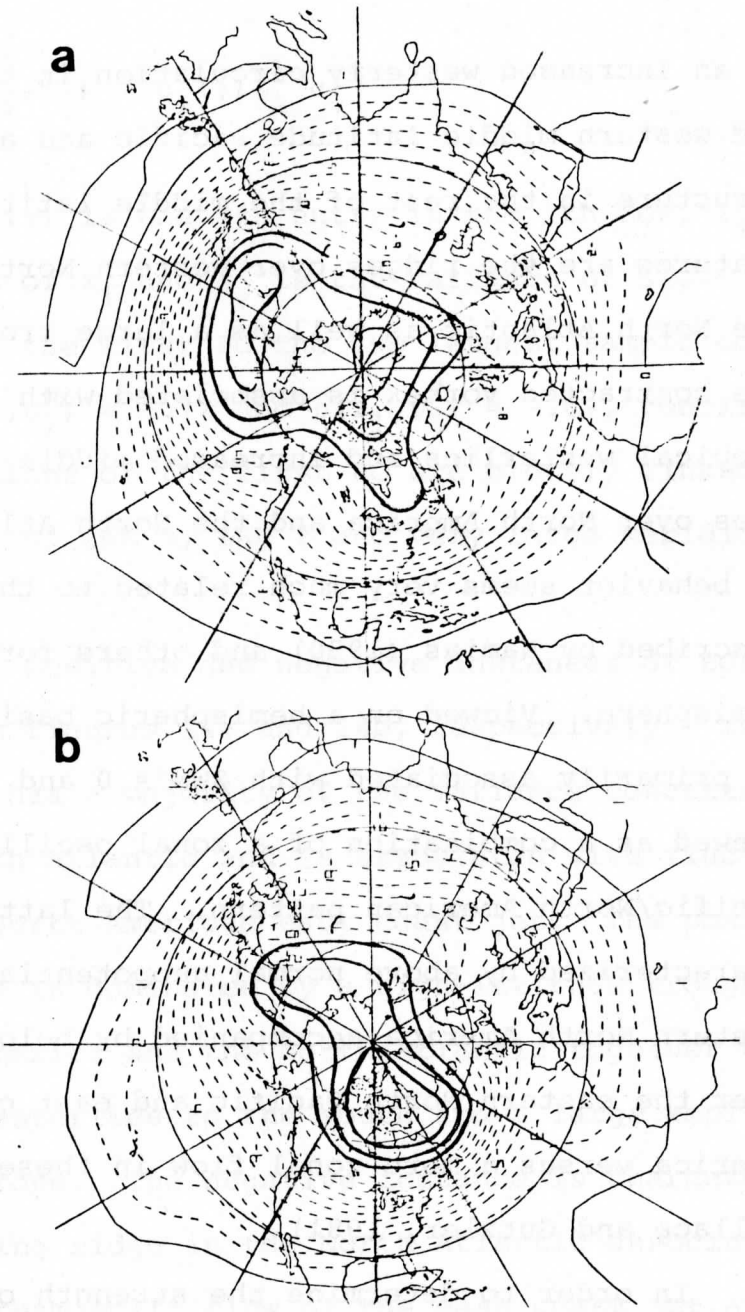

Figure 13. The first EOF superimposed on the winter mean flow with a large (a) positive and (b) negative PC corresponding to 2.5 standard deviations of the 10-day averaged data. Heavy contours are shown for emphasis. Units: non-dimensional, contour interval is 10^{-3}.

by an increased westerly circulation in the subtropics and western middle latitude Pacific and a more wave-like structure in the rest of the middle latitudes. Prominent features are the ridges over western North America and the North Atlantic as well as a large trough over Europe. The contracted vortex is associated with weaker subtropical westerlies and increased middle latitude westerlies over North America and the North Atlantic. This mode of behavior seems very much related to the index cycle described by Namias (1950) and others for the western hemisphere. Viewed on a hemispheric basis this behavior is primarily associated with ZWN's 0 and 2 and may be viewed as a combination of a zonal oscillation and the Pacific/North American pattern. The latter pattern is characterized by above normal geopotential heights over western North America accompanied by below normal heights over the eastern North Pacific and east coast of North America versus a more zonal flow in these regions (see Wallace and Gutzler, 1981).

In order to determine the strength of association between the PC's and the various spectral components, a correlation (in time) between the ith PC, z_i, and spectral coefficient, ψ_γ, (the spectral version of (2.2.7)) is computed as

$$\rho(z_i,\psi_\gamma) = e_i(\gamma)\lambda_i^{\frac{1}{2}}\sigma_\gamma^{-\frac{1}{2}} \qquad (2.3.2)$$

where $e_i(\gamma)$ is the γth entry in the ith EOF, λ_i is the variance of z_i and σ_γ is the variance of ψ_γ.

For the first PC the two largest sample correlations are $\hat{\rho}(z_1,\psi_1^o) = -.72$ and $\hat{\rho}(z_1,\psi_5^2) = -.69$, confirming that oscillations of the first PC are closely linked to the behavior of ZWN 0, ZWN 2 and very large meridional scales.

The positive and negative instances of EOF 2 are shown in Figures 14a and 14b, respectively. This anomaly pattern has a majority of the variance concentrated in the North Atlantic and is associated with fluctuations in the North American east coast jet. The positive instance is dominated by a high-latitude trough over North America and the North Atlantic together with strong zonal westerlies to the south and a large amplitude ridge over Europe. The negative instance is characterized by a blocking ridge in the North Atlantic associated with an upstream split flow of the east coast jet and ridging over the Asian continent. Strongest correlations of the second PC are with ψ_6^3 (-.55), ψ_7^2 (-.54) and ψ_8^1 (-.54). This mode of behavior seems to bear some resemblance to the North Atlantic Oscillation reviewed by Wallace and

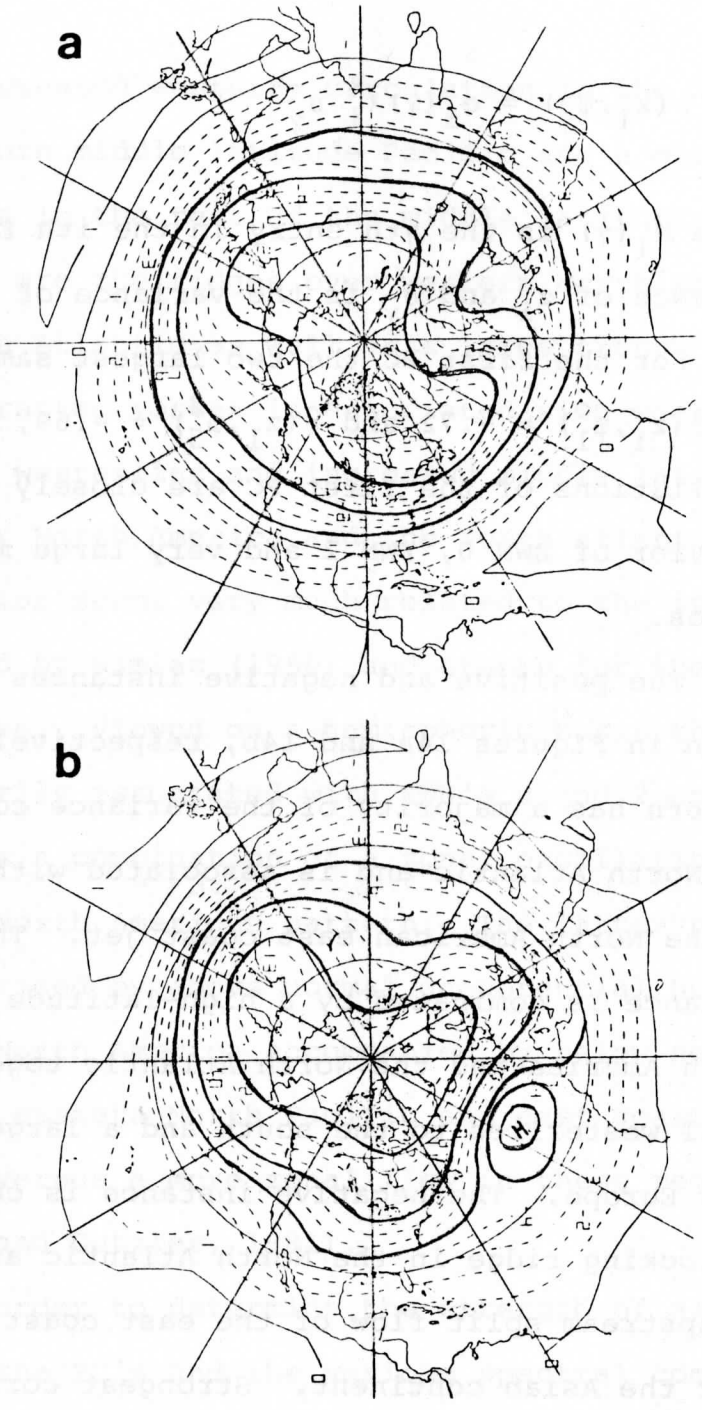

Figure 14. As in Fig. 13, except for the second EOF and corresponding to 3.2 standard deviations.

Gutzler, 1981 and shown schematically in their Figure 1. This should be compared to Figure 5d in the present study.

Figures 15a and 15b show positive and negative instances of the third EOF, respectively. The positive instance is characterized by high latitude ridges in the eastern North Pacific and North Atlantic oceans and a very flat zonal flow pattern over the United States. The negative instance shows a large trough over the North Pacific, a ridge over western North America and a trough over eastern North America. The strongest correlation with the third PC is with ψ_6^3 (.65) indicating that the third PC is closely associated with fluctuations in ZWN 3. This mode also exhibits similarities to the Pacific/ North American pattern.

In order to determine which of the EOF's are important contributors to wintertime blocking patterns, a study by Hartmann and Ghan (1980) was used to determine occurrences of Pacific and Atlantic blocking during the winters (Nov. 15 - March 14 by their definition) of 1965 through 1975. In their study blocking was assumed to occur in either the Atlantic or Pacific if the 500 mb geopotential height exceeded the mean in the longitude sector by more than a specified amount and had a duration

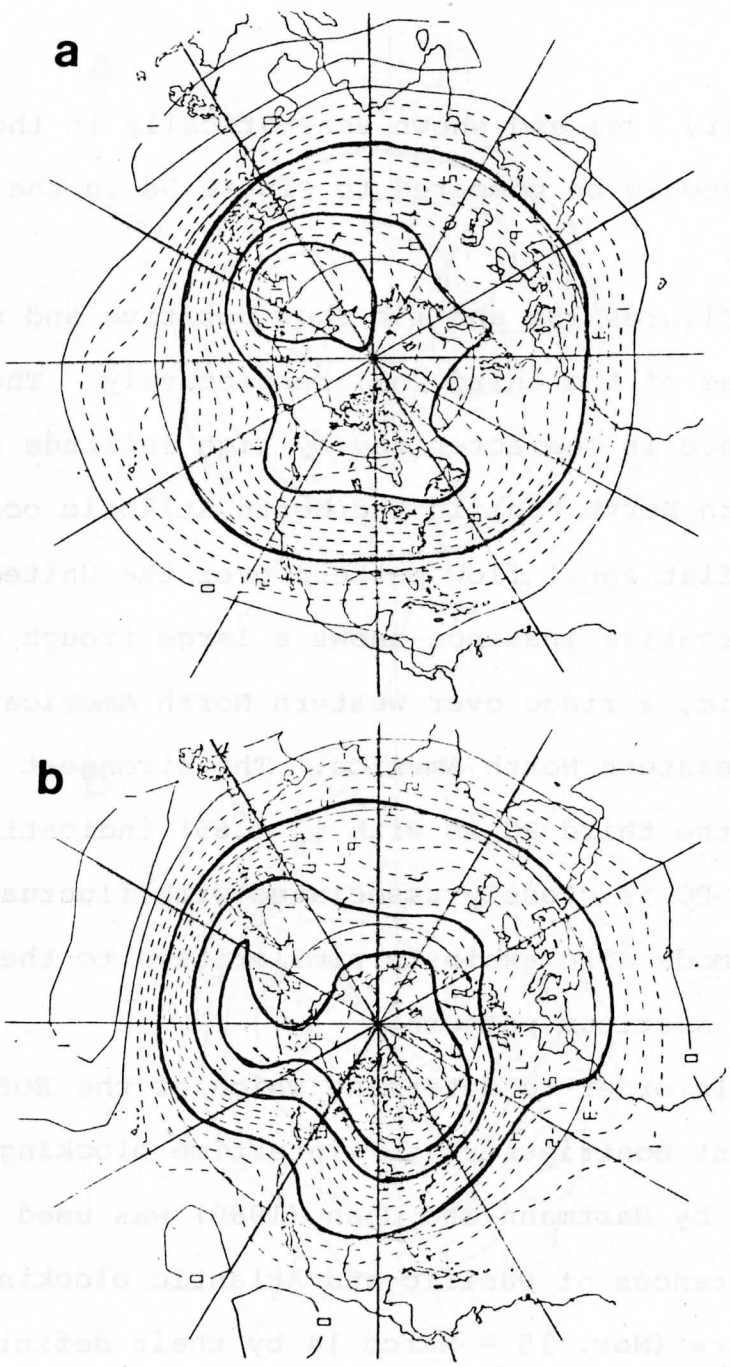

Figure 15. As in Fig. 13, except for the third EOF and corresponding to 3.4 standard deviations.

of six or more days.

Figures 16a and 16b show the mean value of the first 25 PC's during times of Atlantic blocking and Pacific blocking, respectively. In general, one finds that the most important contributions to the blocking patterns lie within the statistically significant EOF's 1-12. In the case of Atlantic blocking a detailed inspection of the PC time variations reveals that blocking occurrences are most closely linked to negative values of the ninth PC. For the case of Pacific blocking such an inspection shows that positive values of the fourth PC (and to a lesser degree negative values of the 12th PC) are most closely linked to blocking. While these higher order PC's contribute a relatively small amount to the total variance defined in (2.2.6a), they may contribute much more to the local variance (2.2.6b). For example, the ninth PC accounts for only 3.6% of the total variance yet over the North Atlantic its contribution to the local variance is equal to or greater than that of the first PC.

The negative and positive instances of the ninth EOF are shown in Figures 17a and 17b, respectively. The resemblance of the negative instance to a classical high latitude Atlantic block is striking. The pattern consists of a very strong ridge in the North Atlantic

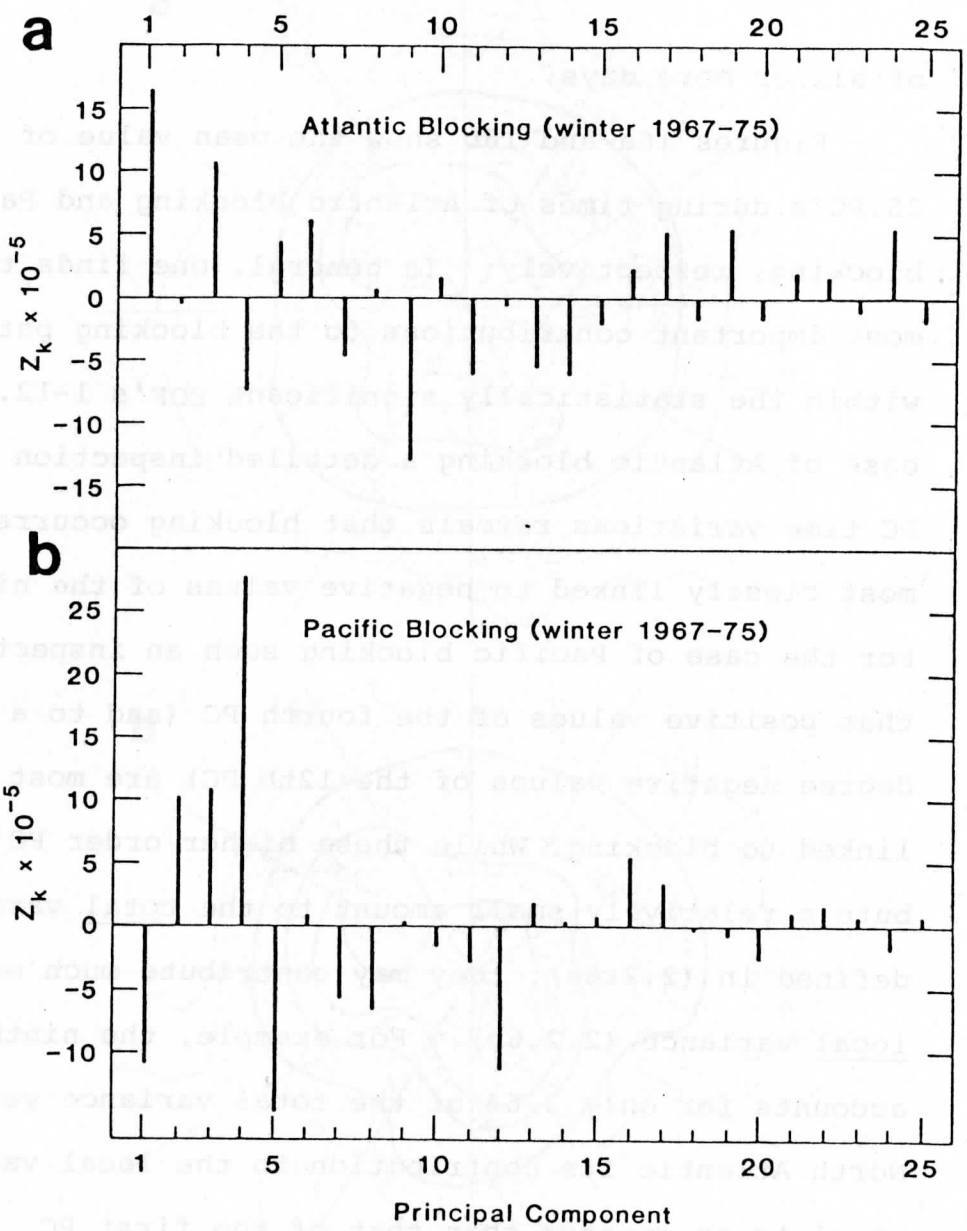

Figure 16. The time averaged value of the first 25 PC's during periods of (a) Atlantic blocking and (b) Pacific blocking. Units: non-dimensional.

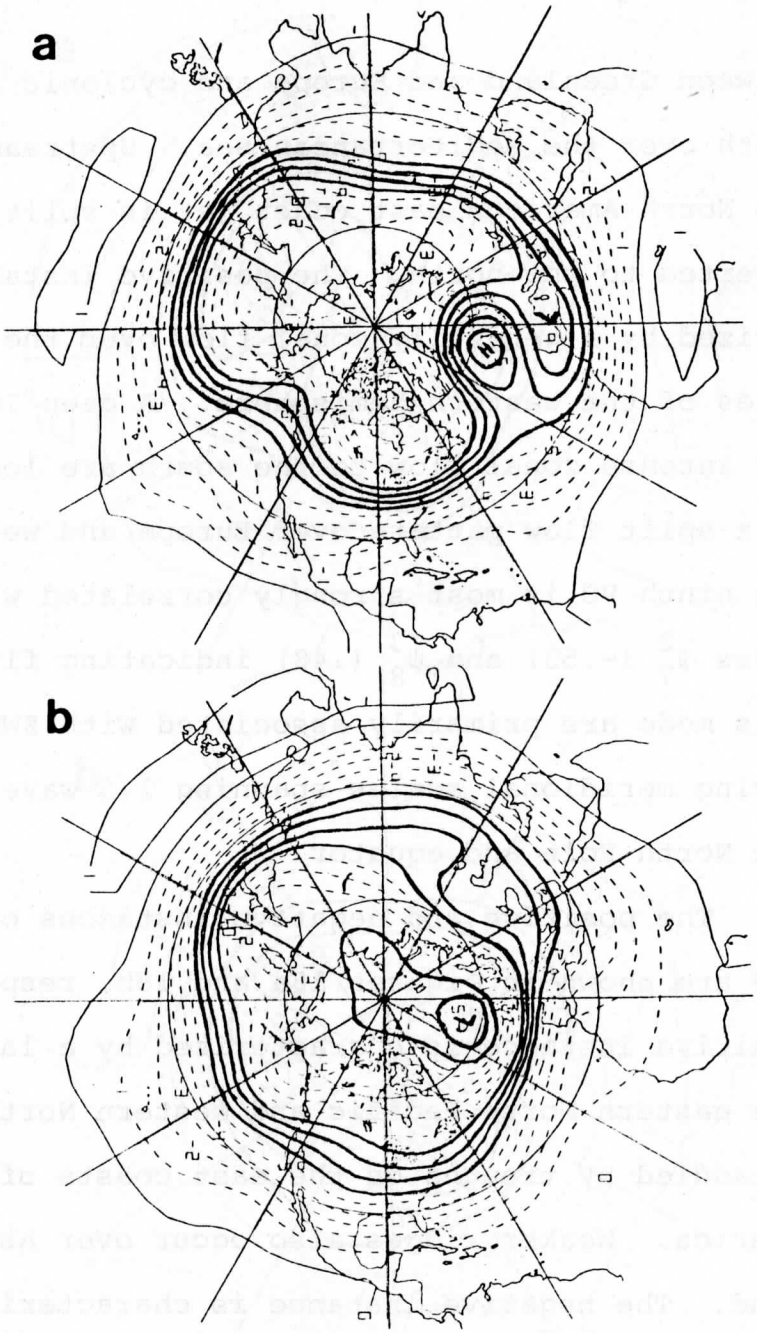

Figure 17. As in Fig. 13, except for the ninth EOF and a large (a) negative and (b) positive PC corresponding to 5.3 standard deviations of the 10-day averaged data.

between Greenland and Europe and cyclonic flow to the south over the Mediterranean Sea. Upstream of the ridge the North American east coast jet is split and strongly diverted to the north. The positive instance is characterized by a generally zonal flow over the middle latitudes of the western hemisphere. A deep Icelandic low and intense zonal flow to the south are located upstream of a split flow pattern over Europe and western Asia. The ninth PC is most strongly correlated with spectral modes ψ_7^2 (-.53) and ψ_8^3 (.48) indicating fluctuations in this mode are primarily associated with ZWN's 2 and 3 having meridional scales spanning 1.5 wavelengths between the North Pole and equator.

The positive and negative instances of the fourth EOF are shown in Figures 18a and 18b, respectively. The positive instance is characterized by a large ridge over the eastern North Pacific and western North America straddled by troughs on the east coasts of Asia and North America. Weaker ridges also occur over Asia and Greenland. The negative instance is characterized by a more zonal flow over the Pacific, North America and Asia, while the eastern Atlantic and Europe are dominated by a middle latitude ridge. The fourth PC is most strongly correlated with ψ_3^0 (.58) and ψ_8^3 (.58) indicating

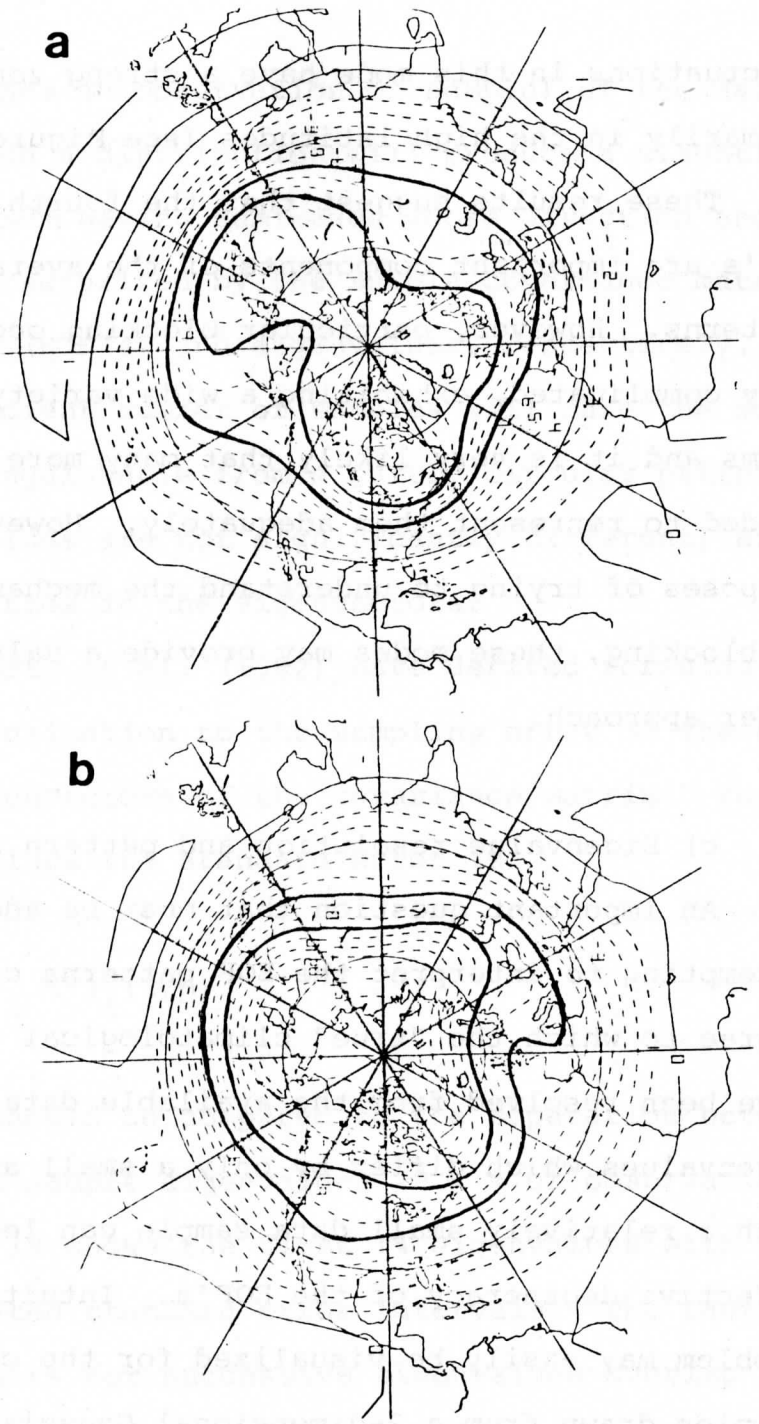

Figure 18. As in Fig. 13, except for the fourth EOF and corresponding to 3.6 standard deviations.

fluctuations in this mode have a strong zonal character primarily in the high latitudes (see Figure 6d).

These results suggest that the fourth and ninth EOF's are important components of the average blocking patterns. However, particular blocking occurrences are very complicated, exhibiting a wide variety of different forms and it is very likely that many more EOF's are needed to represent them adequately. However, for the purposes of trying to understand the mechanisms involved in blocking, these modes may provide a valuable first order approach.

c) Eigenvalue resolution and pattern stability

An important question that must be addressed when attempting to interpret the EOF patterns concerns the degree to which the "true" climatological variations have been resolved from the available data. Population eigenvalues which differ by only a small amount combined with a relatively small data sample can lead to an effective degeneracy of the EOF's. Intuitively this problem may easily be visualized for the case of samples drawn from a 2-dimensional Gaussian distribution with zero mean and nearly identical variances for the components. A scatterplot (a plot where each point

represents an observation or sample) of the samples taken from such a distribution will produce a slightly elliptical pattern having semi-axes whose direction and length are characterized by the sample covariance matrix eigenvectors (EOF's) and eigenvalues, respectively. However, an insufficient number of samples will make the scatterplot indistinguishable from a purely circular pattern (sample eigenvalues are not significantly different) and lead to ambiguities in the eigenvectors.

North et al. (1982) have derived formulas which give an approximation to the sampling error of the eigenvalues and eigenvectors of the covariance matrix. For the eigenvalues the standard error is

$$\delta\lambda_i \sim \lambda_i (2/p)^{\frac{1}{2}} \qquad (2.3.3)$$

which should be compared to the separation between successive sample eigenvalues (P = # of observations). Figure 19 shows the first 14 eigenvalues with the associated standard error intervals. The fact that the error bars for successive eigenvalues overlap suggests that (except for the first EOF) the length of the data set allows only a marginal resolution of the true (population) EOF's and therefore one would expect a

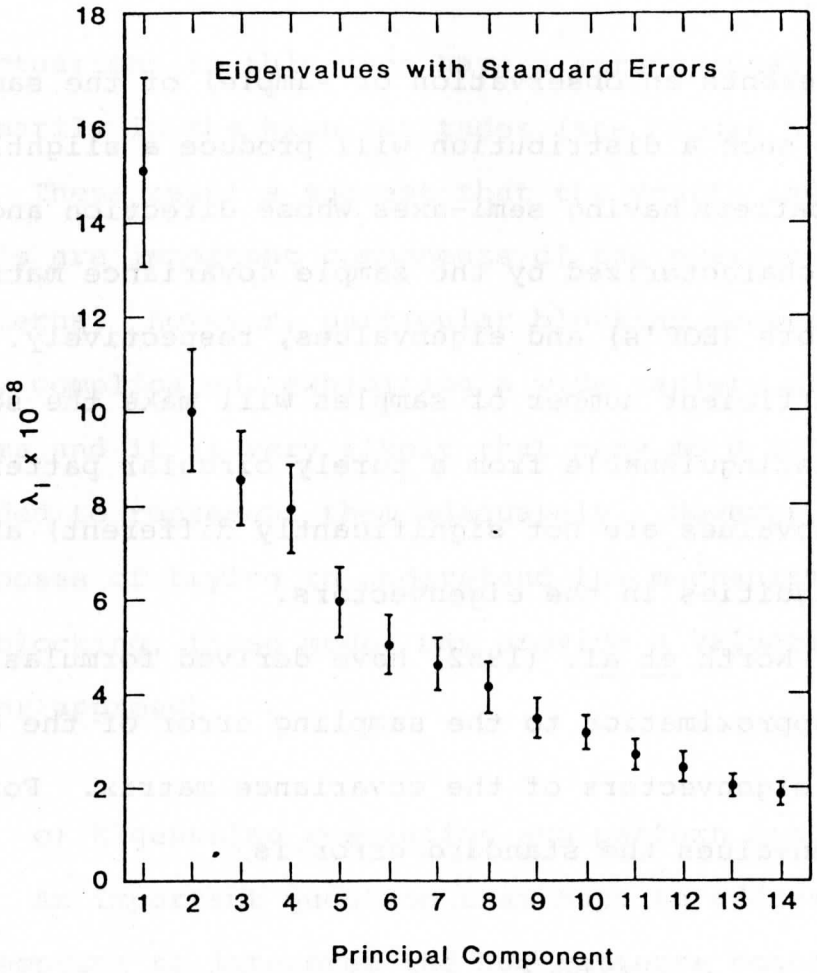

Figure 19. Eigenvalues of the covariance matrix computed from 10-day averaged winter stream function anomalies and the associated approximate standard error bars. Units: non-dimensional.

considerable amount of variability in the details of EOF's computed from different data sets.

To check further the degree of intersample variability in the EOF patterns a comparison is made with the EOF's published by several different authors (Weickmann, 1982; Rhinne, et al., 1981; Fechner, 1981; Jeckström, 1977). Here differences in the EOF's arise not only from differences in the time periods of the data but also from differences in data processing (analysis method and space and time filtering) as well as the choice of variable(s) used in the expansion (e.g. streamfunction, geopotential, winds, horizontal and vertical extent).

Part of the Weickmann study involved an EOF analysis of a circulation data set extending from 85°N to 30°S. NMC gridded objective analyses of the 250 mb and 850 mb Northern Hemisphere winter winds were used covering the period 1974-75 through 1979-80. Five day mean values were computed and the annual cycle was not removed. Only the first three EOF's were presented. The first was found to be associated with the variations of the annual cycle whereas, the second and third describe wavenumber one and two index cycles. Even though direct comparisons with the wind EOF's are difficult, the general behavior of the second and third EOF's when

superimposed on the mean flow is qualitatively similar to the behavior of the first and second EOF's in the present study.

A more direct comparison can be made with the Rhinne et al. results in which the EOF's are based on Fleet Numerical Weather Center analyses of the 500 mb geopotential for the years 1946-70. The data include all seasons and cover the area north of 20°N with a grid length of 381 km at 60°N. 11,876 time periods were used and the annual cycle was not removed. The first EOF is again associated with the annual cycle. The second EOF pattern is similar to the first EOF of the present study which describes an index cycle behavior and the fourth EOF is similar to the third of the present study. Beyond this, there is no clear correspondence between the EOF's except for the eighth which is similar to the ninth blocking mode of the present study.

The work by Fechner is based on the same DWD data set as the present study. The main differences are that the expansion is based on the 500 mb height field; the study is not limited to the winter season and no time averaging is done. Of the eight EOF's presented, the first, second and seventh EOF's are similar to the first, fourth and ninth EOF's of the present study,

respectively.

The Jeckström study also uses the same basic geopotential data on the DWD grid for the years 1966-74 truncated, however, at total wavenumber 12. The analysis covers only the winter months and the annual cycle is not removed. EOF's two through eight are presented superimposed on the first EOF which describes the annual cycle. The second EOF describes an index cycle which is similar to the behavior of the first EOF of the present study. In addition, the third and fourth EOF's are similar to the third (Pacific/North American pattern) and fourth (North Pacific blocking) EOF's of the present study.

In general, the comparisons tend to confirm the sampling errors shown in Figure 19. An index cycle mode is found in all the studies and is usually associated with the first EOF or the second EOF when the annual cycle is not removed. In the latter case the first EOF describes the annual variation. Similarities are found in some cases with higher order EOF's; most surprising is the reproducibility of the ninth (North Atlantic blocking) EOF. However, the lack of a one-to-one correspondence between the EOF's of the different studies indicates that longer data records and more detailed

studies of the effects of data errors and analysis methods are needed in order to determine the true climatological modes of atmospheric variability.

3. MODEL FORMULATION

In this chapter an equivalent barotropic model is formulated as a set of prognostic equations for the anomaly streamfunction PC's at the 500 mb level. The basic equations consist of the linear balanced system. Kruse (1983) gives a detailed scale analysis showing that the vorticity and divergence equations of this system are appropriate for the study of large-scale flows. The thermodynamic equation does not enter into the model due to the assumption of equivalent barotropy. The unknown constants involved in the boundary layer parameterizations are determined by the method of least squares. The seasonal cycle enters into the anomaly equations via the advective terms and as an inhomogeneous forcing term due to the fact that the mean terms, by themselves, do not satisfy the vorticity equation.

3.1. The equivalent barotropic model

a) Basic equations

The fundamental equations in this study (nondimensionalized by twice the Earth's angular speed (2Ω), the Earth's mean radius (a) and reference pressure (p^*))

are, the vorticity equation**

$$\frac{\partial}{\partial t}\nabla^2\psi + \underset{\sim}{v}_\psi\cdot\nabla(\nabla^2\psi + f) + \underbrace{\underset{\sim}{v}_\chi\cdot\nabla f + f\nabla^2\chi}_{D\nabla^2\chi} = 0 \qquad (3.1.1)$$

the continuity equation

$$\nabla^2\chi + \partial\omega/\partial p = 0 \qquad (3.1.2)$$

and the linear balance equation

$$D\nabla^2\psi - \nabla^2\Phi = 0 \qquad (3.1.3)$$

where

$$D \equiv \cos\phi\,\frac{\partial}{\partial\phi}\nabla^{-2} + \sin\phi \qquad (3.1.4)$$

The velocity $\underset{\sim}{v}$ has been partitioned into a divergent component $\underset{\sim}{v}_\chi = \nabla\chi$ and nondivergent component $\underset{\sim}{v}_\psi = \underset{\sim}{k} \times \nabla\psi$. ψ and χ are the streamfunction and velocity potential, respectively. The vorticity equation allows for a

---

**See Haltiner and Williams (1980) for a discussion of the linear balanced system.

variable coriolis parameter (f) and includes advection of planetary vorticity by the divergent wind and the stretching term. Φ is the geopotential, p is pressure and ω is the pressure vertical velocity. ∇^{-2} is the inverse Laplacian and is evaluated in the spectral domain.

The vertical structure of the model atmosphere is divided into two domains consisting of the free atmosphere and the planetary boundary layer (PBL). In the free atmosphere it is assumed that

$$\psi(\lambda,\phi,p,t) = A(p)[\psi] \qquad (3.1.5)$$

where the brackets denote a vertical average above the PBL and A(p) is a vertical structure function such that $[A] = 1$. At the equivalent barotropic level defined by $\psi(\lambda,\phi,p^*,t) = [\psi][A^2]$, (3.1.1) is written as

$$\frac{\partial}{\partial t}\nabla^2\psi = -\underset{\sim}{v}_{\psi}\cdot\nabla(\nabla^2\psi + f) + [A^2]/p_i D\omega(p_i) \qquad (3.1.6)$$

where p_i is the non-dimensional pressure at the bottom of the free atmosphere.

In the PBL it is assumed that there is a balance between friction ($\underset{\sim}{F}_H$), coriolis and pressure gradient forces such that

$$-D\frac{\partial\omega}{\partial p} = -\underset{\sim}{v}_{\psi}\cdot\nabla f + \underset{\sim}{k}\cdot\nabla\times\underset{\sim}{F}_{H} \tag{3.1.7}$$

Integrating (3.1.7) from the top of the PBL to the bottom one obtains

$$D\omega(p_i) = D\omega(p_s) - \{\frac{(p_s-p_i)}{[A^2]}K_2A(p_i)\}\underset{\sim}{v}_{\psi}\cdot\nabla f - \{\frac{g\rho_o c_D K_1 A(p_i)}{(2\Omega)^3 a^2 [A^2]}\}\nabla^2\psi \tag{3.1.8}$$

where it has been assumed that the PBL is bounded at the top by p_i and at the bottom by p_s. Furthermore, it is assumed that

$$\underset{\sim}{F}_{H} = -\frac{g}{(2\Omega)^2 a}\frac{\partial\underset{\sim}{\tau}}{\partial p} \tag{3.1.9a}$$

$$\underset{\sim}{\tau}(p_s) = \frac{\rho_o c_D}{2\Omega a}\underset{\sim}{v}_{\psi}(p_s) \tag{3.1.9b}$$

$$[\psi]^{PBL} \equiv K_2\psi(p_i) \tag{3.1.9c}$$

and

$$\psi(p_s) \equiv K_1\psi(p_i) \tag{3.1.9d}$$

where $\underset{\sim}{\tau}$ is the stress with $\underset{\sim}{\tau}(p_i) \equiv 0$. The surface drag

parameterization has coefficient (c_D) with units of velocity and is formulated to be consistent with the Ekman layer formulation (e.g. Holton, 1972). The mean non-dimensional density in the PBL is ρ_o; p_s and p_i are the non-dimensional pressures at the bottom and top of the PBL, respectively, and K_1 and K_2 are assumed to be constant.

At the lower boundary the expanded form of the vertical velocity ($w = \frac{dz}{dt}$)

$$\omega(p_s) \doteq \rho_o\left(\frac{\partial \Phi(p_s)}{\partial t} - \frac{g}{(2\Omega)^2 a} w(p_s)\right) \qquad (3.1.10)$$

is used to allow for the effects of surface pressure tendencies and orography, where the advective term has been neglected and

$$w(p_s) \doteq \underset{\sim}{v}_{\psi}(p_s)\cdot\nabla h \qquad (3.1.11)$$

where h is the non-dimensional height of the Earth's surface. Then substituting (3.1.3) for Φ and (3.1.11) for w into (3.1.10), one obtains at the lower boundary

$$\omega(p_s) = \frac{K_1 A(p_i)\rho_o}{[A^2]}\nabla^{-2}D\nabla^2\frac{\partial \psi}{\partial t} - \frac{\rho_o A(p_i) K_1 g}{[A^2](2\Omega)^2 a}\underset{\sim}{v}_{\psi}\cdot\nabla h \qquad (3.1.12)$$

Finally (3.1.6), (3.1.8) and (3.1.12) are combined such that

$$\frac{\partial}{\partial t}(1 - L_1)\nabla^2\psi = J(\nabla^2\psi,\psi) - (1 + \varepsilon)\frac{\partial\psi}{\partial\lambda} + L_2 J(h,\psi) - \kappa\nabla^2\psi \qquad (3.1.13)$$

where

$$L_1 = \frac{(2\Omega a)^2}{gH^*} D\nabla^{-2}D \qquad (3.1.14a)$$

$$\varepsilon = \frac{p_s - p_i}{p_i} K_2 A(p_i) \qquad (3.1.14b)$$

$$L_2 = \frac{a}{H^*} D \qquad (3.1.14c)$$

$$\kappa = \frac{c_D}{H^*}\frac{1}{2\Omega} \qquad (3.1.14d)$$

and

$$H^* = \frac{p_i'}{\rho_o' g K_1 A(p_i)} \qquad (3.1.14e)$$

where H^* is a scale height parameter, the primes denote dimensional quantities, and J is the Jacobian representation of the advective terms where

$$J(A,B) = \partial(A,B)/\partial(\lambda,\sin\phi) \qquad (3.1.14f)$$

(3.1.14a) is a generalized form of the long wave correction term. The usual form of this term (see e.g. Haltiner and Williams, 1980) may be obtained by replacing D (3.1.4) by a constant coriolis parameter ($\sin\phi_o$). (3.1.14b) is a correction factor for the beta term. This term arises due to the fact that the coriolis parameter is allowed to vary in the PBL (first term on the RHS of (3.1.7)). (3.1.14c) acts on the orographic vorticity source term and (3.1.14d) is the frictional decay rate.

b) Mean anomaly formulation

One of the problems associated with using barotropic dynamics to model the atmosphere concerns the manner in which to introduce properly (and interpret) a driving or source term. Many theoretical studies dealing with barotropic models have (in a somewhat ad hoc fashion) introduced forcing of a Newtonian type (e.g. Källén, 1981; Charney and DeVore, 1979). More recently, Kruse (1983) has shown that with a more sophisticated treatment of the PBL it is possible to introduce an empirical driving term which (at least for the winter season) may be interpreted as a heat flux from the Earth's surface.

In the present study the thermal driving enters into the model implicitly due to the assumption of a fixed base state equal to the observed winter mean. While the mean state is a statistical quantity which the atmosphere may never resemble for very long time periods, it nevertheless is interpreted as reflecting the mean stabilizing influence of the orography and thermal asymmetries of the lower boundaries. The model is formulated as a prognostic equation for the anomalies (deviations from the base state) which are indirectly forced due to the presence of the base state. This is consistent with the statistical concept of an EOF which represents the modes of fluctuation about a mean state.

In order to obtain a model explicitly involving the PC anomalies the streamfunction is separated into components involving the seasonal cycle (ψ^s) and the deviations from the seasonal cycle (ψ') such that

$$\psi(\lambda,\phi,t) = \psi^s(\lambda,\phi,t) + \psi'(\lambda,\phi,t) \qquad (3.1.15)$$

Substituting (3.1.15) into (3.1.13) leads to

$$\frac{\partial}{\partial t}(1 - L_1)\nabla^2\psi' = J(\nabla^2\psi',\psi') - (1 + \varepsilon)\frac{\partial\psi'}{\partial\lambda}$$

$$+ L_2 J(h,\psi') - \kappa\nabla^2\psi' \qquad (3.1.16)$$

$$+ J(\nabla^2\psi',\psi^s) + J(\nabla^2\psi^s,\psi') + S$$

where

$$S = -\frac{\partial}{\partial t}(1 - L_1)\nabla^2\psi^s + J(\nabla^2\psi^s,\psi^s) - (1 + \varepsilon)\frac{\partial\psi^s}{\partial\lambda}$$

$$+ L_2 J(h,\psi^s) - \kappa\nabla^2\psi^s \qquad (3.1.17a)$$

By ensemble averaging (3.1.16), S is given by

$$S = -\langle J(\nabla^2\psi',\psi')\rangle \qquad (3.1.17b)$$

In (3.1.16) the three additional terms governing the anomalies are the advection of the anomalous vorticity by the mean flow ($J(\nabla^2\psi',\psi^s)$), the advection of mean vorticity by the anomalous wind ($J(\nabla^2\psi^s,\psi')$) and the inhomogeneous forcing term (S) which arises due to the fact that the mean flow vorticity does not satisfy the vorticity equation (3.1.17a). It should be noted that (3.1.17a and b) are not necessarily consistent since

many simplifications have been made in deriving (3.1.17a). As a representation of the average effects of the processes not explicitly included, (3.1.17a) should include a residual term. In practice, S is computed from (3.1.17b) where the ensemble average is replaced by a time average over the entire winter data set and it is assumed that ψ^s does not change appreciably for the time periods of interest.

c) Spectral formulation

The spectral version of (3.1.16) is obtained by expanding all quantities in terms of spherical harmonics (Y_γ) such that

$$\psi(\lambda,\phi,t) = \sum_\gamma \psi_\gamma(t)\ Y_\gamma(\lambda,\phi) \qquad (3.1.18a)$$

$$S(\lambda,\phi) = \sum_\gamma S_\gamma\ Y_\gamma(\lambda,\phi) \qquad (3.1.18b)$$

$$h(\lambda,\phi) = \sum_\delta h_\delta\ Y_\delta(\lambda,\phi) \qquad (3.1.18c)$$

and

$$\omega(\lambda,\phi,\ t) = \sum_\delta \omega_\delta(t)\ Y_\delta(\lambda,\phi) \qquad (3.1.18d)$$

where $\gamma \equiv (n_\gamma, m_\gamma)$, $n_\gamma - m_\gamma$ is odd and $n_\delta - m_\delta$ is even. The Y_γ are normalized so that

$$\int_0^{2\pi} \int_{-\pi/2}^{\pi/2} \bar{Y}_\gamma Y_\beta \cos\phi d\phi d\lambda = 4\pi\delta_{\gamma\beta} \qquad (3.1.19a)$$

The spherical harmonics satisfy the equation

$$\nabla^2 Y_\gamma = - c_\gamma Y_\gamma \qquad (3.1.19b)$$

where $c_\gamma = n_\gamma(n_\gamma + 1)$ and by definition

$$Y_{\bar{\gamma}} = \bar{Y}_\gamma \qquad (3.1.19c)$$

Further properties are given in Platzman (1962). In spectral form (3.1.16) is

$$\begin{aligned} c_\gamma \dot{\psi}_\gamma + N\{r_1(\gamma)\dot{\psi}_\gamma + r_2(\gamma^+)\dot{\psi}_{\gamma^{++}} + r_2(\gamma^-)\dot{\psi}_{\gamma^{--}}\} \\ = i/2 \sum_\alpha \sum_\beta \psi_\alpha \psi_\beta (c_\beta - c_\alpha) L_{\gamma\beta\alpha} + im_\gamma(1+\varepsilon)\psi_\gamma \\ + Mi \sum_\delta \sum_\beta h_\delta \psi_\beta T_{\gamma\beta\delta} - \kappa c_\gamma \psi_\gamma \qquad (3.1.20) \\ + i \sum_\alpha \sum_\beta \psi^s_\alpha \psi_\beta (c_\beta - c_\alpha) L_{\gamma\beta\alpha} + S_\gamma \end{aligned}$$

where $\psi' = \sum_{\gamma} \psi_{\gamma} Y_{\gamma}$ and $\psi^{s} = \sum_{\gamma} \psi_{\gamma}^{s} Y_{\gamma}$. The first term on the left hand side (LHS) is the tendency and the second term in braces is the long wave correction where

$$r_1(\gamma) = (1 - \delta_{1n_\gamma})(B_1(n_\gamma - 1, m_\gamma))^2 + \left(\frac{n_\gamma}{n_\gamma + 2}\right)(B_1(n_\gamma, m_\gamma))^2 \qquad (3.1.21a)$$

$$r_2(\gamma) = \left(\frac{n_\gamma - 1}{n_\gamma + 1}\right) B_1(n_\gamma - 1, m_\gamma) B_1(n_\gamma, m_\gamma) \qquad (3.1.21b)$$

and

$$B_1(n,m) = \left(\frac{n+2}{n+1}\right)\left(\frac{(n+m+1)(n-m+1)}{(2n+1)(2n+3)}\right)^{\frac{1}{2}}, \quad n \geq 1 \qquad (3.1.21c)$$

The correction term has off-diagonal elements involving $\gamma^{++} = (n_\gamma + 2, m_\gamma)$, $\gamma^{+} = (n_\gamma + 1, m_\gamma)$, $\gamma^{--} = (n_\gamma - 2, m_\gamma)$ and $\gamma^{-} = (n_\gamma - 1, m_\gamma)$ and is multiplied by the long wave correction (Helmholtz) parameter

$$N = (2\Omega a)^2 / gH^* \qquad (3.1.22a)$$

The first term on the RHS is the advective term where

($L_{\gamma\beta\alpha}$) is the spectral coupling integral defined by Platzman (1962) and written here as

$$L_{\gamma\beta\alpha} = \frac{-i}{4\pi} \int_0^{2\pi} \int_{-\pi/2}^{\pi/2} \bar{Y}_\gamma J(Y_\beta, Y_\alpha) \cos\phi \, d\phi d\lambda \quad (3.1.22b)$$

The second term on the RHS is the planetary vorticity advection (beta effect) and the third term on the RHS is the generalized orography where

$$T_{\gamma\beta\delta} = B_1(\gamma^-) L_{\gamma-\beta\delta} + \left(\frac{n_\gamma}{n_\gamma + 2}\right) B_1(\gamma) L_{\gamma+\beta\delta} \quad (3.1.22c)$$

is a sum of two coupling integrals weighted by the functions given in (3.1.21c). This term is multiplied by

$$M = a/H^* \quad (3.1.22d)$$

The fourth term on the RHS is the frictional decay and the fifth term involves the mean/anomaly interactions. The last term is the projection of the inhomogeneous forcing (S) onto the spherical harmonics.

3.2. The EOF model

a) EOF expansion and model coefficients

The formulation in terms of EOF's is done completely analagously to the spectral approach. The spectral quantities in (3.1.20) are expanded in the form

$$\psi_\gamma(t) = \sum_k z_k(t) e_k(\gamma) \tag{3.2.1a}$$

$$S_\gamma = \sum_k z_k^* e_k(\gamma) \tag{3.2.1b}$$

where the z_k are the real PC's and $e_k(\gamma)$ are the complex spectral EOF's satisfying

$$e_k(\bar{\gamma}) = \bar{e}_k(\gamma) \tag{3.2.2}$$

The bar indicates a complex conjugate where $\bar{\gamma} = (n_\gamma, -m_\gamma)$.

Substituting (3.2.1) into (3.1.20), multiplying by $\bar{e}_k(\gamma)$ and summing over γ leads to the following system of real prognostic equations for the PC's.

$$\underbrace{\sum_j (a_{kj} + Nu_{kj})\dot{z}_k}_{A} = \underbrace{\sum_i \sum_j z_i z_j d_{kji}}_{B} + \underbrace{(1+\varepsilon) \sum_j z_j g_{kj}}_{C}$$

$$\underbrace{+ M \sum_j z_j f_{kj}}_{D} + \underbrace{\sum_j z_j r_{kj}}_{E} \underbrace{- \kappa \sum_j z_j a_{kj}}_{F} + \underbrace{z_k^*}_{G} \qquad (3.2.3)$$

$$k = 1,2,\ldots$$

The PC tendency term (A) is composed of two parts. The first part derives from the diagonal spectral tendency term $c_\gamma \dot{\psi}_\gamma$ of (3.1.20) and involves the coefficients

$$a_{kj} = \sum_\gamma c_\gamma \bar{e}_k(\gamma)\ e_j(\gamma) \qquad (3.2.4a)$$

These coefficients form a diagonally dominant symmetric positive definite matrix. The second part is the PC form of the generalized long wave correction term where

$$u_{kj} = \sum_\gamma \{r_1(\gamma)\ e_j(\gamma) + r_2(\gamma^+)\ e_j(\gamma^{++}) + r_2(\gamma^-)\ e_j(\gamma^{--})\}\bar{e}_k(\gamma) \qquad (3.2.4b)$$

The matrix formed by these coefficients is also symmetric and shows a tendency for the diagonal terms to be dominant.

The advective term (B) is quadratically nonlinear in the PC's and involves the coefficients

$$d_{kji} = \frac{i}{2} \sum_{\gamma} \sum_{\alpha} \sum_{\beta} \bar{e}_k(\gamma)\, e_j(\beta)\, e_i(\alpha)(c_\beta - c_\alpha)L_{\gamma\beta\alpha} \qquad (3.2.4c)$$

These are interpreted as EOF interaction coefficients even though the tendency term is not strictly diagonal. The interactions involve linear combinations of the spectral interaction coefficients, $(c_\beta - c_\alpha)L_{\gamma\beta\alpha}$, weighted by the elements of the participating EOF's. The only nonzero terms in the triple summation are those which satisfy the spectral selection rules (see Platzman, 1962). These rules are reflected in the EOF interactions by the following relations

$$d_{kji} + d_{jki} + d_{ijk} = 0 \qquad (3.2.4d)$$

$$d_{kji} = d_{kij} \qquad (3.2.4e)$$

which imply that, in general, the only trivial interaction is $d_{kkk} = 0$.

The beta term (C) is linear in the PC's and the coefficients

$$g_{kj} = i \sum_{\gamma} m_\gamma \bar{e}_k(\gamma)\, e_j(\gamma) \qquad (3.2.4f)$$

are inner products of the EOF's weighted by zonal wave

number m_γ. These coefficients form an antisymmetric matrix and satisfy $g_{kk} = 0$. The latter property is a result of the fact that the EOF's are constrained to a flip-flop type behavior and therefore a single EOF cannot be affected by the beta term which causes features to propagate.

The generalized orography term (D) involves the coefficients

$$f_{kj} = i \sum_{\gamma} \sum_{\delta} \sum_{\beta} h_\delta \, \bar{e}_k(\gamma) \, e_j(\beta) \, T_{\gamma\beta\delta} \qquad (3.2.4g)$$

This term is similar to the advective term (B) where the ith EOF has been replaced by the orographic spectral coefficient h_δ. The matrix formed by these coefficients shows a tendency for antisymmetry and it is shown in Appendix B that when the advection of planetary vorticity by the divergent wind is neglected, f_{kj} reduces to an antisymmetric form.

The linear term involving interactions between the mean flow and EOF anomalies (E) is composed of two parts. The first is the EOF advection of the mean flow vorticity where

$$rl_{kj} = i \sum_{\gamma} \sum_{\alpha} \sum_{\beta} (-c_\alpha \psi^s_\alpha) \, \bar{e}_k(\gamma) \, e_j(\beta) L_{\gamma\beta\alpha} \qquad (3.2.4h)$$

This term is identical in form to the simplified orography (see Appendix B) where now the mean flow vorticity ($-c_\alpha \psi^s_\alpha$) plays the role of the orography and the matrix of coefficients is again antisymmetric. Figure 20 shows the mean flow vorticity or what may be called a "dynamic orography" for the winter season. Here the major "mountains" are along the east coasts of North America and Asia and the subtropics are characterized by extensive "valleys". The relative importance of the orography (see Figure 1) and dynamic orography in contributing to the PC tendency depends on the factor M given in (3.1.22d) and is determined in 3.3 by regression.

The second part of E is the mean flow advection of the EOF vorticity where

$$r2_{kj} = i \sum_\gamma \sum_\alpha \sum_\beta c_\beta \psi^s_\alpha \bar{e}_k(\gamma)\, e_j(\beta) L_{\gamma\beta\alpha} \qquad (3.2.4i)$$

The matrix of coefficients for this term has neither symmetry or antisymmetry properties. One may combine rl_{kj} and $r2_{kj}$ such that

$$r_{kj} = i \sum_\gamma \sum_\alpha \sum_\beta \psi^s_\alpha \bar{e}_k(\gamma)\, e_j(\beta)(c_\beta - c_\alpha) L_{\gamma\beta\alpha} \qquad (3.2.4j)$$

where $r_{kj} = rl_{kj} + r2_{kj}$, making the similarity between

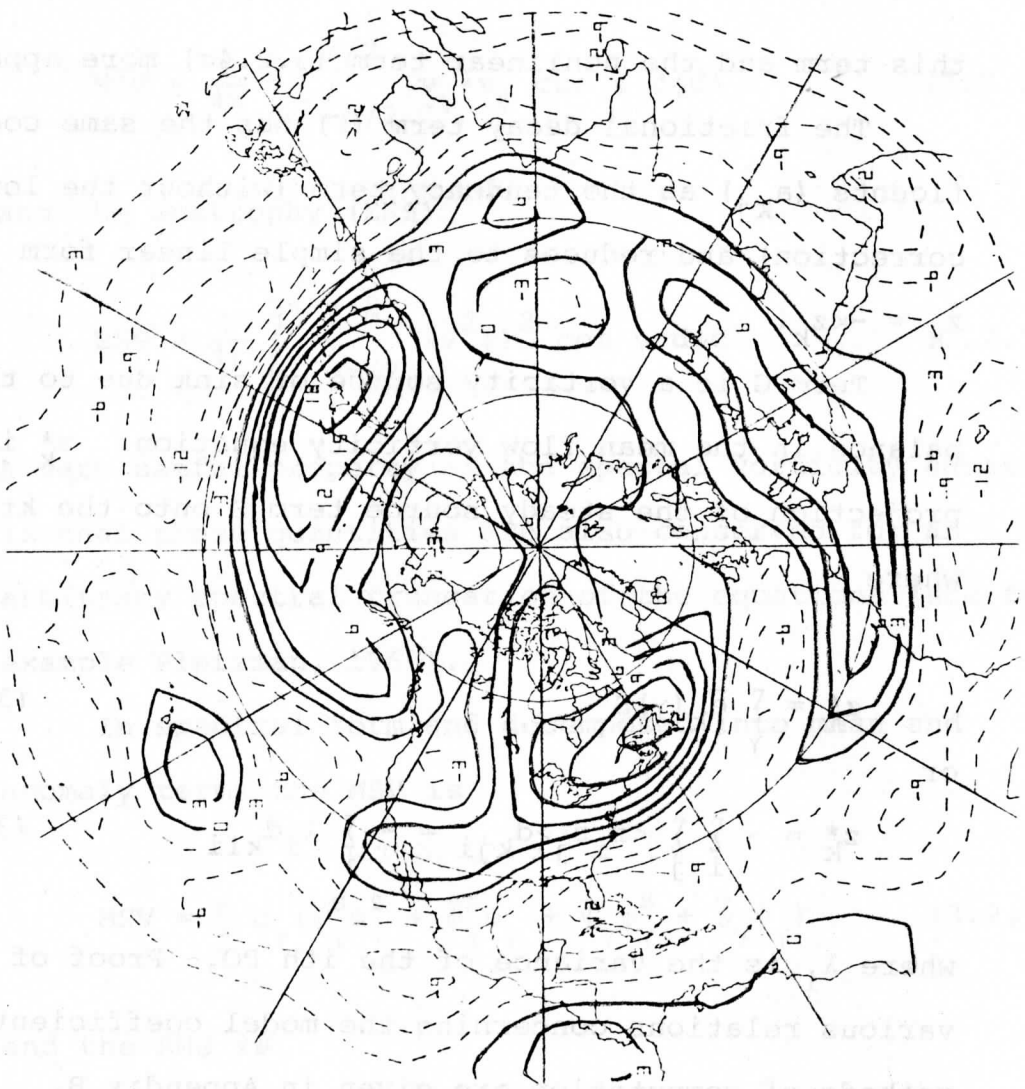

Figure 20. The climatological winter mean flow vorticity or "dynamic orography". Units: non-dimensional, contour interval is 3×10^{-5}.

this term and the nonlinear term (3.2.4c) more apparent.

The frictional decay term (F) has the same coefficents (a_{kj}) as the tendency term (without the long wave correction) and reduces to the simple linear form $\dot{z}_k = -\kappa z_k$.

Term G is a vorticity source or sink due to the imbalance in the mean flow vorticity equation. z_k^* is the projection of the steady source term S onto the kth EOF where

$$z_k^* = \sum_\gamma \bar{e}_k(\gamma) S_\gamma \qquad (3.2.4k)$$

or

$$z_k^* = -\sum_i \sum_j \langle z_i z_j \rangle d_{kji} = -\sum_i \lambda_i d_{kii} \qquad (3.2.4l)$$

where λ_i is the variance of the ith PC. Proof of the various relations concerning the model coefficients and methods of computation are given in Appendix B.

b) Integral constraints and energy sources

Two important conservative quantities for the two dimensional vorticity equation (when only advection and the beta effect are included) are the mean energy or mean square nondivergent velocity (MSV)

$$MSV = \frac{1}{4\pi} \int_0^{2\pi} \int_{-\pi/2}^{\pi/2} \underset{\sim}{v}_\psi \cdot \underset{\sim}{v}_\psi \cos\phi \, d\phi d\lambda \qquad (3.2.5a)$$

and the enstrophy (ENS)

$$ENS = \frac{1}{4\pi} \int_0^{2\pi} \int_{-\pi/2}^{\pi/2} (\nabla^2\psi)^2 \cos\phi \, d\phi d\lambda \qquad (3.2.5b)$$

A very useful property of the spectal vorticity equation is that these quantities are also conserved for an arbitrary spectral truncation of the equations (see for example Platzman, 1960).

In spectral form and decomposed into mean and anomaly terms the MSV is

$$MSV = \sum_\gamma c_\gamma (\bar{\psi}^s_\gamma \psi^s_\gamma + \bar{\psi}^s_\gamma \psi_\gamma + \bar{\psi}_\gamma \psi^s_\gamma + \bar{\psi}_\gamma \psi_\gamma) \qquad (3.2.6a)$$

and the ENS is

$$ENS = \sum_\gamma c^2_\gamma (\bar{\psi}^s_\gamma \psi^s_\gamma + \bar{\psi}^s_\gamma \psi_\gamma + \bar{\psi}_\gamma \psi^s_\gamma + \bar{\psi}_\gamma \psi_\gamma) \qquad (3.2.6b)$$

where ψ_γ and ψ^s_γ denote the stream function associated with the anomalies and the seasonal cycle, respectively. The ensemble averages of these quantities are

$$\langle MSV \rangle = \sum_\gamma c_\gamma \, \bar{\psi}^s_\gamma \psi^s_\gamma + c_\gamma \langle \bar{\psi}_\gamma \psi_\gamma \rangle \qquad (3.2.7a)$$

and

$$\langle ENS \rangle = \sum_{\gamma} c_{\gamma}^2 \, \bar{\psi}_{\gamma}^{s} \psi_{\gamma}^{s} + c_{\gamma}^2 \langle \bar{\psi}_{\gamma} \psi_{\gamma} \rangle \qquad (3.2.7b)$$

In the present study the quantities of interest are the MSV and ENS associated with the anomalies alone. Therefore, the anomaly MSV and ENS are defined as

$$MSV \equiv \sum_{\gamma} c_{\gamma} \, \bar{\psi}_{\gamma} \psi_{\gamma} = \sum_{k} \sum_{j} a_{kj} z_k z_j \qquad (3.2.8a)$$

and

$$ENS \equiv \sum_{\gamma} c_{\gamma}^2 \, \bar{\psi}_{\gamma} \psi_{\gamma} = \sum_{k} \sum_{j} b_{kj} z_k z_j \qquad (3.2.8b)$$

where

$$a_{kj} = \sum_{\gamma} c_{\gamma} \, \bar{e}_k(\gamma) \, e_j(\gamma) \qquad (3.2.8c)$$

$$b_{kj} = \sum_{\gamma} c_{\gamma}^2 \, \bar{e}_k(\gamma) \, e_j(\gamma) \qquad (3.2.8d)$$

and one should keep in mind that at any instant in time the complete quantities are defined by (3.2.6).

One of the peculiarities of the EOF model is that the truncated model is not unique in the sense that

multiplying (3.1.20) by a function of γ will lead to different solutions in the EOF domain. Depending upon exactly how the spectral model is formulated, the above integral quantities may or may not be conserved for the EOF model ((3.2.3) with only terms B and C and without the long wave correction). When all the EOF's are included (in this case a total of 135) this is not the case since the EOF transformation is simply an orthogonal coordinate rotation. The key to the integral constraints for the complete model is the dual orthogonality (2.2.12) of the EOF's which is only exactly achieved by including all possible components. However, as discussed below, by making a judicious choice for the PC tendency formulation it is possible to achieve either energy or enstrophy conservation (but not both) for an arbitrary EOF truncation.

One way to formulate the tendency term is first to divide through by c_γ in (3.1.20). This leads to a diagonal tendency term; however, it also destroys the symmetry properties of the EOF interaction coefficients and neither energy or enstrophy are conserved for the truncated model (see Appendix C).

A second formulation is achieved by not dividing through by c_γ in (3.1.20). If the tendency term is then

projected onto the EOF's as

$$\sum_{\gamma} \bar{e}_k(\gamma) \{c_\gamma \dot{\psi}_\gamma\} \tag{3.2.9a}$$

this leads to tendency coefficients (3.2.8c) which are related to the energy. It is shown subsequently that such truncated models will conserve energy and this is the approach taken in formulating (3.2.3).

A third approach is first to multiply (3.1.20) by c_γ so that the tendency has the form

$$\sum_{\gamma} \bar{e}_k(\gamma) \{c_\gamma^2 \dot{\psi}_\gamma\} \tag{3.2.9b}$$

In this form the tendency term involves coefficients (3.2.8d) which are related to the enstrophy and it is shown in Appendix C that truncated models of this form will conserve enstrophy.

In order to show that the present formulation conserves energy, the MSV tendency is written as

$$\frac{1}{2} \frac{d}{dt} (\text{MSV}) = \sum_k z_k \{\sum_j a_{kj} \dot{z}_j\} \tag{3.2.10}$$

and the various terms on the RHS of (3.2.3) are substituted for the term in braces. For the nonlinear term

this becomes

$$\sum_k \sum_j \sum_i z_k z_j z_i \, d_{kji} \qquad (3.2.11a)$$

which sums to zero identically for any truncation because by (3.2.4d-e) all permutations of d_{kji} sum to zero. For the beta term, (3.2.10) becomes

$$\sum_k \sum_j z_k z_j g_{kj} \qquad (3.2.11b)$$

which sums to zero for any truncation, this time because of the antisymmetry of the g_{kj} (i.e. $g_{kj} = -g_{jk}$). Similarly for the term involving EOF advection of the mean flow vorticity (rl_{kj}).

Potential energy sources or sinks include the generalized orography

$$\sum_k \sum_j z_k z_j f_{kj} \neq 0 \qquad (3.2.11c)$$

the mean flow advection of EOF vorticity

$$\sum_k \sum_j z_k z_j \, r2_{kj} \neq 0 \qquad (3.2.11d)$$

the dissipation term

$$-\sum_k \sum_j a_{kj} z_k z_j \leq 0 \qquad (3.2.11e)$$

and the inhomogeneous forcing

$$\sum_k \sum_j z_k z_j^* \neq 0 \qquad (3.2.11f)$$

The tendency for the f_{kj} to be antisymmetric indicates (3.2.11c) may not be an important energy source. It will be shown in 4.2 that (3.2.11d) is an important energy source, primarily for the dominant PC's. Since a_{kj} forms a positive definite matrix, (3.2.11e) is always an energy sink. The inhomogeneous forcing may be a source or sink depending on the sign of the inner product between $\underset{\sim}{z}$ and $\underset{\sim}{z}^*$. This term will be described in more detail in 4.3a.

3.3. The regression model

The EOF model (3.2.3) contains several undetermined quantities ($N, M, \varepsilon, \kappa$) which appear in the equations as a result of the PBL parameterizations. The question that the regression approach attempts to answer is: how important are the boundary layer processes to the tendency of the PC's at the 500 mb level? Or, more specifically, what percent of the remaining observed variance in the PC tendency do the boundary terms explain after all the

other terms have been taken into account?

In order to answer this question (3.2.3) is re-written in the form

$$\underset{\sim}{Y} = \beta_1 \underset{\sim}{X}_1 + \beta_2 \underset{\sim}{X}_2 + \beta_3 \underset{\sim}{X}_3 \qquad (3.3.1)$$

where

$$Y_k = \sum_k a_{kj}\dot{z}_j - \{\sum_i \sum_j z_i z_j d_{kji} + \sum_j (g_{kj} + r_{kj}) z_j + z_k^*\} \qquad (3.3.2a)$$

$$X_{1k} = \sum_j af_{kj} z_j - \sum_j \frac{(2\Omega a)^2}{g} u_{kj} z_j \qquad (3.3.2b)$$

$$X_{2k} = \sum_j g_{kj} z_j \qquad (3.3.2c)$$

$$X3_k = \sum_j \frac{1}{2\Omega} a_{kj} z_j \qquad (3.3.2d)$$

$$\beta_1 = H^{*-1} \qquad (3.3.2e)$$

$$\beta_2 = \varepsilon \qquad (3.3.2f)$$

and

$$\beta_3 = (-c_D H^{*-1}) \equiv -2\Omega\kappa \qquad (3.3.2g)$$

An important assumption implicit in the model formulation is that the various parameters involved in the PBL parameterizations are not a function of the PC's. For example, it is assumed that the same frictional decay rate, κ, holds for the first PC as well as the fortieth PC. Therefore, in the context of the estimation procedure, one should treat each component of $\underset{\sim}{Y}$ in (3.3.1) as a sample, rather than the entire vector itself. The problem may then be posed as a standard univariate multiple regression equation

$$\underset{\sim}{Y} = X\underset{\sim}{\beta} + \underset{\sim}{\varepsilon} \tag{3.3.3}$$

where $\underset{\sim}{Y}$ is a vector of length (r × n) where r is the number of observations and n is the number of PC's retained. X is the (r × n) × 3 design matrix involving 3.3.2b-d and $\underset{\sim}{\beta}$ is the (3 × 1) vector of parameters. $\underset{\sim}{\varepsilon}$ is the (r × n) × 1 error vector which is assumed normally distributed as

$$\underset{\sim}{\varepsilon} \sim N(\underset{\sim}{0}, V\sigma^2) \tag{3.3.4}$$

The regression procedure involves the minimization of the mean square error which leads to estimates for $\underset{\sim}{\beta}$ and σ^2 if the (n × r) × (n × r) matrix (V) is known

(see e.g. Draper and Smith, 1966, pp. 77-81). For the present analysis it has been assumed that the errors are uncorrelated in time and the variances and covariances of the errors are not a function of time. Therefore V is written as

$$V = \begin{bmatrix} \Sigma & & & \\ & \Sigma & & \\ & & \ddots & \\ & & & \Sigma \end{bmatrix} \qquad (3.3.5)$$

where Σ is the $(n \times n)$ matrix of error variances and covariances. In the following results only two forms of Σ have been tested. One is that Σ is the identity matrix and the other assumes that the covariances are zero but the error variances are proportional to the PC variances such that

$$\Sigma = \begin{bmatrix} \lambda_1 & & & \\ & \lambda_2 & & \\ & & \ddots & \\ & & & \lambda_n \end{bmatrix} \qquad (3.3.6)$$

The latter form of ξ leads to the weighted least squares problem (e.g. Draper and Smith, loc. cit.).

The PC are filtered with a five day running average to eliminate the high frequency fluctuations and provide a better estimate of the observed tendencies which, in turn, are computed from a two day difference of the filtered data. The effects of the smoother are shown in Figure 21 for selected PC time series. These results suggest that the filter does an adequate job of reducing the short time scale fluctuations without seriously reducing the amplitude of the longer time scale components. All the terms in (3.3.3) except z_k^* are computed from the filtered data sampled at 5 day intervals for the winter seasons of 1967-75/76.

Results of the regression are summarized in Table 1 for various truncations. A test of the overall regression equation based on an F-test (see Draper and Smith, loc. cit.) showed significance at the 95% level for all the models shown. The first four rows of Table 1 show results computed with V = I and the long wave correction term removed from (3.3.2b). A major result of this analysis is that the boundary terms are found to explain only a small amount of the observed variance. For example, with 25 PC's included in the model the percent

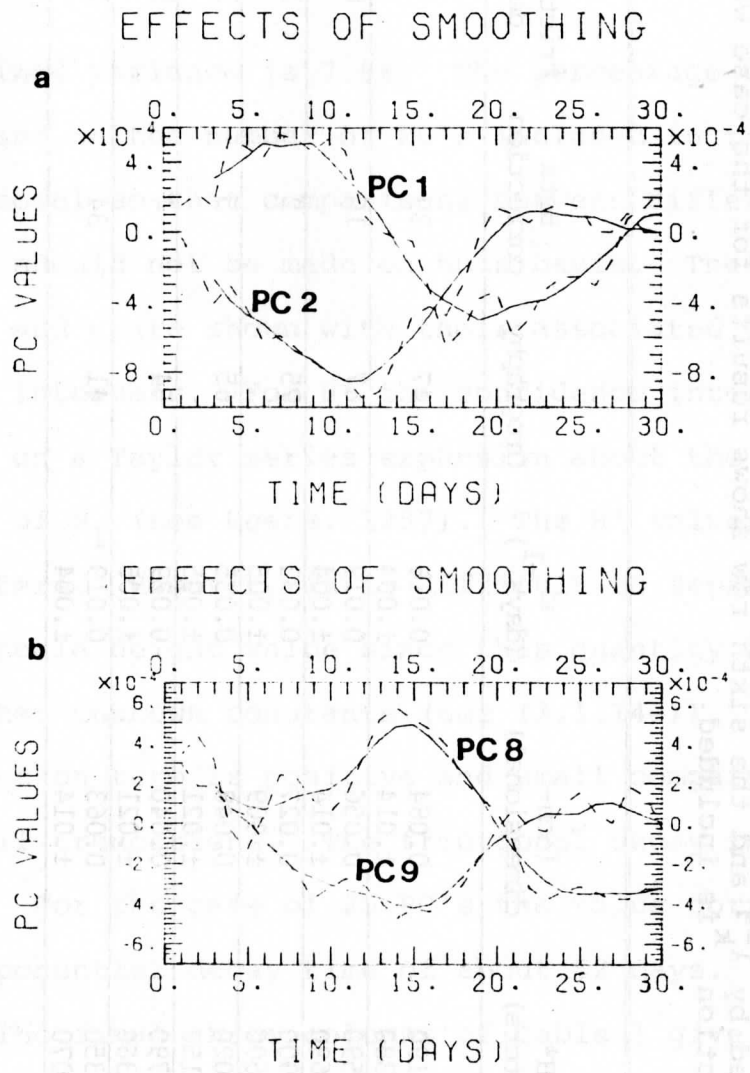

Figure 21. Effects of smoothing on the evolution of (a) the first and second PC's and (b) the eighth and ninth PC's. The dashed lines represent the projection of the daily 500 mb anomaly fields (Jan. 1-30, 1967) onto the EOF's computed from 10-day averaged anomalies. The solid lines are a result of a 5-day running average applied to the unsmoothed PC's. Units: non-dimensional.

Table 1. Summary of the regression results. The last three columns represent the additional sum of squares gained (as a percent of the final sum of squares) when the term in question is the last to enter the model. Results for the fifth row are for data weighted by $\lambda_k^{-\frac{1}{2}}$ and the sixth row shows results for the case when the long wave correction is included.

	Number of PC's	Percent Variance	H* (meters)	ε (non-dimensional)	κ ($days^{-1}$)	Orography	Beta correction	Frictional decay
1.	40	4.3	23190 ±3380	0.084 ±.014	0.016 ±.004	47	39	5
2.	25	7.6	14590 ±1690	0.056 ±.014	0.019 ±.004	67	15	6
3.	12	12.5	9900 ±600	0.027 ±.009	0.033 ±.005	75	2	15
4.	10	14.8	9020 ±1150	0.048 ±.021	0.035 ±.005	65	5	14
5.	10	12.9	9790 ±1360	0.040 ±.021	0.029 ±.005	64	4	10
6.	25	4.3	25350 ±5070	0.063 ±.014	0.019 ±.004	41	34	10

explained variance is 7.6%. The percentage calculation is based on the number of PC's included in the regression model so that comparisons between different truncations should not be made on this basis. The values of H*, ε and κ are shown with their associated 95% confidence intervals. For H* the confidence intervals are based on a Taylor series expansion about the computed value of β_1 (see Beers, 1957). The H* values have units of meters. However, it is difficult to separate out a true scale height value since this quantity is weighted by other unknown constants (see (3.1.14e)). The beta correction term is positive and small compared to one, for all truncations. The frictional decay is also very weak. For the case of 25 PC's the value corresponds to an exponential decay time of about 52 days.

The final three columns of Table 1 give an indication of the relative importance of the boundary terms. The numbers represent the additional sum of squares gained (as a percent of the final regression sum of squares) when the term in question is the last to enter the model. This suggests that, in general, the orography term is the most important predictor while the relative importance of the beta correction and frictional decay depends strongly on the level of EOF truncation.

The fifth row of Table 1 shows the case of weighted least squares ($\sharp$ given by (3.3.6)). For ten PC's it is found that the percent variance is actually smaller and the parameter values are not significantly different. The sixth row shows the case of 25 PC's when the long wave correction term is included in the model. The percent variance explained is reduced by almost one half suggesting that the long wave correction should not be included. This is contrary to the results of the Kruse (1983) study in which it was found that the inclusion of baroclinic effects leads to large values of the surface correction parameter. In order to understand this result, an effective total wavenumber for the EOF's is computed from the ratio of the enstrophy (3.2.5b) to energy (3.2.5a) given by

$$\frac{b_{kk}}{a_{kk}} = \sum_{\gamma} c_{\gamma}^2 \bar{e}_k(\gamma)\, e_k(\gamma) \Big/ \sum_{\gamma} c_{\gamma} \bar{e}_k(\gamma)\, e_k(\gamma) \equiv c_k \qquad (3.3.7)$$

where $c_k \equiv n_k(n_k + 1)$ and n_k is the effective total wave number for the k^{th} EOF.

Figure 22a shows n as a function of the EOF's and Figure 22b is a table of observed versus theoretical phase speeds for various spherical harmonics (taken from Eliasen and Machenhauer, 1969). These results show that

a

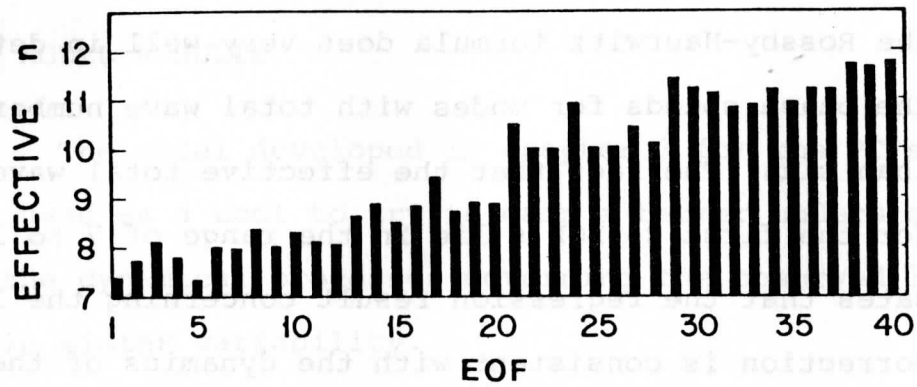

b

OBSERVED — THEORETICAL

n \ m	1	2	3	4	5	6	7	8	
1	0								-360
2	0	-9							-111
3	0	-5	-1						-48
4	-3	0	-3	1					-23
5	-3	-2	-3	1	0				-11
6	-4	-1	-1	3	1	2			-4
7	1	3	1	2	2	3	2		1
8	1	5	1	3	6	4	4	3	4
9		6	3	7	5	5	4	4	6
10			6	6	8	8	5	5	7
11				9	7	10	7	6	8
12					7	9	9	7	9
13						9	11	12	10
14							11	11	10
15								11	11

PHASE SPEEDS (°Longitude/day)

Figure 22. (a) The effective total wave numbers of the EOF's based on the ratio of ENS to MSV. (b) The mean observed phase speeds for the Northern Hemisphere 500 mb stream function (1 Oct., 1957-31 Jan., 1958) for various wave components (°long./day) and the theoretical phase speeds determined from the Rossby-Haurwitz formula assuming a solid rotating mean flow of 14 °long./day. Taken from Eliasen and Machenhauer (1969).

the Rossby-Haurwitz formula does very well in determining the phase speeds for modes with total wave number greater than six. The fact that the effective total wave numbers for the first 25 EOF's lie in the range of 7 to 12 indicates that the regression result concerning the long wave correction is consistent with the dynamics of these modes.

4. MODEL RESULTS

The model developed in chapter 3 for the PC's is now used as a tool to try to gain a better understanding of the dynamical processes governing the observed large-scale winter variability.

Section 1 deals with the complete model when all the terms except the long wave correction are included. The model is first run in a diagnostic mode where the observations are simply substituted into the model terms in order to determine their relative magnitudes as well as to examine the ability of the model to reproduce the observed tendency. Next, a simulation is made with the observed mean flow as initial conditions in order to assess the ability of the model to reproduce the atmospheric variability.

Section 2 deals with simplified linear versions of the model. First the stability of the winter mean flow is tested with respect to perturbations composed of the individual EOF patterns. Then a more complete normal mode analysis is done in order to compare the structure of these modes with the EOF's and to examine the sensitivity of the normal modes to model truncation.

Finally, in section 3 the nonlinear properties are examined in more detail. This includes a discussion of

EOF interactions, the inhomogeneous forcing, EOF's as steady states, and the possibility of multiple equilibria in highly simplified versions of the model.

4.1. The complete model

a) Variance of model terms

Figure 23 shows the standard deviations of the various terms in the model as a function of the PC's. Successive values are connected in order to make the plot more readable. The values are based on 25 PC's for nine winters (1967-74/75) of data filtered with a five day running average and sampled every fifth day. The observed tendency is computed from a centered finite difference formula spanning a 48 hour period. All other terms are computed by inserting the observed values of the PC's into the model terms every fifth day.

The comparison between the standard deviation of the model tendency (RHS of (3.2.3)) and that of the observed tendency indicates that there is a reasonable agreement particularly for the first few PC's. The dominant terms on the RHS of (3.2.3) are the mean flow/EOF interactions and the beta term. These are 1.5 to 4 times larger than the tendency term, but they are highly negatively correlated so that their sum (not shown) has

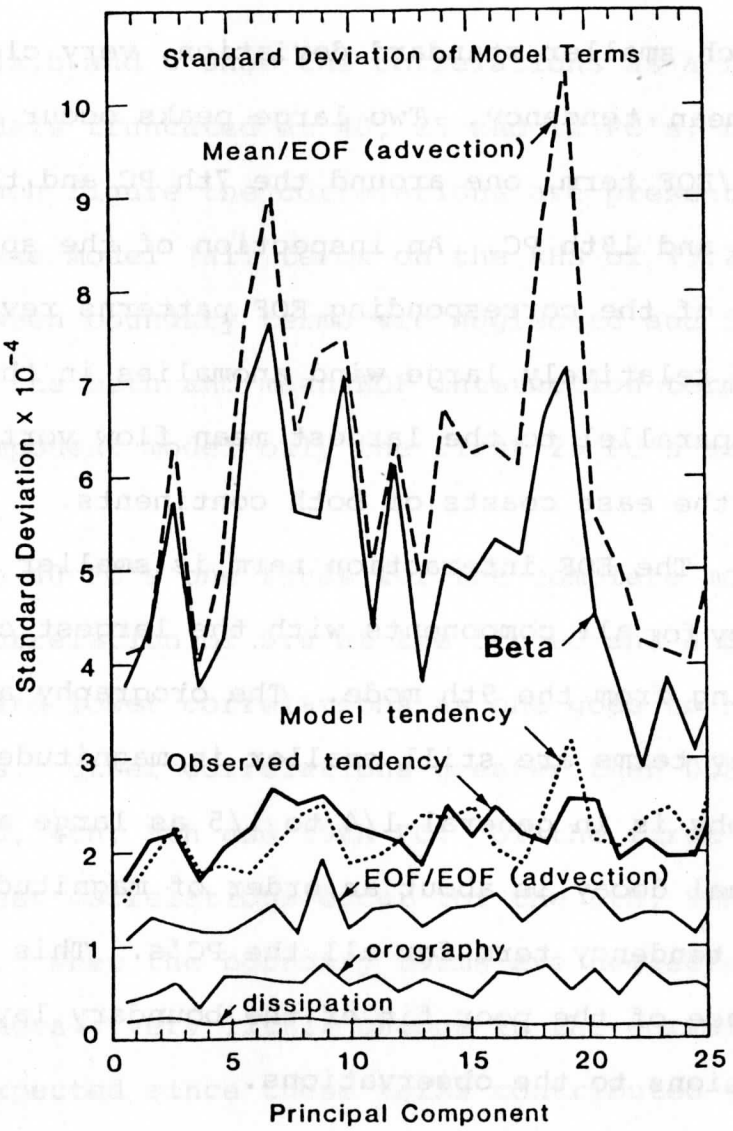

Figure 23. The standard deviation of the model terms as a function of PC for the 25 component model. The values are computed by inserting the observations (filtered with a 5 day running averaged and sampled every fifth day) into the model terms for the winters of 1967-74/75. The observed tendency is also based on the filtered data and is computed from a centered finite difference formula spanning a 48 hour period. Successive values are connected to make the plot more legible. Units: non-dimensional.

a much smaller standard deviation, very close to that of the mean tendency. Two large peaks occur in the mean flow/EOF term, one around the 7th PC and the other at the 18th and 19th PC. An inspection of the spatial distribution of the corresponding EOF patterns reveals them to have relatively large wind anomalies in the vicinity of and parallel to the largest mean flow vorticity gradients off the east coasts of both continents.

The EOF interaction term is smaller than the tendency for all components with the largest contribution coming from the 9th mode. The orography and frictional decay terms are still smaller in magnitude. The orography is in general 1/4 to 1/5 as large and the frictional decay is about an order of magnitude smaller than the tendency term for all the PC's. This is a consequence of the poor fit of the boundary layer parameterizations to the observations.

b) Tendency correlations

In order to obtain a simple measure of the forecast skill of the EOF model, correlations are computed between the observed and model tendencies for each PC. The method of computation of the various terms is identical to that of the previous section.

Figures 24a,b and c show the correlations as a function of PC for models truncated at 40, 25 and 12 PC's, respectively. In each figure the correlations are presented for the complete model (all terms on the RHS of (3.2.3)), for the case when boundary terms are neglected and finally with only the beta and mean/EOF interaction terms. For the 40 component model only the first 25 PC's are presented.

With 40 PC's one finds for the complete model a maximum correlation of 0.6 at the 5th PC and a general trend toward lower correlations as one goes to higher order PC's. Other correlations greater than 0.5 occur at the 2nd, 4th, 9th and 15th PC. Of the first 12 PC's the smallest correlations occur for the 6th, 8th and 11th PC's. When the boundary terms are neglected there is, in general, very little change in the correlations. This is expected since these terms contributed very little to the sums of squares. The 3rd, 5th and 6th PC's gain the most from the boundary terms, as measured by the improvement in the correlations. These modes have anomaly patterns which suggest some coupling to the positions of the major land masses. In particular, the sixth EOF, when superimposed on the mean flow, exhibits either a zonal wave number 4 pattern with troughs off the west

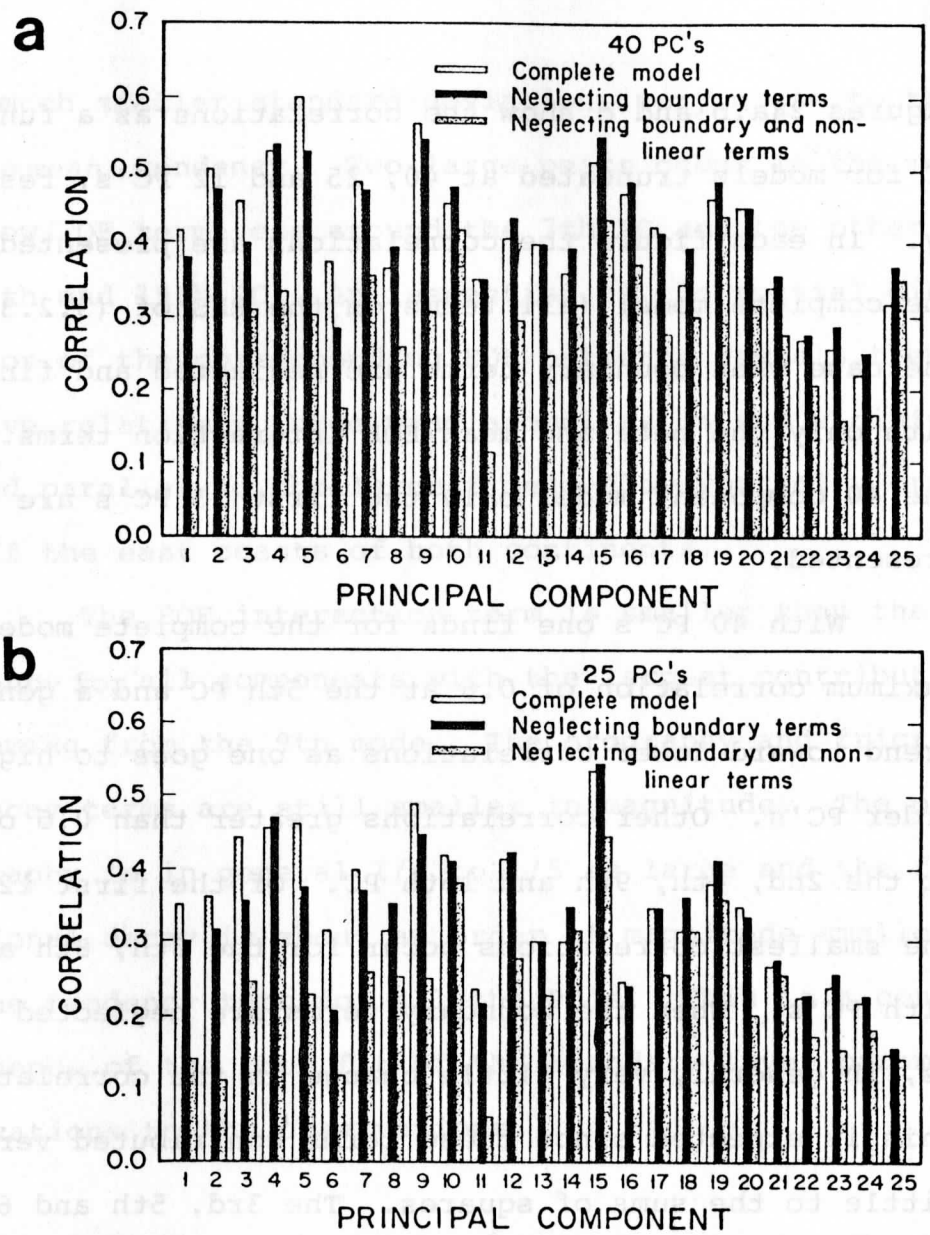

Figure 24. Correlations between the observed tendency and the tendency computed from the model, as a function of PC for (a) the 40 component model and (b) the 25 component model. The three model versions compared are (1) the complete model as determined from regression (2) the model which neglects all boundary terms and (3) the linear version of the model which also excludes the boundary terms.

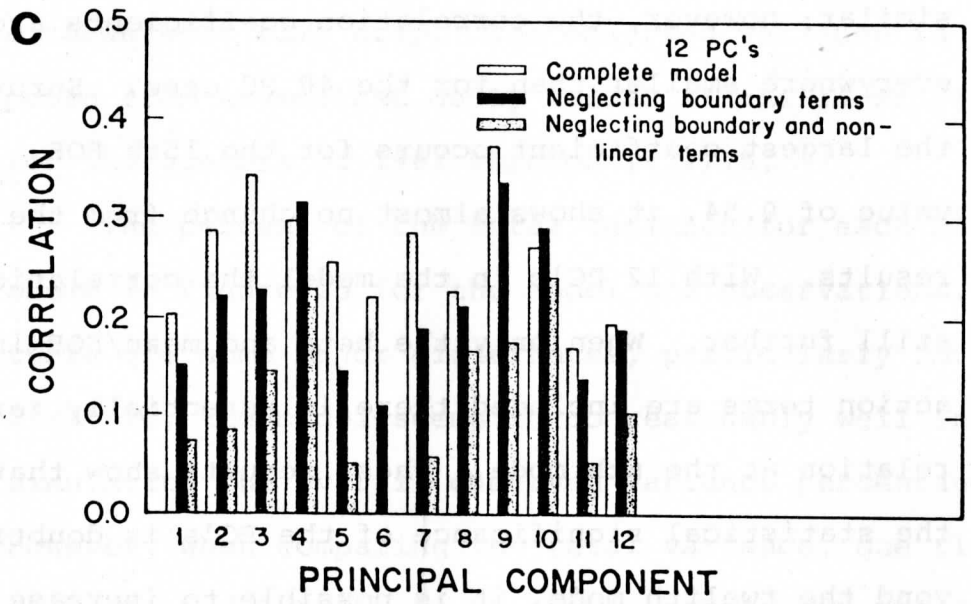

Figure 24c. As in Fig. 24a, except for the 12 component model.

coast of North America and over the western part of Asia, or, a zonal wave number 2 pattern with ridges in these areas. With only the beta and mean/EOF interaction terms there is a dramatic drop in the correlations. This indicates the importance of the EOF interactions particularly for EOF's 2, 4, 5, 9 and 11, all showing a reduction of more than 0.2 in the correlation coefficient. Other modes such as the 10th, 19th and 25th show very little improvement when nonlinear interactions are included.

For the 25 component model the results are very

similar; however, the correlation coefficients are almost everywhere smaller than for the 40 PC case. Surprisingly, the largest coefficient occurs for the 15th EOF. With a value of 0.54, it shows almost no change from the 40 PC results. With 12 PC's in the model the correlations drop still further. When only the beta and mean/EOF interaction terms are included there is essentially zero correlation at the 6th mode. These results show that, while the statistical significance of the PC's is doubtful beyond the twelfth mode, it is possible to increase substantially the predictive skill of the model by including the higher order EOF's.

c) A winter simulation

The ability of the model to reproduce the observed climatology is measured by performing a long term integration from mean flow initial conditions and comparing the simulated PC variances with the observed. The model derived variances are computed from daily output using the last 300 days of a 365 day simulation. The model includes 25 PC's and uses the parameter values determined by regression (see 3.3). The numerical integration involves a time derivative which is approximated by a one step, fourth order Kutta scheme (Young, 1968) using

a three hour time step. The observed variance is computed from unsmoothed daily values of the first 25 PC's for the winters of 1967 through 1974/75.

The percent of the total variance for each PC is shown in Figure 25 for the model and observations. While there are some major differences, particularly for the first PC, the model seems to do reasonably well in simulating the overall observed variance percentages. However, when comparing the total variance, one finds that the model has more than twice the variance of the observations. This is, in part, due to the fact that the regression produced a very weak frictional decay rate (e-folding time of about 52 days); however, this also suggests that there are significant energy sources in the model.

A more detailed look at the simulation is presented in Figure 26. The first 165 days of the evolution of the first, second and ninth PC's (Figure 26a) shows that there is a rapid energy input into the system producing large oscillations (similar in magnitude to the observed) within the first 50 days. The important components of the kinetic energy tendency (Figure 26b) show that the dominant source is the mean flow advection of the anomalous vorticity. The contribution from the inhomo-

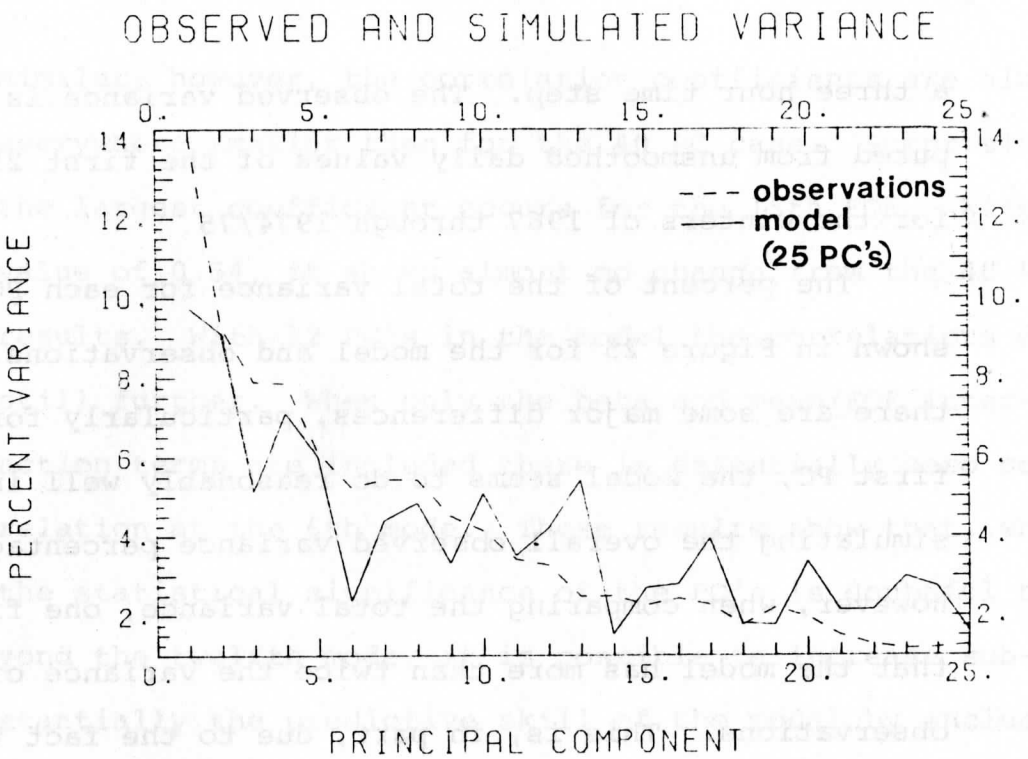

Figure 25. The percent of the total variance explained by each PC for the observations (dashed line) and the model simulation (solid line). Successive points are connected to make the plot more legible. Units: non-dimensional.

geneous forcing is closely coupled to the behavior of PC 9 (see Figure 31) and, of course, the dissipation produces a negative tendency for all times. The fact that most of the energy is obtained from the mean flow advection term indicates that the winter mean flow is barotropically unstable. This result is consistent with the recent findings of Simmons et al. (1982) in their study of the stability of the 300 mb mean flow. They suggested that barotropic instability may be a major

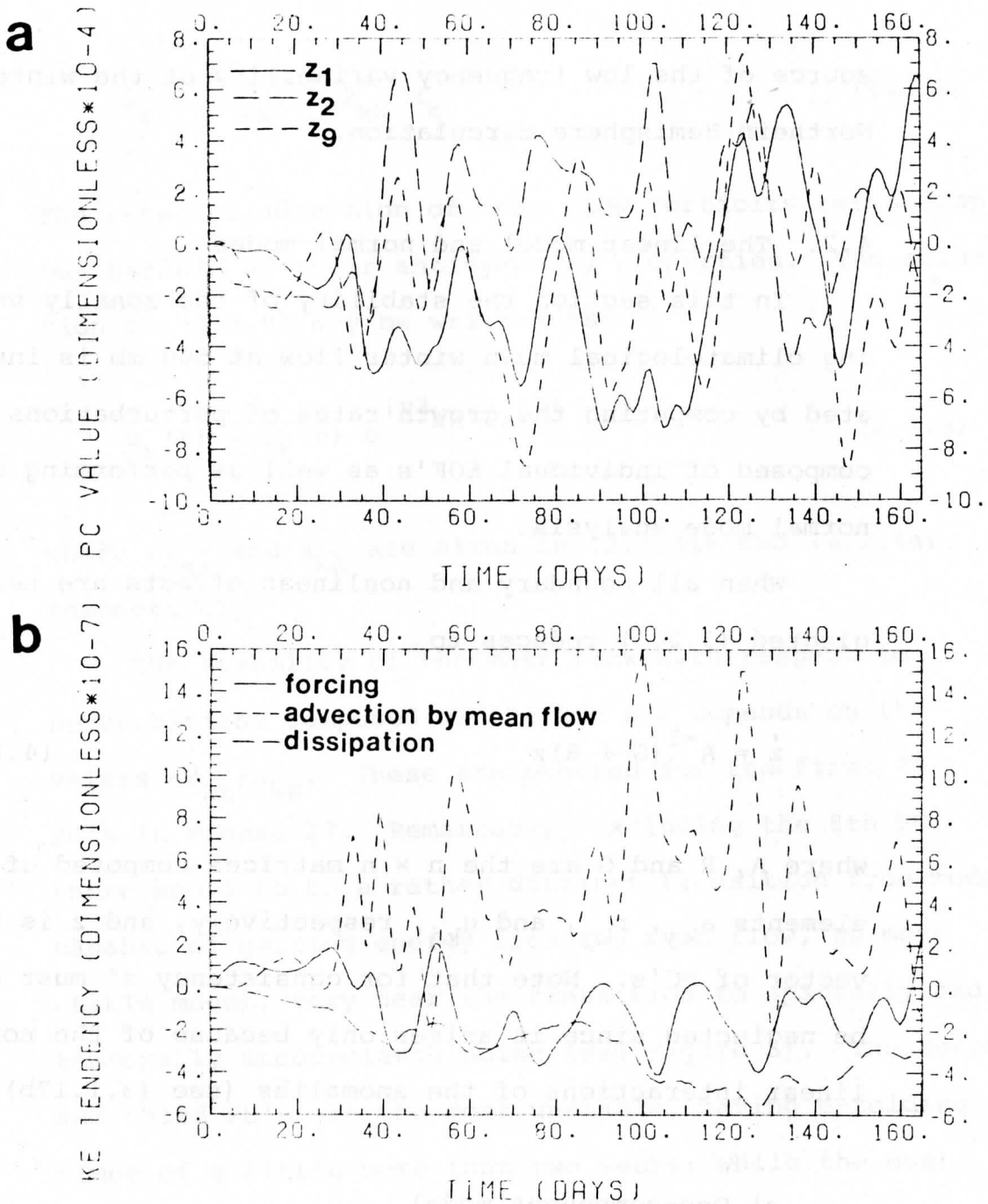

Figure 26. (a) The evolution of the first, second and ninth PC's and (b) the major contributors to the total KE tendency in a 25 component model simulation starting from mean flow initial conditions. Units: non-dimensional.

source of the low frequency variability of the wintertime Northern Hemisphere circulation.

4.2. The linear model and normal modes

In this section the stability of the zonally varying climatological mean winter flow at 500 mb is investigated by computing the growth rates of perturbations composed of individual EOF's as well as performing a normal mode analysis.

When all boundary and nonlinear effects are neglected (3.2.3) reduces to

$$\dot{\underset{\sim}{z}} = A^{-1}(G + R)\underset{\sim}{z} \qquad (4.2.1)$$

where A, R and G are the n × n matrices composed of the elements a_{kj}, r_{kj}, and g_{kj}, respectively, and $\underset{\sim}{z}$ is the vector of PC's. Note that for consistency $\underset{\sim}{z}^*$ must also be neglected since it arises only because of the nonlinear interactions of the anomalies (see (3.1.17b)).

a) One-component model

For the case when only one EOF is allowed into the model (4.2.1) becomes

$$\dot{z}_k = (a_{kk})^{-1} r2_{kk}\, z_k \qquad (4.2.2)$$

The beta and advection of mean flow vorticity terms drop out because of their antisymmetry properties. The solution to (4.2.2) may be written as

$$z_k(t) = z_k(0)\, e^{(r2_{kk}/a_{kk})t} \qquad (4.2.3)$$

where $r2_{kk}$ and a_{kk} are given in (3.2.4i) and (3.2.4a), respectively.

The stability of the mean flow with respect to perturbations composed of the kth EOF depends on the values $r2_{kk}/a_{kk}$. These are plotted for the first 25 PC's in Figure 27. Remarkably, excluding the 8th PC, there seems to be a rather distinct transition from modes capable of gaining energy from the mean flow, to more stable modes, very near the transition to spatially and temporally uncorrelated noise (see Figure 3). The second and third PC's are the most unstable, having e-folding times of a little more than two weeks; while the most stable modes are found beyond the thirtieth PC (not shown). The stability of the January 1-10 and May climatological mean flows is also examined. The former is of interest because it is representative of a more

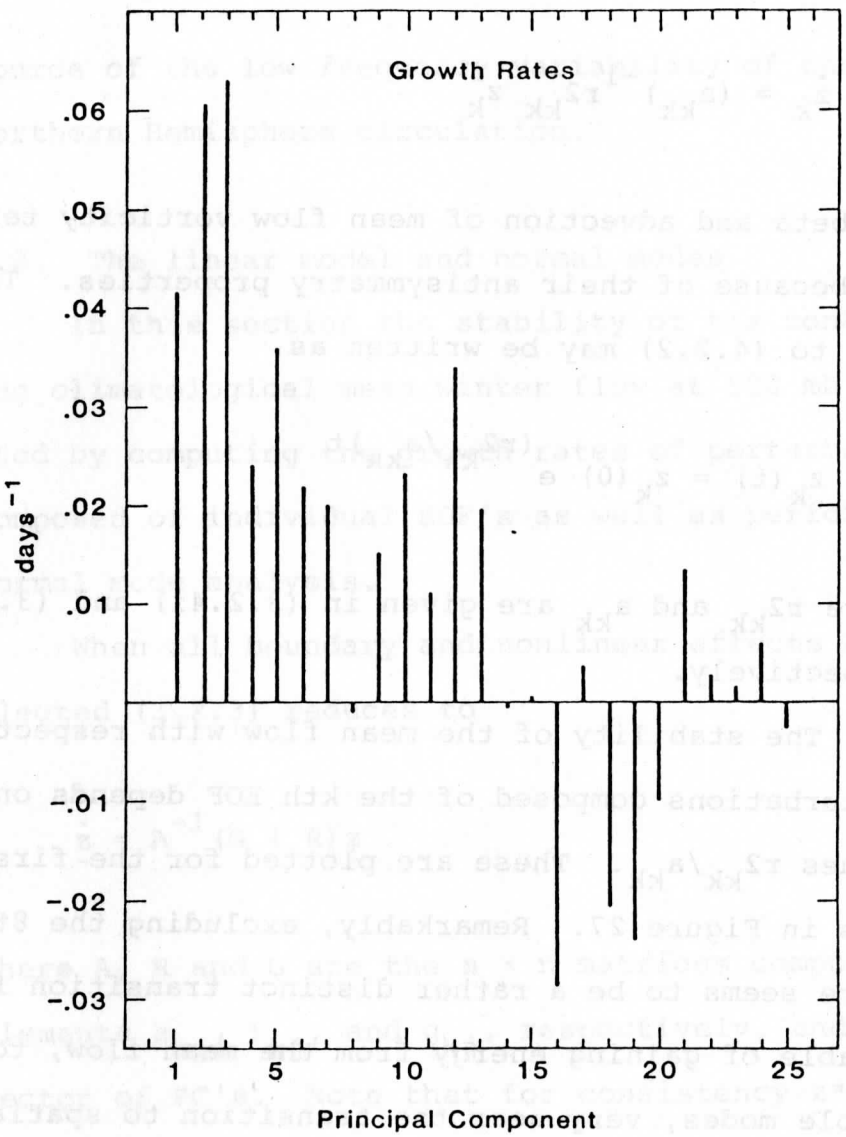

Figure 27. The growth rates of perturbations consisting of individual EOF's superimposed on the climatological mean winter flow.

intense circulation regime and the latter is of interest because it is a peak blocking month (see e.g. Brezowsky et al., 1951). Figure 28 compares the growth rates for the first 15 PC's. For the January 1-10 flow there is a general increase in the growth rates with a dramatic increase occurring for the third and twelfth PC's (9.9 and 13 day e-folding time, respectively). For the May average flow the growth rates are much reduced; in particular, the fourth and ninth PC's have essentially zero growth rates.

These results must be viewed only as measuring the potential for instability since the EOF perturbation is constrained to be fixed in space. In reality the asymmetric components of the RHS of (4.2.1) (such as those associated with the beta and advection of mean flow vorticity terms) will tend to propagate the anomalies.

Some rather general constraints on the growth rates and frequencies are expressed in theorems due to Bendixson and Pick (Bodewig, 1959, pp. 70-75). These theorems state that for a general matrix W, the eigenvalues (a + ib) are constrained such that

$$m_1 \leq a \leq M_1 \qquad (4.2.4a)$$

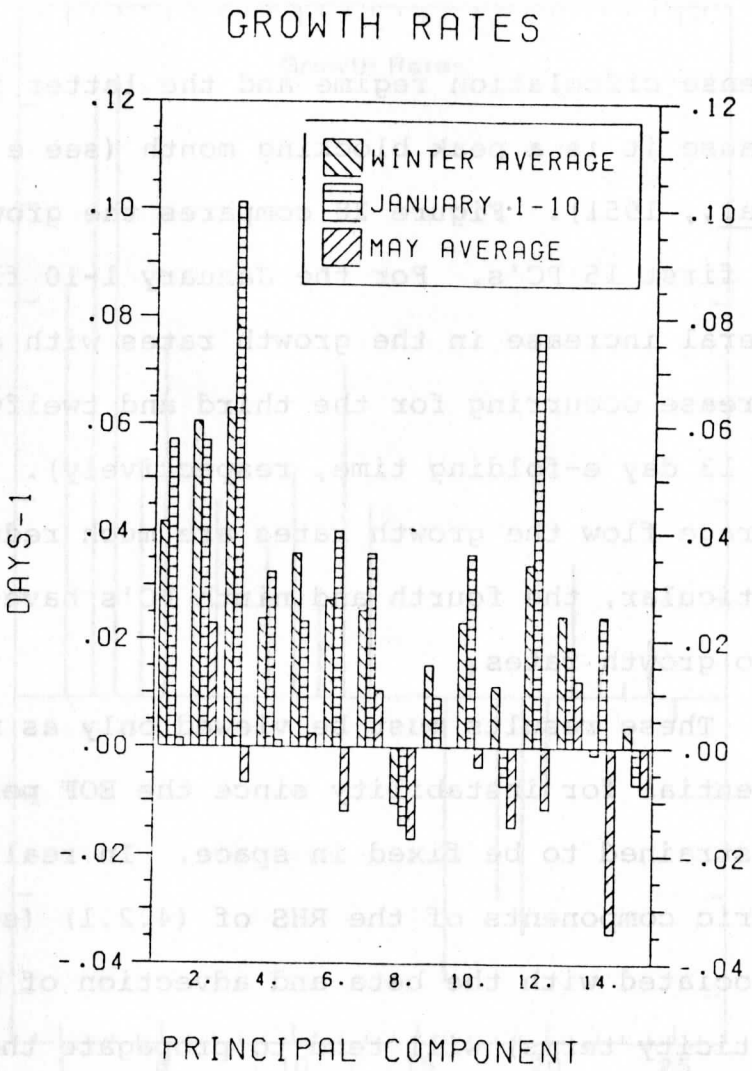

Figure 28. A comparison of the growth rates of perturbations consisting of individual EOF's superimposed on (1) the climatological mean winter flow (2) the climatological mean January 1-10 flow and (3) the climatological mean May flow.

and

$$m_2 \leq b \leq M_2 \qquad (4.2.4b)$$

where m_1 and M_1 are the smallest and largest eigenvalues of W^S and m_2 and M_2 are the smallest and largest eigenvalues of $-iW^A$. Here, W^S and W^A are the symmetric and antisymmetric components of W, respectively. In the present analysis (4.2.1), the growth rates are constrained by the eigenvalues of

$$W^S = \{A^{-1}(R + G) + (R + G)^T A^{-1}\}/2 \qquad (4.2.5a)$$

and the frequencies are constrained by the eigenvalues of

$$-iW^A = -i\{A^{-1}(R + G) - (R + G)^T A^{-1}\}/2 \qquad (4.2.5b)$$

For the case of the one dimensional model, (4.2.5a) reduces to the single value $r2_{kk}/a_{kk}$ and (4.2.5b) reduces to zero implying an infinite period. It will be shown in the next section that for the 40 component model the asymmetric terms do in fact result in the most unstable mode being fixed in space.

b) N-component model

For an arbitrary number of components the solution to (4.2.1) may be written in the vector form

$$\underset{\sim}{z}(t) = \text{EXP}\{A^{-1}(R + G)t\}\underset{\sim}{z}(0) \qquad (4.2.6)$$

Assuming distinct eigenvalues (ν_j), $\underset{\sim}{z}(0)$ is expanded in terms of the eigenvectors ($\underset{\sim}{\omega}_j$) of $A^{-1}(R + G)$ such that

$$\underset{\sim}{z}(t) = \sum_j c_j \, \underset{\sim}{\omega}_j \, e^{\nu_j t} \qquad (4.2.7)$$

where the c_j are constants which may be determined from the initial conditions.

The real normal mode solutions are

$$\underset{\sim}{z}_j(t) = e^{\nu_j^{(r)} t}\{\underset{\sim}{\omega}_j^{(r)} \cos \nu_j^{(i)} t - \underset{\sim}{\omega}_j^{(i)} \sin \nu_j^{(i)} t\} \qquad (4.2.8)$$

where $\underset{\sim}{\omega}_j = \underset{\sim}{\omega}_j^{(r)} + i\underset{\sim}{\omega}_j^{(i)}$ and $\nu_j = \nu_j^{(r)} + i\nu_j^{(i)}$

or in terms of the streamfunction

$$\psi(\lambda,\phi,t)_j = e^{\nu_j^{(r)} t}\{\cos \nu_j^{(i)} t \, (\underset{\sim}{\omega}_j^{(r)} \cdot \underset{\sim}{E}(\lambda,\phi)) - \sin \nu_j^{(i)} t \, (\underset{\sim}{\omega}_j^{(i)} \cdot \underset{\sim}{E}(\lambda,\phi))\} \qquad (4.2.9)$$

where $\underset{\sim}{E}(\lambda,\phi)$ is the vector of spatial EOF's evaluated at the point (λ,ϕ) and the dot signifies an inner product. For the case of real eigenvalues (4.2.9) reduces to

$$\psi(\lambda,\phi,t)_j = e^{\nu_j t}(\underset{\sim}{\omega}_j \cdot \underset{\sim}{E}(\lambda,\phi)) \qquad (4.2.10)$$

Figure 29 shows the spatial pattern of the fastest growing mode (e-folding time of 16.7 days) for the 40 component model. For reasons of computational convenience only the contributions from the first 25 PC's are actually plotted. The mode is fixed in space and is dominated by the 2nd, 4th and 12th EOF's with only minor contributions beyond the 25th EOF. Large anomaly centers are located in regions of mean flow diffluence (see Figure 12a) associated with the Asian and North American east coast jets together with weaker anomalies of opposite sign to the south. Another large anomaly is located over western Asia on the lee side of a mean trough in this area with a weaker anomaly of opposite sign over the Mediterranean.

An analysis of the 500 mb winter mean flow shows that the zonally averaged state is barotropically stable (absolute vorticity has no extrema). This suggests that the zonally asymmetric components of the mean state which account for less than 16% of the mean flow kinetic energy and are primarily composed of zonal wave numbers 1, 2 and 3 (see Figure 12b) are the key sources of instability.

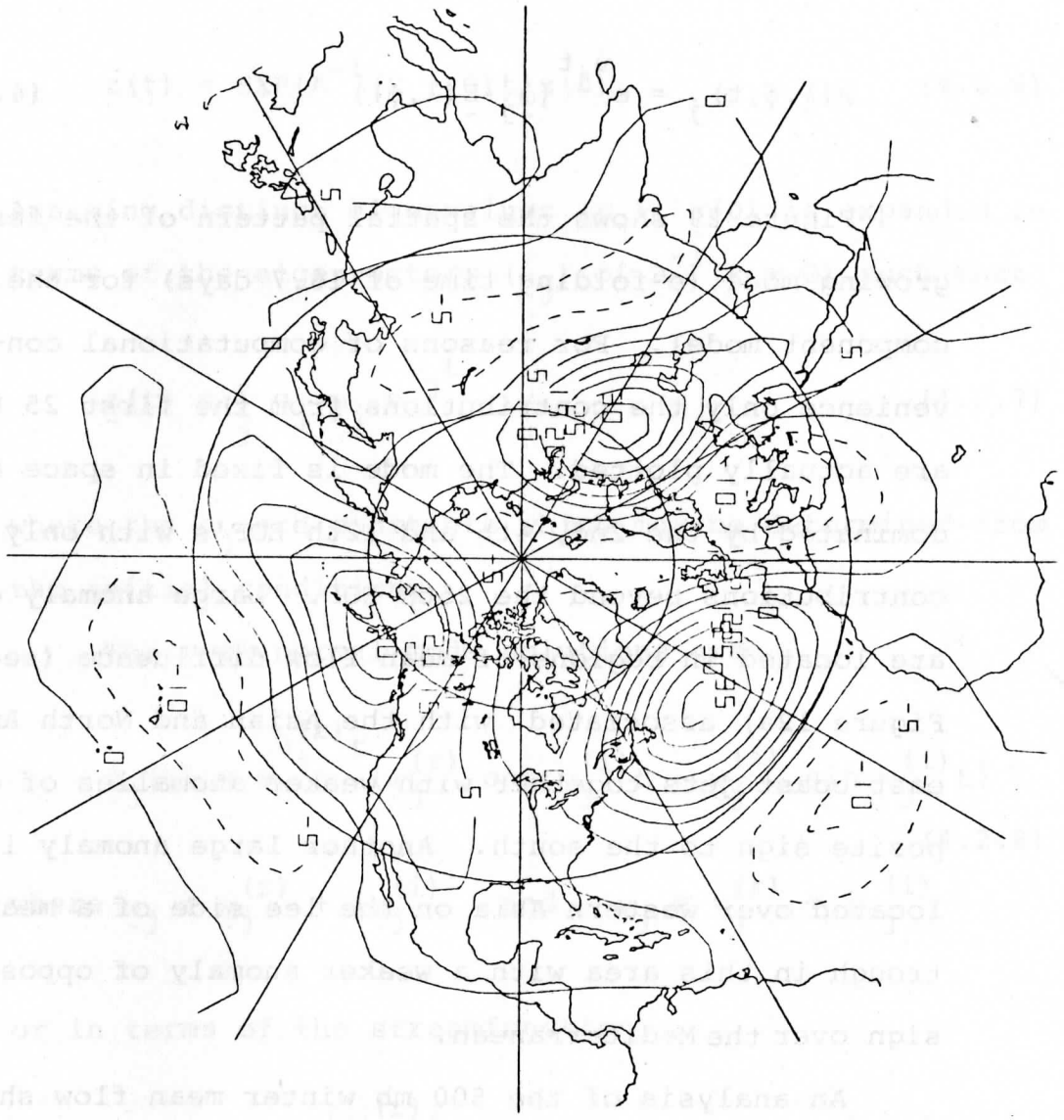

Figure 29. The spatial distribution of the fastest growing mode for the 40 component model linearized about the climatological mean winter flow. Units: non-dimensional, contour interval is 5×10^{-1}.

As a test of the sensitivity to the model truncation of the normal mode growth rates, periods and spatial structure, the solutions (4.2.8) were computed for all possible truncations up to and including 40. Figure 30 shows the growth rate and frequency of the fastest growing mode for each truncation. One finds a very strong sensitivity to the number of modes in the model. Beyond a truncation of 30 there is a general tendency towards very long or infinite periods; however, an obvious asymptotic behavior is not evident. A more detailed examination of the second, third and fourth fastest growing modes shows that at some truncations these modes have very nearly the same growth rates yet widely differing periods. When these become interchanged for subsequent truncations the large scatter evident in Figure 30 is produced. This, for example, is the case for the fastest growing mode at a truncation of 28 which is actually very similar to the second fastest growing mode at a truncation of 29. A somewhat stranger behavior occurs at more severe truncations, particularly at truncations between 9 and 14, where an apparently spurious unstable mode is traced until at a truncation of 15 it seems to have disappeared.

The fact that such apparently spurious unstable

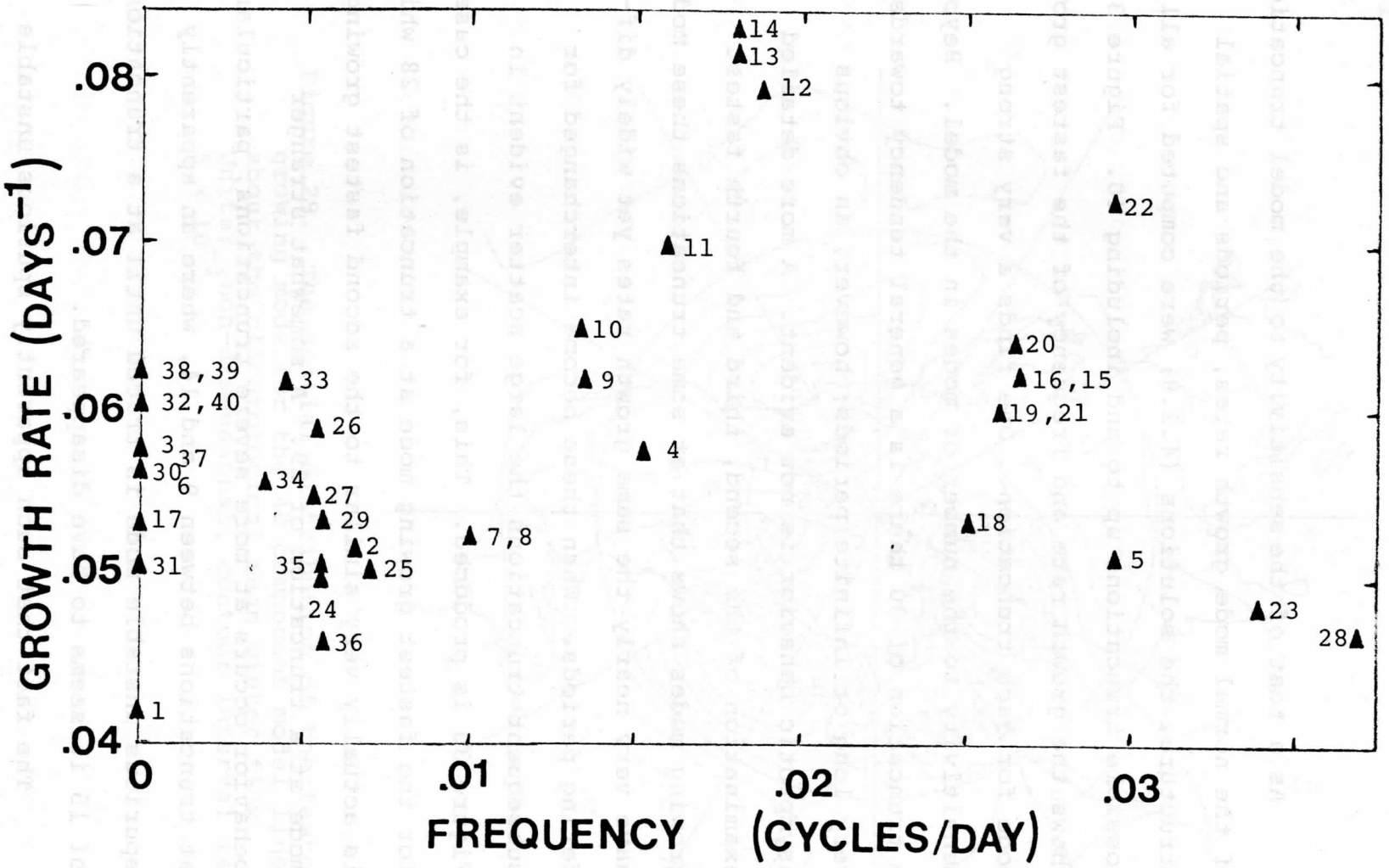

Figure 30. The growth rates and frequencies of the fastest growing mode as a function of model truncation. The numbers next to the triangles refer to the number of PC's retained in the model.

modes exist for intermediate model truncations points to a potentially serious defect of the truncated EOF model in particular, and of all truncated models in general. If this is indeed true, in general, then using highly truncated models for extended range forecasting has very little chance of success since the unstable spurious modes will eventually contaminate the forecast. Unfortunately, it seems that the EOF model may have an even greater sensitivity to truncation than the spectral or grid point models.

4.3. Forced nonlinear models and steady states

In this section the nonlinear aspects of the EOF model (3.2.3) are examined in more detail. For purposes of this analysis all boundary terms except friction are neglected.

With these simplifications (3.2.3) becomes

$$\sum_j a_{kj} \dot{z}_j = \sum_j \sum_i d_{kji} z_i z_j - \sum_j p_{kj} z_j + z_k^* \qquad (4.3.1)$$

where the linear part

$$p_{kj} = \kappa a_{kj} - r_{kj} - g_{kj} \qquad (4.3.2)$$

consists of the friction, mean flow/EOF interaction and the beta terms. It is emphasized that the model does not allow the anomalies to feed back on the mean flow. The mean flow is assumed to be continuously maintained by a climatological mean winter thermal and orographic forcing. The model should therefore be viewed as a quasi-nonlinear system where nonlinear interactions are only allowed between the EOF's which, in turn, may gain or lose energy due to the presence of the mean flow. As was shown in 3.2b these energy source/sink terms are the mean flow advection of the anomalous vorticity ($r2_{kj}$) and the inhomogeneous forcing (z_k^*).

a) EOF interactions and forcing

The extent to which EOF's interact is governed by the quadratic term in (4.3.1). The d_{kji} are coefficients involving linear combinations of the usual spectral interactions (see (3.2.4c)) and are referred to here as EOF interaction coefficients even though the tendency term in (4.3.1) is not strictly diagonal (diagonal elements are dominant). The interaction coefficients satisfy the properties that the sum of all permutations with respect to the indices i, j and k is identically zero, and that there is symmetry with respect

to i and j (see (3.2.4d,e)). It follows that a system with only one component is inert ($d_{kkk} = 0$).

An inspection of the EOF interaction coefficients should provide some insights into the nature of the nonlinear behavior of the EOF's; however, the large number of the coefficients makes this a rather tedious task. A somewhat more tractable approach is to examine the ensemble average nonlinear structure

$$\sum_i \sum_j \langle z_i z_j \rangle d_{kji} = \sum_j d_{kjj} \lambda_j \qquad (4.3.3)$$

where λ_j is the variance of the jth PC.

For each k and j, $d_{kjj} \lambda_j$ indicates the average effectiveness with which z_k and z_j interact to produce changes in z_k. The efficiency of the interaction, which depends on the spatial structure of the associated EOF's, is measured by d_{kjj}; while λ_j measures the intensity of the circulation fluctuations associated with z_j.

Table 2 shows the values of $d_{kjj} \lambda_j$ for some of the dominant interactions. Only those values are shown which are larger than an arbitrary cutoff of 10×10^{-6} in non-dimensional units. Examining this table row by row one finds that the 9th PC (k = 9) is most strongly influenced by interactions with other modes; particularly

Table 2. The time averaged EOF interactions ($d_{kjj}\ \lambda_j$). Values smaller than 10 are not shown. Units: non-dimensional $\times 10^{-6}$.

k \ j	1	2	3	4	5	6	7	8	9	10	11	12
1												
2												
3		14			12							
4		13	-18									
5	-12			10								
6		-13			12			13				
7			28					11				
8	-13											
9	32	64	25	13				11		12		
10	-12		-12	-16								
11		32										
12		15			-10							
13			15						12			
14	-10										10	
15									12			
16	-19		-11									
17												
18	-11		-27									
19												
20	13		12	20	11		10					
21												
22		16										
23												
24												
25								-11				

the first three. By far the dominant interaction is between the 2nd and 9th PC's. The effect of the interactions is to produce a positive tendency in the 9th PC which translates into a tendency for cyclonic flow over the North Atlantic (see Figure 9b). Thus the dominant nonlinear processes hinder the development of anticyclonic circulations in this region.

Other strong interactions occur between the 2nd and 11th, the 3rd and 7th, and the 3rd and 18th PC's. The fact that there are no entries in the first 2 rows of Table 2 indicates that the first two PC's do not interact very efficiently. These two modes do interact very efficiently with some of the higher order PC's (e.g. PC 9); however, the relatively low intensity (variance) of the higher order modes results in an overall small nonlinear contribution.

The ensemble average of (4.3.1) is

$$\sum_j d_{kjj} \lambda_j + z_k^* = 0 \qquad (4.3.4)$$

where, by definition, the forcing for the kth PC (z_k^*) balances the average anomaly interactions and is equal to the sum of the entries of the kth row in Table 2, with opposite sign. These are shown in Figure 31 for

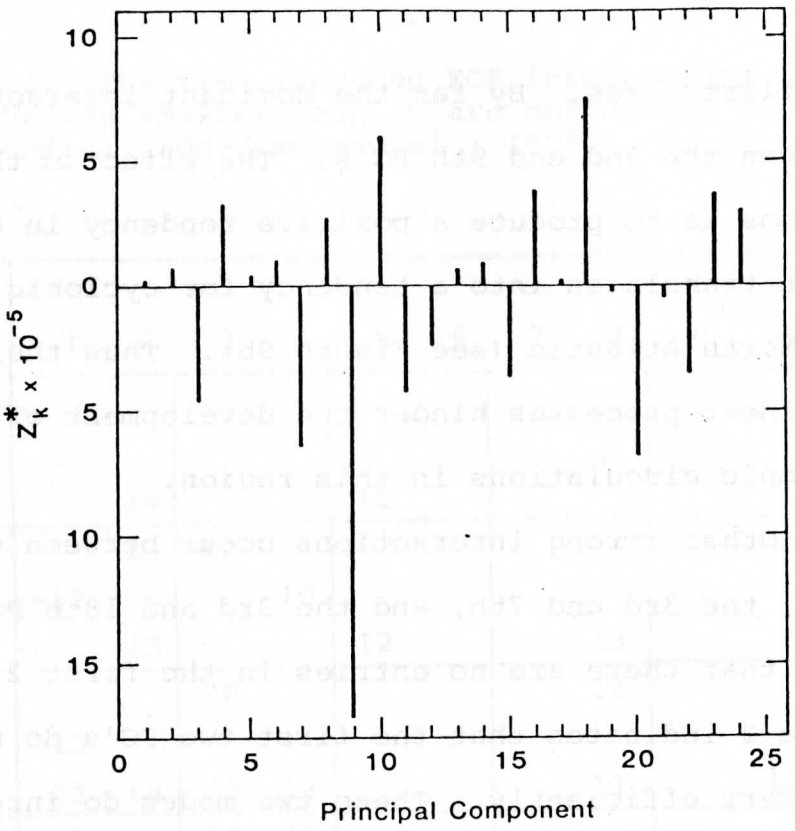

Figure 31. The inhomogeneous vorticity forcing (S) as a function of the PC's. Units: non-dimensional.

the first 25 PC's. The large negative value at the 9th PC corresponds to an important anticyclonic vorticity source in the North Atlantic. Other relatively large contributions to the forcing occur at the 7th, 10th, 18th and 20th PC's. The spatial distribution of the forcing (S) is shown in Figure 32. The dominance of the 9th EOF is clearly evident. This pattern is equal to the projection of the time averaged vorticity advection by the anomalies (c.f. Holopainen and Oort, 1981, Figure 2b)

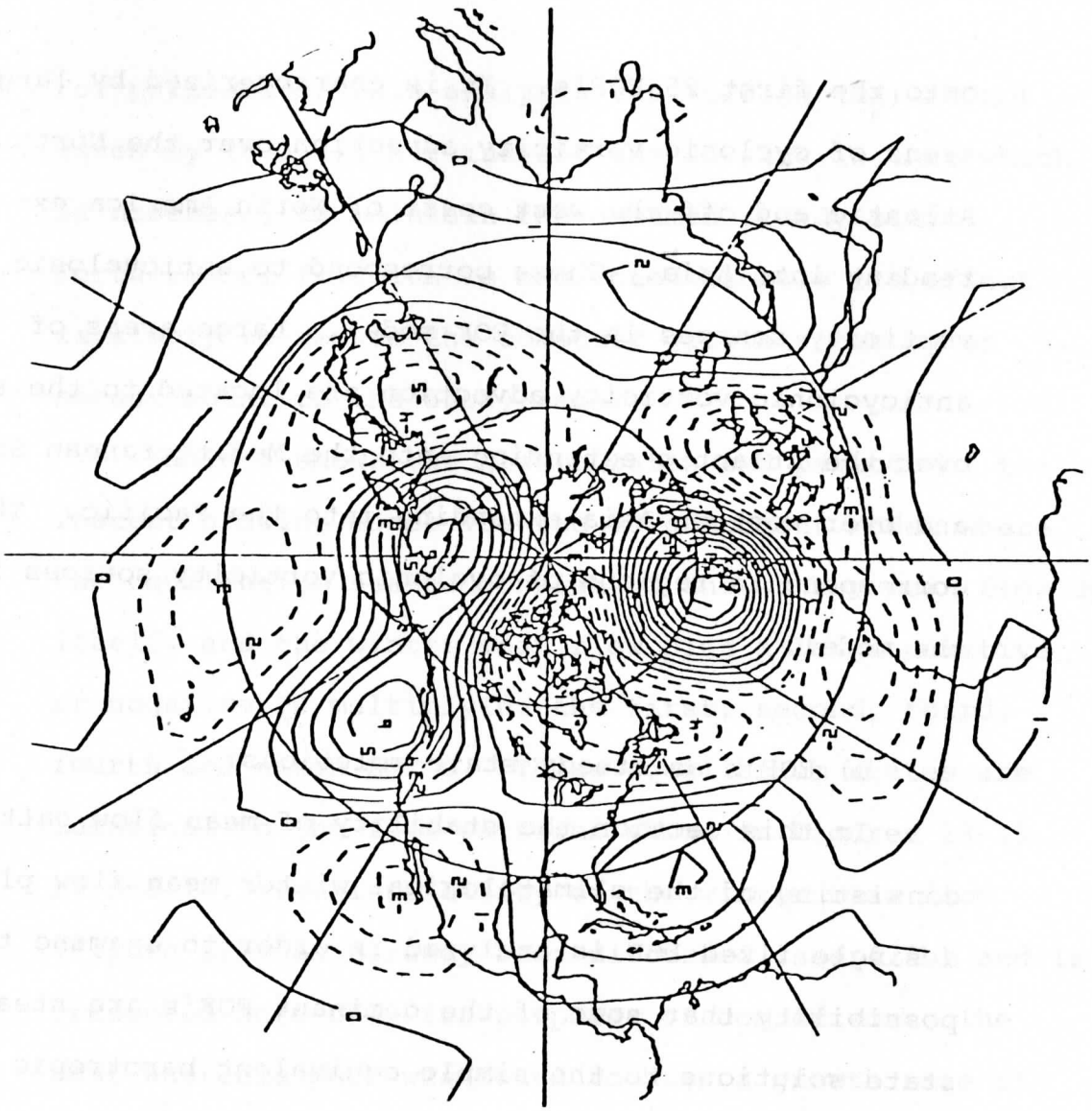

Figure 32. The spatial pattern of the inhomogeneous vorticity forcing (S). This pattern is equal to the mean anomaly vorticity advection projected onto the first 25 PC's. Units: non-dimensional, contour interval is 10^{-4}.

onto the first 25 EOF's. It is characterized by large areas of cyclonic vorticity advection over the North Atlantic and off the west coast of North America extending into Asia. These correspond to anticyclonic vorticity sources in the EOF model. Large areas of anticyclonic vorticity advection are located to the south over the Atlantic extending into the Mediterranean Sea and over western Asia extending into the Pacific. These correspond to regions of cyclonic vorticity sources in the model.

b) EOF's as steady state solutions

In this section the stability of mean flow patterns consisting of the climatological winter mean flow plus a single fixed EOF is analyzed in order to examine the possibility that some of the dominant EOF's are steady state solutions to the simple equivalent barotropic model (4.3.1).

The equations governing small perturbations about a base state ($\tilde{z}^e$) are

$$\sum_j a_{kj}(z_j - z_j^e) = \sum_j \{-p_{kj} + 2 \sum_i d_{kji} z_i^e\}(z_j - z_j^e) \qquad (4.3.5)$$

For purposes of this analysis the forcing (z_k^*) is not given by (4.3.4), but instead the forcing is that which is necessary to maintain the assumed steady state. Furthermore, friction is neglected because its effect is simply to reduce the computed growth rates by an amount equal to the decay rate.

Table 3 shows the growth rates and periods of the fastest growing modes for the 40 component model where the equilibrium states consist of the winter mean flow by itself, and the winter mean flow plus a large positive or negative PC multiplying the first, second, third, fourth and ninth EOF's. These equilibrium states are identical to the flow patterns shown in Figures 13-15, 17 and 18. The instability of the winter mean flow (Figure 12) has already been discussed (see 4.2b) and is presented here only for purposes of comparison. The most unstable mode was found to have a growth rate of 16.7 days with an infinite period.

With a positive first EOF (Figure 13a) the flow is somewhat more unstable and again is fixed in space. The flow is even more unstable when it involves a negative first EOF (Figure 13b) with the fastest growing mode exhibiting a 10.4 day e-folding time and a period of 51.8 days. The second EOF equilibrium states exhibit

Table 3. Characteristics of the fastest growing mode in a 40 component model with base states consisting of the climatological winter mean flow plus large positive or negative instances of some of the dominant EOF's.

Equilibrium state	e-folding time (days)	Period (days)
mean flow	16.7	∞
+/- EOF 1	13.2/10.4	∞/ 51.8
+/- EOF 2	9.9/ 6.7	25.4/185.2
+/- EOF 3	13.7/ 7.0	40.0/∞
+/- EOF 4	9.5/10.8	27.8/∞
+/- EOF 9	11.7/ 5.6	19.5/∞

modes with e-folding times under 10 days. The negative instance (Figure 14b) has the most unstable mode with a 6.7 day e-folding time and a very long period. The third EOF is also very unstable for the negative instance (e-folding time of 7 days, infinite period) which is shown in Figure 15b; whereas the positive version (Figure 15a) is only slightly more unstable than the winter mean flow alone. The fourth EOF (Figure 18) exhibits modes with e-folding times of about 10 days for both the positive and negative instances. The ninth EOF (Figure 17) is very unstable for the negative

instance exhibiting a mode with an e-folding time of 5.6 days and infinite period.

Whether any of these equilibrium states are stable depends of course on the value of the frictional decay rate. However, these results do suggest that it is unlikely that the negative instances of the second, third and ninth EOF's may be maintained as stable steady states of an equivalent barotropic model of the type discussed here. In particular, the North Atlantic blocking mode (negative instance of the ninth EOF), which previous studies have suggested may be a stable equilibrium state, turns out to be the most unstable of all the regimes investigated.

c) Low order models

In the following analysis the solutions to (4.3.1) are examined in more detail for the case where z_k^* is determined from the observations (4.3.4) and only a relatively small number of modes are allowed into the model.

i) Method of solution

The general problem of finding all steady solutions to (4.3.1) for an arbitrary truncation is a very

difficult if not impossible task. The approach taken in this section is to develop a numerical method which will find all steady state solutions for models having a reasonably small number of degrees of freedom and certain restrictions on the model parameters.

The model is extended to allow for a change in the magnitude of the forcing by including an additional parameter (α) such that

$$\sum_j a_{kj} \dot{z}_j = \sum_j \sum_i d_{kji} z_i z_j - \sum_j p_{kj} z_j + \alpha z_k^* \quad (4.3.5)$$

The solution method involves searching a subset of the phase space defined by the PC's to find regions where the tendency (LHS of (4.3.5)) is small. These regions define a set of points which are used as initial guesses for the multivariate version of Newton's method which, in turn, is used to determine the final solutions.

The tendency is written in terms of the MSV as

$$\frac{1}{2}\frac{d}{dt}(\text{MSV}) = \sum_k \sum_j a_{kj} \dot{z}_k z_j = -\sum_k \sum_j p_{kj} z_j z_k + \alpha \sum_k z_k z_k^* \quad (4.3.6)$$

or, in vector and matrix notation

$$\frac{1}{2}\frac{d}{dt}(\text{MSV}) = -\underset{\sim}{z}^T P_s \underset{\sim}{z} + \alpha \underset{\sim}{z}^T \underset{\sim}{z}^* \tag{4.3.7}$$

where P is the matrix of coefficients p_{kj} (see (4.3.2)) and

$$P_s = \frac{1}{2}(P + P^T) \tag{4.3.8}$$

is a symmetric matrix composed of P and its transpose.

Setting the MSV tendency equal to zero and assuming P_s is nonsingular, (4.3.7) may be written as

$$(\underset{\sim}{z} - \underset{\sim}{q})^T P_s (\underset{\sim}{z} - \underset{\sim}{q}) = \underset{\sim}{q}^T P_s \underset{\sim}{q} \tag{4.3.9}$$

where

$$\underset{\sim}{q} = \frac{\alpha}{2} P_s^{-1} \underset{\sim}{z}^* \tag{4.3.10}$$

If P_s is positive definite (4.3.9) describes an ellipsoid of zero KE tendency centered at $\underset{\sim}{q}$ inside of which the KE tendency is positive and outside of which the tendency is negative. Systems for which P_s is positive definite will be denoted as bounded systems, since this implies the existence of an ellipsoid of constant KE inside of which all trajectories are eventually trapped

(see Lorenz, 1980). When this ellipsoid is contained within a sufficiently small volume of the phase space a numerical search for all the steady states of the system is feasible for low order models. The procedure for the search is described in Appendix D.

The volume and orientation of the ellipsoid (4.3.9) depends on the eigenvalues (μ_i) and eigenvectors ($\underset{\sim}{t}_i$) of the symmetric matrix .

$$P_s = \kappa A - R_s \tag{4.3.11a}$$

which has elements

$$p^s_{kj} = \kappa a_{kj} - \frac{1}{2}(r_{kj} + r_{jk}) \tag{4.3.11b}$$

This is seen more clearly when the ellipsoid is rotated to the standard form

$$\frac{y_1^2}{b_1^2} + \frac{y_2^2}{b_1^2} + \ldots + \frac{y_N^2}{b_N^2} = 1 \tag{4.3.12}$$

The volume is related to the length of the semi-axes

$$b_i = \frac{\alpha}{2} \left(z^{*T} P_s^{-1} z^* / \mu_i\right)^{\frac{1}{2}} \tag{4.3.13a}$$

and the coordinate rotation is given by

$$\underset{\sim}{z} - \underset{\sim}{q} = T\underset{\sim}{y} \qquad (4.3.13b)$$

where T is the matrix of eigenvectors $(\underset{\sim}{t}_i)$.

In order to insure that P_s is positive definite κ must be larger than the largest eigenvalue of the generalized eigenvalue problem

$$\det(R_s - \lambda_i^* A) = 0 \qquad (4.3.14)$$

As κ is reduced so that it approaches the largest eigenvalue of (4.3.14), the ellipsoid (4.3.9) becomes infinitely large since the smallest eigenvalue of P_s approaches zero. The direction and length of the associated axis (4.3.13a) determines to some extent the nature of possible large amplitude steady state solutions.

In order to insure a reasonable bound for the system the value of $\kappa \equiv \kappa_r$ is chosen such that the volume of the ellipsoid of zero KE tendency (4.3.9) is equal to one half the volume of the ellipsoid

$$\sum_k \sum_j a_{kj}\, z_k\, z_j = \sum_k a_{kk}\, \lambda_k \qquad (4.3.15)$$

where the RHS is the time averaged anomaly MSV of the observations. Such a constraint is relatively easy to apply for an arbitrary truncation and will be used for most of the equilibrium calculations to follow. See Appendix D for details on the development of these constraints.

ii) Characteristics of the solutions

Before applying the general numerical approach outlined in the previous section, the two component model will be analyzed more completely by directly solving (4.3.5) for the equilibrium states

$$\underset{\sim}{z}^e = \begin{pmatrix} z_k^e \\ z_j^e \end{pmatrix} \equiv \begin{pmatrix} x \\ y \end{pmatrix} \tag{4.3.16}$$

The equations are

$$0 = 2d_{kkj}\, xy - 2d_{jjk}(y^2 - \alpha\lambda_j) - p_{kk}\, x - p_{kj}\, y \tag{4.3.17a}$$

$$0 = 2d_{jjk}\, xy - 2d_{kkj}(x^2 - \alpha\lambda_k) - p_{jk}\, x - p_{jj}\, y \tag{4.3.17b}$$

or

$$0 = y^3 + a_2y^2 + a_1y + a_0 \qquad (4.3.18)$$

where $a_2 = \delta_2/\delta_1$, $a_1 = \delta_3/\delta_1$, $a_0 = \delta_4/\delta_1$ and

$$\delta_1 = -4d_1d_2(p_{12} + p_{21}) + (d_2^2p_1 + d_1^2p_2) \qquad (4.3.19a)$$

$$\delta_2 = 8\alpha d_1d_2^2\lambda_2 + 2p_1d_2(p_{21} - p_{12}) - 2d_1p_{12}(p_{12} + p_{21}) + 4d_1p_1p_2 + 8\alpha d_1^3\lambda_1 \qquad (4.3.19b)$$

$$\delta_3 = 4\alpha d_1d_2\lambda_2(2p_{12} + p_{21}) + p_1(p_{12}p_{21} - p_1p_2) + 4\alpha p_1(d_2^2\lambda_2 - 2d_1^2\lambda_1) \qquad (4.3.19c)$$

$$\delta_4 = -2\alpha d_2\lambda_2(4\alpha d_1d_2\lambda_2 + p_1p_{21}) + 2\alpha d_1p_1^2\lambda_1 \qquad (4.3.19d)$$

with $d_1 = d_{kkj}$, $d_2 = d_{jjk}$, $p_1 = p_{kk}$, $p_2 = p_{jj}$,

$p_{12} = p_{kj}$ and $p_{21} = p_{jk}$.

The first component is computed from

$$x = (2d_2y^2 + p_{12}y - 2\alpha d_2\lambda_2)/(2d_1y - p_1) \qquad (4.3.20)$$

The number of steady states is determined from

$$\frac{b^2}{4} + \frac{c^3}{27} \begin{cases} > 0 & \text{1 real, 2 complex conjugate roots} \\ = 0 & \text{3 real, at least 2 are equal} \\ < 0 & \text{3 distinct real roots} \end{cases} \tag{4.3.21}$$

where

$$c = \frac{1}{3}(3a_1 - a_2^2) \tag{4.3.22a}$$

$$b = \frac{1}{27}(2a_2^3 - 9a_2a_1 + 27a_0) \tag{4.3.22b}$$

and the a_i are those in (4.3.18).

Figure 33 shows the number of real solutions for various values of α and κ for the two component models

$$\begin{pmatrix} z_1 \\ z_2 \end{pmatrix} \text{ and } \begin{pmatrix} z_1 \\ z_9 \end{pmatrix}.$$

The former model is chosen because it contains the two modes which contribute most to the observed variance and the latter is of interest because of the highly non-linear nature of the ninth PC (see 4.3a). The heavy

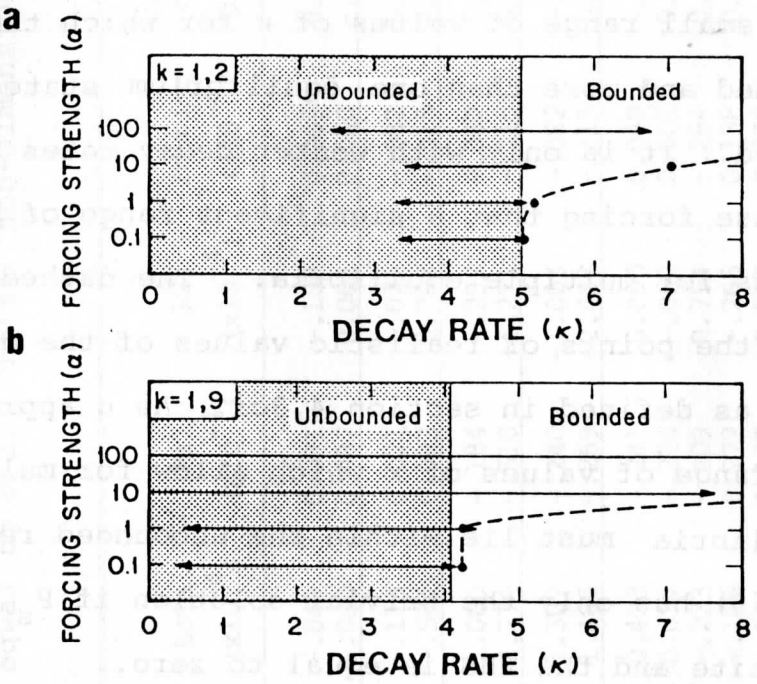

Figure 33. The number of steady states as a function of model parameters for the two component models consisting of (a) the first and second PC's and (b) the first and ninth PC's. The heavy horizontal arrows indicate the range of frictional decay rates which allow 3 steady states. Outside of this range only 1 steady state is possible. The speckled region indicates that the trajectories are not bounded and the dashed line connects points having observationally consistent decay rates (see text for details). Units for κ: non-dimensional $\times 10^{-3}$. Multiply by 12.57 to get units of days^{-1}.

arrows indicate the range of κ for which 3 solutions are found. The speckled region indicates the range of κ for which the system is unbounded (i.e. P_s in (4.3.9) is not positive definite). One finds that for reasonable values of the forcing strength ($\alpha \doteq 1$) there is only a

very small range of values of κ for which the system is bounded and more than one equilibrium state is obtained. It is only with weaker decay rates and/or very intense forcing that a significant range of parameters allows for multiple equilibria. The dashed lines connect the points of realistic values of the decay rate (κ_r) as defined in section 4.3ci. As α approaches zero the range of values of κ which allow for multiple equilibria must lie within the unbounded region since (4.3.9) has only the trivial solution if P_s is positive definite and the RHS is equal to zero.

Next the numerical searching technique outlined in the previous section is used to obtain the equilibrium solutions for various low order models with up to 5 PC's. Table 4 lists the steady state solutions for selected models having parameter values α equal to one and the frictional decay rate equal to κ_r (see 4.3ci). For each solution the balance of terms is shown and the solution to the corresponding linear system is given.

With only the first two PC's in the model only one solution is obtained and it is stable. This is of course consistent with Figure 33a which shows that for these parameter values only one real solution is possible. The balance of terms shows that the nonlinear contribution

Table 4. Steady state solutions and balance of terms for various model truncations. The corresponding solution for the linear system is given in parentheses. The frictional decay rate (κ_r) is chosen to be observationally consistent (see text) and the forcing strength (α) is equal to one. Units: non-dimensional.

k	κ_r	Solution ($\times 10^{-4}$)	(linear)	Stable	Non linear ($\times 10^{-4}$)	Beta ($\times 10^{-4}$)	R1 ($\times 10^{-4}$)	R2 ($\times 10^{-4}$)	Forcing ($\times 10^{-4}$)	Frictional decay ($\times 10^{-4}$)
1	0.0051	-.384	(-.388)	Yes	-.0006	-.049	0.071	-.109	0.009	0.078
2		0.311	(0.319)		-.0007	-.060	0.087	0.001	0.060	-.088
1	0.0042	-.361	(-1.592)	Yes	0.011	-.113	0.021	-.021	-.082	0.185
9		0.306	(0.346)		0.047	-.504	0.093	0.763	-.315	-.084
1	0.0042	7.492		Yes	0.582	1.000	-.184	-.292	-.082	-1.025
9		-2.700			1.616	2.774	-.510	-4.271	-.315	0.705
1	0.0042	3.959		No	0.577	1.307	-.240	-1.003	-.082	-.559
9		-3.529			0.647	1.466	-.269	-2.403	-.315	0.875
1	0.0062	1.566	(1.836)	Yes	-.014	0.433	-.241	0.095	0.049	-.322
2		-.618	(-.581)		-.023	0.054	-.274	-.052	0.001	0.286
3		-.373	(-.455)		0.034	-.223	-.409	0.754	-.264	0.109
4		-.324	(-.394)		-.035	-.166	0.272	-.265	0.138	0.056
5		0.861	(1.077)		0.010	-.909	0.167	0.917	0.039	-.223
1	0.0059	1.334	(-1.356)	Yes	-.001	0.929	-1.322	1.003	-.086	-.523
2		-4.169	(-2.962)		-.495	-.512	-.572	0.325	0.161	1.094
3		-.206	(0.578)		0.111	2.690	-1.533	-1.196	-.216	0.145
4		1.046	(-2.275)		0.271	2.296	0.257	-2.789	0.048	-.082
9		-1.578	(-2.887)		1.471	3.309	0.764	-4.673	-1.335	0.465

is very small and the solution is very near to the small amplitude solution to the linear system. Figure 34a shows the steady solution as a point on the ellipse of zero KE tendency (A), along with the ellipse of constant MSV (B) given by (4.3.15), superimposed on the streamlines of the PC tendencies. Within A the system is gaining energy; i.e., the PC tendency is such that the trajectories cross the ellipses of constant KE (such as B) moving towards higher energy. From Figure 34a it is evident that any solution to this two component system will follow a spiral trajectory, momentarily gaining a small amount of energy with each pass through A and eventually coming to rest at the equilibrium point near the origin.

For the two component system involving PC's one and nine, Table 4 shows that three solutions were found. This confirms the results of Figure 33b which indicates the existence of three real solutions at the point where the dashed line intersects the heavy arrow corresponding to $\alpha = 1$. Two are stable and one is unstable. One of the stable solutions is again near the solution to the corresponding linear system and the contribution from the nonlinear terms is relatively unimportant. The other stable solution has much larger magnitudes for the PC's

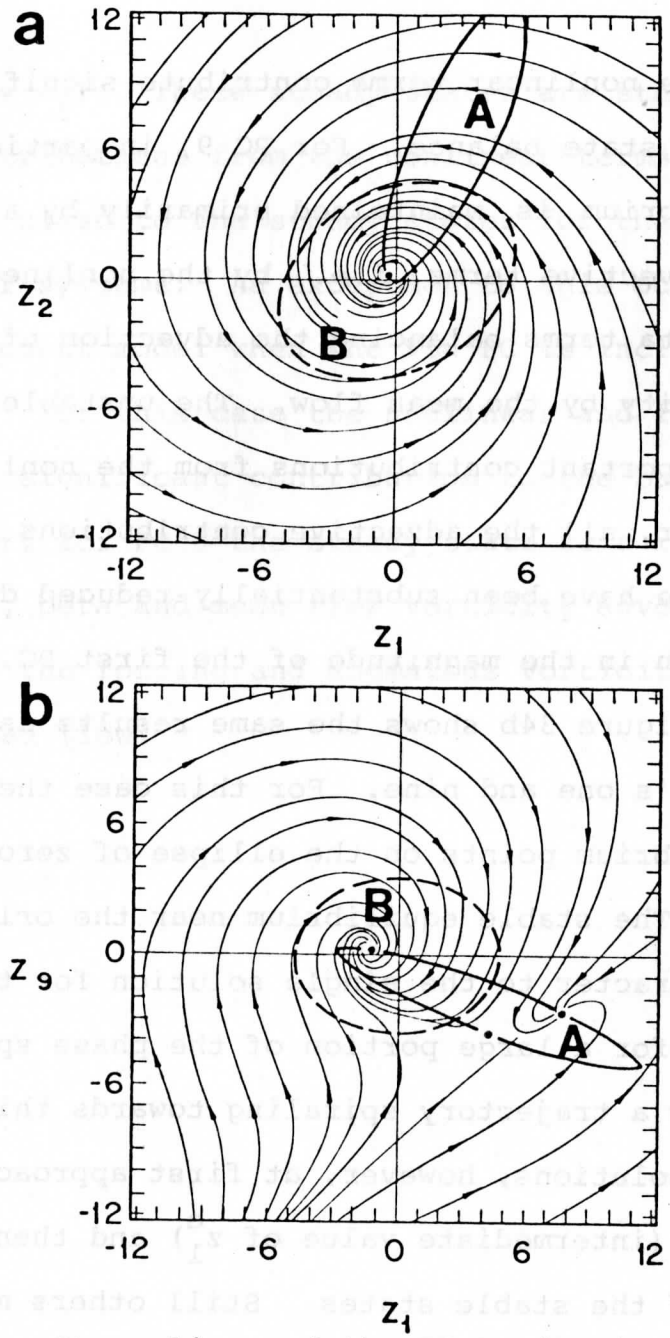

Figure 34. Streamlines of the PC tendencies with the superimposed ellipses of zero MSV tendency (A) and constant MSV of the observations (B) for the two component models consisting of (a) the first and second PC's and (b) the first and ninth PC's. Parameter values are those given in Fig. 33 for the case where the dashed line intersects $\alpha = 1$. Units: non-dimensional $\times 10^{-4}$.

and the nonlinear terms contribute significantly to the steady state balance. For PC 9, in particular, the equilibrium is maintained primarily by a balance between the advective terms, i.e., by the nonlinear interaction and beta terms balancing the advection of anomalous vorticity by the mean flow. The unstable solution also has important contributions from the nonlinear term. However, all the advective contributions to the ninth PC balance have been substantially reduced due to the reduction in the magnitude of the first PC.

Figure 34b shows the same results as 34a except now for PC's one and nine. For this case there are three equilibrium points on the ellipse of zero KE tendency (A). The stable equilibrium near the origin is similar in character to the single solution for the first two PC's; for a large portion of the phase space solutions follow a trajectory spiraling towards this steady state. Some solutions, however, at first approach the unstable state (intermediate value of z_1^e) and then move towards one of the stable states. Still others move directly towards the large magnitude stable state (largest value of z_1^e).

As more PC's are allowed into the model only one equilibrium solution is found for each truncation (with

$\alpha = 1$, $\kappa = \kappa_r$). These steady states are stable with small contributions from the nonlinear terms, and are generally close to the steady states for the corresponding linear systems. An exception to this occurs for the five component model when the 9th PC is included (see Table 4). For this case the nonlinear and forcing terms provide a significant contribution to the balance. In particular, for PC 9 the steady state is a result of the nonlinear, beta and mean flow vorticity advection terms balancing the forcing and anomalous vorticity advection by the mean flow.

5. SUMMARY AND CONCLUSIONS

The observed wintertime intraseasonal variability of the Northern Hemisphere circulation has been analyzed using a combination of statistical and dynamical methods. The basic approach has involved a somewhat reversed analysis method, in which statistical and empirical methods are first used to identify and quantify the important modes of variability. Subsequently these modes are entered into a simplified dynamical model in an attempt to gain further insight into the important processes governing their behavior. The primary advantage gained by such an approach is the ability to monitor explicitly the behavior of realistic modes of variability within a dynamical setting. The main disadvantages concern the difficulties associated with the proper identification of the "true" modes of variation (the EOF's) and an apparently strong sensitivity to model truncation. These drawbacks are connected with the more general problem which involves an incompatibility between the model dynamics and the degrees of freedom allowed in the model. While this incompatibility occurs for most highly truncated models, it seems to be more apparent for the EOF model in which the individual modes (1) are constrainted to a flip-flop type of behavior, (2) involve

linear combinations of spectral modes which are constrained to behave in unison, and (3) are (in the present case) based on 10-day averaged data. The latter effectively filters out those modes associated with day to day weather fluctuations.

In order to emphasize the statistical nature, as well as enhance the physical interpretation of the EOF's, the analysis is based on deviations from the climatological mean seasonal cycle and is limited to the winter season. Guided by the results of a statistical test which compares the variance of the PC's to white noise (Preisendorfer et al., 1981), only the first 12 EOF's are analyzed in detail. The EOF's are based on a spherical harmonic expansion of the streamfunction data which allows for a convenient spectral decomposition of their spatial structure.

The dominant EOF's are predominantly associated with zonal wave numbers 0 through 5, and range anywhere from very localized anomalies to more wavelike structures to very complicated spatial patterns. While there is a general shift toward smaller scales as one goes to yet higher order EOF's, this trend is very weak and seems to be associated with a general flattening of the spectrum toward a white noise structure. These results suggest

a weakness in the EOF representation of an independent data set. Beyond the large scale features captured by the dominant EOF's a very large number of the spatially noisy higher order EOF's would be needed to represent adequately the complete spectrum of spatial scales.

Some of the dominant EOF's were found to be associated with the more familiar observed modes of variability. In particular, the first three EOF's seem to exhibit a range of behavior encompassing an index cycle, the Pacific/North American pattern and the North Atlantic oscillation. The fourth and ninth EOF's were found to be related to some aspects of North Pacific and North Atlantic blocking, respectively. The negative version of the ninth EOF, when superimposed on the mean flow bears a striking resemblance to the classical North Atlantic block.

Comparisons with other studies and approximate standard errors for the PC variances suggest a large amount of intersample variability in the EOF patterns. However, an index cycle-type mode was found in all the studies compared, usually in association with the first EOF, or the second EOF when the seasonal cycle is not removed. In the latter case the first EOF describes the seasonal cycle. Similarities were found in some cases

with higher order EOF's; most surprising is the reproducibility of the ninth (North Atlantic blocking) EOF.

The dynamical basis for this study centers on an equivalent barotropic model which includes the effects of surface friction, orography and surface pressure tendencies (long wave correction term). In addition, planetary vorticity advection by the divergent wind is included, leading to a generalized form of the orography and longwave correction terms. The seasonal cycle enters into the anomaly equations via the advective terms and as an inhomogeneous forcing due to the fact that the mean flow does not, by itself, satisfy the vorticity equation. The inhomogeneous forcing is not a function of time due to the stationarity assumption and the seasonal cycle is replaced by a constant equal to the climatological mean winter value. The complete EOF model consists of 40 quadratically nonlinear equations for the PC tendencies. The restriction to 40 PC's (out of a possible 119) is primarily a consequence of the excessive computational requirements for the nonlinear terms.

By formulating the model as a linear multiple regression problem in which the predictors involve only the parameterized terms, it was found that the boundary terms contribute very little to the remaining variance.

These results are very likely explained to some extent by the crudeness of the parameterizations and the inadequacies of the barotropic model. For the case of the orography these results may also suggest the unimportance of direct orographic effects on the anomalies at the 500 mb level relative to the effects of the advection of mean flow vorticity. The latter term is similar in form to the orography term where the mean flow vorticity acts as a "dynamic orography". With such an interpretation, major "mountain chains" are located along the east coasts of North America and Asia, and extensive "valleys" are found throughout the subtropics. The relative unimportance of the orographic term and particularly the friction term is a result which is qualitatively similar to the results obtained in the Kruse (1983) statistical study of an equivalent barotropic model. However, detailed comparisons are difficult, due to the fact that the present model is based on deviations from a base state.

Peculiarities of the truncated EOF model include the inability of the model to conserve both energy and enstrophy simultaneously, and the results (from the regression) indicating that the longwave correction is not needed. The latter is contrary to the results of

the Kruse (loc. cit.) study and seems to be a filtering effect of the EOF expansion. The effective total wave numbers of the first 40 PC's lie in the range of 7 to 12; whereas, the retrograde characteristics of the non-divergent barotropic model are primarily associated with waves having total wave numbers less than 6.

The mean flow/anomaly interaction and beta terms are by far the dominant components of the EOF model. However, the strong negative correlation exhibited by these two terms results in a much reduced combined variance, comparable to that of the tendency and anomaly advection terms. Signficiantly smaller variance is associated with the orography and friction terms. As a simple measure of the EOF model's predictive skill, correlations between the observed tendency and the tendency calculated from the RHS terms of the model were computed. For the 40 component model the dominant PC correlations ranged from greater than 0.55 for the fifth and ninth PC's to less than 0.4 for the sixth, eighth and eleventh PC's. Future work suggested by these results involves a more detailed investigation of the synoptic situations and associated PC compositions which lead to particularly good or bad forecasts.

Results of a 365 day winter simulation starting from

mean flow initial conditions identified the mean flow advection of anomalous vorticity as an important energy source and emphasized the need for a more detailed inspection of the stability properties of the climatological mean flow. A major result of this study is the identification of the zonally varying wintertime mean flow as a potentially important energy source for some of the dominant wintertime EOF's. A perturbation analysis of the climatological mean winter flow consisting of individual EOF patterns showed that when friction is neglected the largest potential growth rates (e-folding times of about 16 days) occurred for the second and third PC's with generally weak or negative growth rates beyond the thirteenth PC. For the case of the January 1-10 mean flow the third and twelfth PC's show a dramatic increase in growth rates (9.9 and 13 day e-folding times, respectively). This is consistent with and supports the recent findings of Simmons et al. (1982) concerning the barotropic instability of the 300 mb climatological mean January flow. They suggested that barotropic instability is a major source of the low frequency variability of the wintertime Northern Hemisphere circulation.

A peak blocking month (May) was also analyzed in order to investigate the possibility that the springtime

climatological mean flow might show a preference for growing perturbations consisting of the blocking EOF's. Results of this analysis showed a dramatic drop in the growth rates for almost all the PC's for the May average flow. In particular, the fourth (North Pacific blocking) and the ninth (North Atlantic blocking) PC's exhibited essentially zero growth rates. Part of the reason for the overall drop in growth rates is very likely the general decrease in the intensity of the mean springtime circulation; however, it may also be due in part to an incompatibility between the wintertime perturbation patterns (EOF's) and the springtime base state.

A more complete normal mode analysis with the 40 component model showed that for the climatological mean winter flow the fastest growing mode (e-folding time of 16.7 days) is fixed in space and is dominated by the second, fourth and twelfth EOF's. However, a sensitivity test revealed a very strong dependence of the growth rates and particularly the periods of the fastest growing modes on the level of EOF truncation. This is partly a result of an interchange of modes occurring for successive truncations when no one dominantly unstable mode exists. However, other apparently spurious unstable modes which occur for intermediate truncations suggest

a more serious truncation problem.

The nonlinear aspects of the model have been examined when all the boundary terms except the dissipation are neglected. An inspection of the time averaged EOF interactions shows that the ninth PC is most strongly influenced by interactions with other modes. By far the dominant interaction occurs between the second (associated with fluctuations in the North Atlantic jet) and the ninth (North Atlantic blocking) PC's. The inhomogeneous forcing is found to be dominated by the ninth PC; this implies the existence of an important anticyclonic vorticity source in the North Atlantic.

Flow regimes consisting of the climatological winter mean flow and a single dominant EOF have been tested for their stability in order to examine the possibility that such patterns exist as steady state solutions to simple forced barotropic models. For this analysis the inhomogeneous forcing is chosen to be that which is necessary to maintain the constructed base state. All 40 PC's are allowed into the perturbation equations. Each of the base states examined were found to be more unstable than the mean flow by itself. In particular, the base states involving the negative instances of the second, third and ninth EOF's were found to be very

unstable with the fastest growing modes having e-folding times of less than seven days. The North Atlantic blocking mode (negative ninth EOF) is the most unstable, indicating a very strong nonlinear transfer of energy out of this mode. These results seem to contradict the soliton theory of blocking (e.g. McWilliams, 1980) in which the nonlinearities are responsibe for maintaining the mode against the effects of dispersion.

Simple low-order nonlinear models were investigated in more detail to examine the possibility of multiple equilibria. In order to find all the equilibria for the low order models a numerical method was developed which searches the ellipsoid of zero kinetic energy tendency. The success of this method hinges on the need to restrict the search to a reasonably small region of phase space. Therefore, for each model truncation (except for the two-component models) a single value of the decay rate was chosen such that the PC trajectories are eventually trapped in a phase space volume consistent with the observed mean kinetic energy of the anomalies.

For the two-component models the solutions were computed directly from a third order polynomial, as well as by the searching method, in order to verify the technique. Multiple equilibria were found; however, in

general these solutions involved unrealistically low values of the decay rate and/or unrealistically large values of the inhomogeneous forcing. For the model consisting of the first and ninth PC's, three solutions were found for realistic parameter values. Two of the solutions are stable and one is unstable. One of the stable solutions is near the solution to the corresponding linear system, while the other two have large magnitudes with important contributions to the steady state balance from the nonlinear terms. As more components were allowed into the model only one solution was found for realistic parameter values. This solution is stable and generally very near to the linear solution with only small contributions from the nonlinear terms.

These results do not support the near resonance multiple equilibria mechanism of the low order barotropic models with orography and thermal driving. To the extent that the atmosphere is equivalent barotropic, the present study suggests that the 500 mb streamfunction anomalies do not significantly "feel" the direct effects of the orography. Instead the presence of the mean flow plays a dominant role as an orographic type term as well as an important energy source for the anomalies. While multiple equilibria are found for some values of the

model parameters, the exact mechanism is not clear. For realistic values of the decay rate large amplitude equilibria are associated with directions in the PC phase space given by the most unstable eigenvector of the energy related terms (mean flow advection of the anomalous vorticity and dissipation). In addition, these results emphasize the need for an inhomogeneous forcing in order for multiple equilibria to occur in the presence of realistic damping.

In the present model the residual inhomogeneous forcing exhibits important anticyclonic vorticity sources in the North Atlantic and off the west coast of North America. Therefore, blocking-type flows are most likely to occur as a quasi-linear response to the direct forcing in these areas. In order to determine the nature of this forcing it is likely that one must turn to more complicated multi-level models which directly include the effects of baroclinicity and thermal forcing. Frederiksen (1982) has examined the stability of a 3-dimensional flow typical of the Northern Hemisphere winter. It was found that for certain values of the static stability the fastest growing modes in a two-layer spherical quasigeostrophic model exhibited high-low dipole structures in both the Pacific and Atlantic oceans. Such an

instability which depends on the vertical structure of the atmosphere would show up as a residual forcing in the present barotropic model.

APPENDIX

A. COMPUTATIONS

1. Real and complex expansions

The complex expansion of the streamfunction in terms of odd spherical harmonics (Y_n^m) is

$$\psi(\lambda,\phi,t) = \sum_{n_\alpha=1}^{16} \sum_{m_\alpha=-n_\alpha}^{n_\alpha} \psi_{n_\alpha}^{m_\alpha}(t) e^{im_\alpha\lambda} P_{n_\alpha}^{m_\alpha}(\phi)$$

$$(n_\alpha - m_\alpha \text{ odd})$$

$$\equiv \sum_{\alpha} \psi_\alpha(t)\, Y_\alpha(\lambda,\phi) \qquad \text{(A.1)}$$

$$(n_\alpha - m_\alpha \text{ odd})$$

where P_n^m is the normalized associated Legendre function of the first kind defined in Platzman, 1962, where $P_n^{-m} = P_n^m$. In practice, the streamfunction data were expanded in the real domain as (Kruse, 1983)

$$\psi(\lambda,\phi,t) = \sum_{m=0}^{15} \sum_{n=m+1}^{16} \{A_n^{m,o}(t) \cos m\lambda + A_n^{m,1}(t) \sin m\lambda\} \sqrt{2-\delta_{om}}\,(-1)^m P_n^m(\phi) \qquad \text{(A.2)}$$

where the real and complex coefficients are related by

$$\psi_n^m = \begin{cases} \frac{(-1)^m}{\sqrt{2}} \left(A_n^{m,o} - iA_n^{m,1}\right) & , \quad m > 0 \\ A_n^{m,o} & , \quad m = 0 \end{cases} \tag{A.3}$$

2. The EOF's

The EOF calculation is based on 10-day averaged values of the real spectral coefficients (A.2). Each year is divided into the 36 time periods shown in Table A1. The climatological seasonal cycle is defined as

$$\underset{\sim}{\psi}_j^s = \frac{1}{10} \sum_{k=1}^{10} \hat{\underset{\sim}{\psi}}_{kj} \tag{A.4}$$

where $\hat{\underset{\sim}{\psi}}_{kj}$ is the 10 day averaged (135 × 1) vector of real streamfunction coefficients for the kth year (1-10) and the jth period (1-36). Deviations from the seasonal cycle are computed as

$$\underset{\sim}{\psi}_{kj} = \hat{\underset{\sim}{\psi}}_{kj} - \underset{\sim}{\psi}_j^s \tag{A.5}$$

Note that

$$\sum_{j} \sum_{k=1} \underset{\sim}{\psi}_{kj} = 0 \qquad \text{(A.6)}$$

where the sum over j refers to an arbitrary interval of the year (see Table A1).

The real winter EOF's are the (135 × 1) eigenvectors of the covariance matrix

$$C = \frac{1}{10 \times 12} \Psi \Psi^{T} \qquad \text{(A.7)}$$

where $(\ )^{T}$ denotes a transpose and the number of periods within a year is 12 for the winter season (Dec. 2 - March 31). Ψ is the (135 × 120) matrix of anomaly vectors defined in (A.5). The eigenvector/value computations were done in double precision using routines found in the International Mathematical and Statistical Libraries (IMSL).

With the use of (A.3), the real EOF's ($\underset{\sim}{x}_i$) computed from (A.7) may be related to the complex EOF's ($\underset{\sim}{e}_i$) by

$$\underset{\sim}{e}_i = T \, \underset{\sim}{x}_i \qquad \text{(A.8)}$$

where T is the unitary matrix

Table A1. Time averaging interval used to develop the basic data set employed in the EOF computations. The winter EOF's are based on time periods 1-9 and 34-36 of each year.

Time Period	# of days	Beginning date (00Z)	Ending date (12Z)
1	10	Jan 1	Jan 10
2	10	Jan 11	Jan 20
3	10	Jan 21	Jan 30
4	10	Jan 31	Feb 9
5	10	Feb 10	Feb 19
6	10 (11 on	Feb 20	Mar 1
7	10 leap yr)	Mar 2	Mar 11
8	10	Mar 12	Mar 21
9	10	Mar 22	Mar 31
10	10	Apr 1	Apr 10
11	10	Apr 11	Apr 20
12	10	Apr 21	Apr 30
13	10	May 1	May 10
14	10	May 11	May 20
15	10	May 21	May 30
16	10	May 31	Jun 9
17	11	Jun 10	Jun 20
18	11	Jun 21	Jul 1
19	11	Jul 2	Jul 12
20	11	Jul 13	Jul 23
21	11	Jul 24	Aug 3
22	10	Aug 4	Aug 13
23	10	Aug 14	Aug 23
24	10	Aug 24	Sep 2
25	10	Sep 3	Sep 12
26	10	Sep 13	Sep 22
27	10	Sep 23	Oct 2
28	10	Oct 3	Oct 12
29	10	Oct 13	Oct 22
30	10	Oct 23	Nov 1
31	10	Nov 2	Nov 11
32	10	Nov 12	Nov 21
33	10	Nov 22	Dec 1
34	10	Dec 2	Dec 11
35	10	Dec 12	Dec 21
36	10	Dec 22	Dec 31

$$
\begin{bmatrix}
\frac{(-1)^{m_{\alpha_1}}}{\sqrt{2}} & \frac{i(-1)^{m_{\alpha_1}+1}}{\sqrt{2}} & & & & & 0 \\
\frac{(-1)^{m_{\alpha_1}}}{\sqrt{2}} & \frac{i(-1)^{m_{\alpha_1}}}{\sqrt{2}} & & & & & \\
 & & \frac{(-1)^{m_{\alpha_2}}}{\sqrt{2}} & \frac{i(-1)^{m_{\alpha_2}+1}}{\sqrt{2}} & & & \\
 & & \frac{(-1)^{m_{\alpha_2}}}{\sqrt{2}} & \frac{i(-1)^{m_{\alpha_2}}}{\sqrt{2}} & & & \\
 & & & & \ddots & & \\
 & 0 & & & & 1 & \\
 & & & & & & 1
\end{bmatrix}
\tag{A.9}
$$

The elements of the real EOF's have been arranged in a sequence of the cosine/sine coefficients with the (m = 0) cosine coefficients occurring last.

3. EOF model coefficients

For each element of $\underset{\sim}{e}_i$, (A.8) may be written more explicitly as

$$e_i(\gamma) = \sum_{\ell} t_{\gamma\ell} x_i(\ell) \qquad \text{(A.10)}$$

where $t_{\gamma\ell}$ are the elements of (A.9). The computation of the EOF model coefficients is based on the real versions of (3.2.4) which are determined by substitution of (A.10).

As an example, the real form of (3.2.4a) is

$$a_{kj} = \sum_{\ell} x_k(\ell)\, x_j(\ell) c_\ell \qquad \text{(A.11)}$$

where $c_\ell = n_\ell(n_\ell + 1)$. The real form of (3.2.4f) is

$$g_{kj} = \sum_{\substack{\ell=1 \\ (\ell \text{ odd})}}^{127} \{x_k(\ell)\, x_j(\ell+1) - x_k(\ell+1)\, x_j(\ell)\} m_\ell \qquad \text{(A.12)}$$

and the real version of (3.2.4c) is

$$d_{kji} = \frac{1}{2} \sum_{\ell} \sum_{\ell'} \sum_{\substack{\ell'' \\ \ell'' > \ell'}} \{x_k(\ell)\, x_i(\ell')\, x_j(\ell'') + x_k(\ell)\, x_i(\ell'')\, x_j(\ell')\} I_{\ell\ell'\ell''} \qquad \text{(a.13)}$$

where

$$I_{\ell\ell'\ell''} = i\bar{t}_{\ell}\, t_{\ell'}\, t_{\ell''}(c_{\ell''} - c_{\ell'})\{sl_{\ell\ell'\ell''}L_{\ell\ell'\ell''}$$

$$+s2_{\ell\ell'\ell''}L_{\ell\ell'\ell''} + s3_{\ell\ell'\ell''}L_{\ell''\ell\ell'}\} \qquad \text{(A.14)}$$

The subscript γ in $t_{\gamma\ell}$ has been dropped since the sums in (A.13) involve only positive m. $L_{\ell\ell'\ell''}$ is computed in double precision from formulas given in Silberman (1954) and

$$sl_{\ell\ell'\ell''} = 1 - (-1)^{is_{\ell}+is_{\ell'}+is_{\ell''}}(1 - \delta_{om_{\ell}})$$

$$(1 - \delta_{om_{\ell'}})(1 - \delta_{om_{\ell''}}) \qquad \text{(A.15a)}$$

$$s2_{\ell\ell'\ell''} = (-1)^{is_{\ell''}}(1 - \delta_{om_{\ell''}})$$

$$- (-1)^{is_{\ell}+is_{\ell'}}(1 - \delta_{om_{\ell}})$$

$$(1 - \delta_{om_{\ell'}}) \qquad \text{(A.15b)}$$

$$s3_{\ell\ell'\ell''} = (-1)^{is_{\ell'}}(1 - \delta_{om_{\ell'}})$$

$$- (-1)^{is_{\ell}+is_{\ell''}}(1 - \delta_{om_{\ell}})$$

$$(1 - \delta_{om_{\ell''}}) \qquad \text{(A. 15c)}$$

where

$$is = \begin{cases} 1 \ , \text{ sine term} \\ 0 \ , \text{ cosine term} \end{cases}$$

and

$$\delta_{om_\ell} = \begin{cases} 1 \ , \ m_\ell = 0 \\ 0 \ , \text{ otherwise} \end{cases} .$$

The sum in (A.13) involves 56,664 terms for the case of triangular truncation at total wave number 16 limited to the odd harmonics.

B. Identities of the EOF coefficients

1. Symmetry of a_{kj}

$$a_{jk} = \sum_\gamma c_\gamma \, \bar{e}_j(\gamma) \, e_k(\gamma) = \sum_\gamma c_{\bar{\gamma}} \, e_j(\bar{\gamma}) \, \bar{e}_k(\bar{\gamma})$$

$$= \sum_\gamma c_\gamma \, e_j(\gamma) \, \bar{e}_k(\gamma) = a_{kj}$$

where use was made of the fact that $\bar{e}_k(\gamma) = e_k(\bar{\gamma})$ and $c_{\bar{\gamma}} = c_\gamma$.

2. Symmetry of u_{kj}

These coefficients may be rewritten as

$$u_{kj} = \sum_{\gamma} r_1(\gamma)\ e_j(\gamma)\ \bar{e}_k(\gamma)$$

$$+ \sum_{\gamma} r_2(\gamma^+)\ e_j(\gamma^{++})\ \bar{e}_k(\gamma) + e_k(\gamma^{++})\ \bar{e}_j(\gamma)$$

Since $r_1(\bar{\gamma}) = r_1(\gamma)$, it follows from B1 that $u_{kj} = u_{jk}$.

3. Antisymmetry of g_{kj}

$$g_{jk} = i \sum_{\gamma} m_\gamma\ \bar{e}_j(\gamma)\ e_k(\gamma) = i \sum_{\gamma} m_{\bar{\gamma}}\ \bar{e}_j(\bar{\gamma})\ e_k(\bar{\gamma})$$

$$= -i \sum_{\gamma} m_\gamma\ e_j(\gamma)\ \bar{e}_k(\gamma)$$

$$= -g_{kj} \qquad \text{(note that } m_{\bar{\gamma}} = -m_\gamma\text{)}$$

4. Properties of the EOF interaction coefficients

In the following derivations, it is necessary to make use of the redundancy relations of the coupling integrals, $L_{\gamma\beta\alpha}$. These are (see Platzman, 1962)

$$L_{\gamma\beta\alpha} = -L_{\gamma\alpha\beta} \tag{B.1a}$$

$$L_{\gamma\bar{\beta}\alpha} = L_{\alpha\beta\gamma} \tag{B.1b}$$

$$L_{\gamma\beta\bar{\alpha}} = L_{\beta\gamma\alpha} \tag{B.1c}$$

Let $L^*_{\gamma\beta\alpha} = i\, L_{\gamma\beta\alpha}$ and $I_{\gamma\beta\alpha} = (c_\beta - c_\alpha)\, L^*_{\gamma\beta\alpha}$. It follows from (B.1a) that $I_{\gamma\beta\alpha} = I_{\gamma\alpha\beta}$.

(i) Symmetry of d_{kji}

$$d_{kij} = \frac{1}{2} \sum_{\gamma} \sum_{\alpha} \sum_{\beta} \bar{e}_k(\gamma)\, e_i(\beta)\, e_j(\alpha)\, I_{\gamma\beta\alpha}$$

$$= \frac{1}{2} \sum_{\gamma} \sum_{\alpha} \sum_{\beta} \bar{e}_k(\gamma)\, e_i(\alpha)\, e_j(\beta)\, I_{\gamma\alpha\beta} = d_{kji}$$

(ii) $d_{kji} + d_{jki} + d_{ijk} = 0$

Following a development similar to that of Platzman (1960) d_{kji} may be written as

$$d_{kji} = -\frac{1}{2} \sum_{\gamma} \sum_{\beta} \bar{e}_k(\gamma) \sum_{\alpha} c_\alpha L^*_{\gamma\beta\alpha} \{e_i(\beta)\, e_j(\alpha) + e_i(\alpha)\, e_j(\beta)\} \tag{B.2}$$

Let

$$Q_{\gamma\beta j} = \sum_{\alpha} c_{\alpha}\ e_j(\alpha)\ L^*_{\gamma\beta\alpha} \tag{B.3}$$

where

$$Q_{\gamma\beta j} = -\ Q_{\overline{\beta\gamma} j} \tag{B.4}$$

since from (B.1)

$$L_{\overline{\gamma\beta}\alpha} = -\ L_{\beta\gamma\alpha} \tag{B.5}$$

Then

$$d_{kji} = -\ \frac{1}{2} \sum_{\gamma} \sum_{\beta} D_{\gamma\beta kij} + D_{\gamma\beta kji} \tag{B.6}$$

where

$$D_{\gamma\beta kji} \equiv \bar{e}_k(\gamma)\ e_j(\beta)\ Q_{\gamma\beta i} \tag{B.7}$$

and from (B.4)

$$D_{\overline{\gamma\beta} kji} = -\ D_{\beta\gamma jki} \tag{B.8}$$

Therefore

$$d_{kji} + d_{jki} + d_{ijk} = -\frac{1}{2}\sum_{\gamma}\sum_{\beta}(D_{\gamma\beta kij} + D_{\gamma\beta kji} + D_{\gamma\beta jik} + \underbrace{D_{\gamma\beta jki}}_{-D_{\overline{\beta\gamma}kji}} + \underbrace{D_{\gamma\beta ikj}}_{-D_{\overline{\beta\gamma}kij}} + \underbrace{D_{\gamma\beta ijk}}_{-D_{\overline{\beta\gamma}jik}})$$

$$= 0$$

5. Antisymmetry of rl_{kj}

Let

$$M_{\gamma\beta} = \sum_{\alpha} (-c_{\alpha}\psi_{\alpha}^{s})\ L^{*}_{\gamma\beta\alpha} \qquad (B.9)$$

where, from (B.5)

$$M_{\gamma\beta} = -M_{\overline{\beta\gamma}} \qquad (B.10)$$

Then

$$rl_{kj} = \sum_{\gamma}\sum_{\beta} F_{\gamma\beta kj} \qquad (B.11)$$

where

$$F_{\gamma\beta kj} = \bar{e}_k(\gamma)\ e_j(\beta)\ M_{\gamma\beta} \tag{B.12}$$

and

$$F_{\gamma\beta kj} = -\ F_{\overline{\beta\gamma}jk} \tag{B.13}$$

Therefore

$$rl_{jk} = \sum_{\gamma}\sum_{\beta} F_{\gamma\beta jk} = -\sum_{\gamma}\sum_{\beta} F_{\overline{\beta\gamma}kj}$$

$$= -\sum_{\gamma}\sum_{\beta} F_{\gamma\beta kj}$$

$$= -rl_{kj}$$

6. Antisymmetry of the simplified orography

If the advection of planetary vorticity by the divergent wind is neglected and a constant coriolis parameter is assumed, (3.1.4) simplifies to $f_0 = \sin\phi_0$ and term D of (3.2.3) becomes $M'\sum_j z_j\ f'_{kj}$ where

$$f'_{kj} = \sum_{\gamma}\sum_{\alpha}\sum_{\beta} h_\alpha\ \bar{e}_k(\gamma)\ e_j(\beta)\ L^*_{\gamma\beta\alpha} \tag{B.14a}$$

and

$$M' = a\, f_0/H^* \qquad \text{(B.14b)}$$

The antisymmetry of (B.14a) folows from B5 by substituting h_α for $(-c_\alpha \psi^s_\alpha)$.

C. Conservative properties of the EOF model

Unlike the spectral model, the EOF model does not, in general, conserve both energy and enstrophy for arbitrary model truncations. In the following, two alternative model formulations are given: one approach conserves enstrophy but not energy and the other, based on a diagonal form of the tendency term, conserves neither property. When all of the EOF's are included both energy and enstrophy are conserved, independent of the model formulation.

1. Enstrophy conserving formulation

The spectral model with only the nonlinear and beta terms is

$$c_\gamma \dot{\psi}_\gamma = \frac{i}{2} \sum_\alpha \sum_\beta \psi_\alpha \psi_\beta (c_\beta - c_\alpha) L_{\gamma\beta\alpha} + i m_\gamma \psi_\gamma \qquad \text{(C.1)}$$

Multiplying by c_γ and expanding (C.1) in terms of EOF's leads to

$$\sum_j b_{kj}\,\dot{z}_j = \sum_i \sum_j z_i\, z_j\, d'_{kji} + \sum_j z_j\, g'_{kj} \qquad (C.2)$$

where b_{kj} is given in (3.2.8d),

$$d'_{kji} = \sum_\gamma \sum_\beta \sum_\alpha c_\gamma\, \frac{i}{2}(c_\beta - c_\alpha)\, \bar{e}_k(\gamma) e_j(\beta) e_i(\alpha) L_{\gamma\beta\alpha} \qquad (C.3)$$

and

$$g'_{kj} = \sum_\gamma c_\gamma im_\gamma\, \bar{e}_k(\gamma)\, e_j(\gamma) \qquad (C.4)$$

The enstrophy (ENS) tendency is

$$\begin{aligned}\frac{1}{2}\frac{d}{dt}(\mathrm{ENS}) &= \sum_k z_k \sum_j b_{kj}\,\dot{z}_j \\ &= \sum_k z_k \{\sum_i \sum_j z_i\, z_j\, d'_{kji} \\ &\quad + \sum_j z_j\, g'_{kj}\} \qquad (C.5)\end{aligned}$$

In the following, it is shown that d'_{kji} and g'_{kj} satisfy the same properties as d_{kji} and g_{kj}, respectively, and therefore the ENS tendency is zero.

(i) Symmetry of d_{kji}

This follows directly from B4i.

(ii) $d'_{kji} + d'_{jki} + d'_{ijk} = 0$

Rewrite d'_{kji} as

$$d'_{kji} = -\frac{1}{2} \sum_{\gamma} \sum_{\alpha} c_\gamma c_\alpha \bar{e}_k(\gamma) \sum_{\beta} L^*_{\gamma\beta\alpha} \{e_j(\beta)\ e_i(\alpha) + e_j(\alpha)\ e_i(\beta)\} \qquad (C.6)$$

Let

$$Q'_{\gamma\alpha j} = \sum_{\beta} e_j(\beta) L^*_{\gamma\beta\alpha} \qquad (C.7)$$

where

$$Q'_{\overline{\gamma\alpha}j} = - Q'_{\alpha\gamma j} \qquad (C.8)$$

since from (B.1)

$$L^*_{\overline{\gamma\beta\alpha}} = - L^*_{\alpha\beta\gamma} \qquad (C.9)$$

Then

$$d'_{kji} = -\frac{1}{2}\sum_{\gamma}\sum_{\alpha} c_\gamma c_\alpha \{D'_{\gamma\alpha kji} + D'_{\gamma\alpha kij}\} \qquad (C.10)$$

where

$$D'_{\gamma\alpha kji} = \bar{e}_k(\gamma)\ Q'_{\gamma\alpha j}\ e_i(\alpha) \qquad (C.11)$$

and

$$D'_{\overline{\gamma\alpha}kji} = -D'_{\alpha\gamma ijk} \qquad (C.12)$$

Therefore

$$d'_{kji} + d'_{jki} + d'_{ijk} =$$

$$= -\frac{1}{2}\sum_{\gamma}\sum_{\alpha}(c_\gamma c_\alpha D'_{\gamma\alpha kji} + c_\gamma c_\alpha D_{\gamma\alpha kij}$$

$$+ c_\gamma c_\alpha D_{\gamma\alpha jki}$$

$$+ c_\gamma c_\alpha \underbrace{D_{\gamma\alpha jik}}_{-D_{\overline{\alpha\gamma}kij}} + c_\gamma c_\alpha \underbrace{D_{\gamma\alpha ijk}}_{-D_{\overline{\alpha\gamma}kji}} + c_\gamma c_\alpha \underbrace{D_{\gamma\alpha ikj}}_{-D_{\overline{\alpha\gamma}jki}}) = 0$$

(iii) Antisymmetry of g_{kj}

This follows directly from (B.3) since $c_{\bar{\gamma}} = c_{\gamma}$.

2. Model formulation with a diagonal tendency term

Next it is shown that when the tendency term is diagonal neither energy or enstrophy are identically conserved unless all the EOF's are allowed in the model.

Let

$$v_{kj} = \sum_{\gamma} c_{\gamma}^{t} \bar{e}_{k}(\gamma)\ e_{j}(\gamma) \tag{C.13}$$

Then

$$\sum_{k}\sum_{j} v_{kj}\ z_{k}\ z_{j} = \begin{cases} \text{MSV} , & t = 1 \\ \text{ENS} , & t = 2 \end{cases} \tag{C.14}$$

The spectral model is written as

$$\dot{\psi}_{\gamma} = \frac{1}{2c_{\gamma}} \sum_{\alpha}\sum_{\beta} \psi_{\alpha}\ \psi_{\beta}(c_{\beta} - c_{\alpha})L_{\gamma\beta\alpha} + i\,\frac{m_{\gamma}}{c_{\gamma}}\,\psi_{\gamma} \tag{C.15}$$

Then

$$\dot{z}_{k} = \sum_{i}\sum_{j} z_{i}\ z_{j}\ d'''_{kji} + \sum_{j} z_{j}\ g'''_{kj} \tag{C.16}$$

where

$$d''_{kji} = \sum_{\gamma} \sum_{\beta} \sum_{\alpha} \bar{e}_k(\gamma)\ e_i(\alpha)\ e_j(\beta)\ \frac{c_\beta - c_\alpha}{c_\gamma}\ L_{\gamma\beta\alpha} \qquad (C.17)$$

and

$$g''_{kj} = \sum_{\gamma} \frac{im_\gamma}{c_\gamma}\ \bar{e}_k(\gamma)\ e_j(\gamma) \qquad (C.18)$$

One half the tendency of (C.14) is

$$\sum_j z_j \sum_k v_{kj} \dot{z}_k = \sum_j \sum_r \sum_s z_j\ z_r\ z_s \sum_k v_{kj} d''_{ksr}$$

$$+ \sum_s \sum_j z_k\ z_s \sum_k v_{kj}\ g''_{ks} \qquad (C.19)$$

where

$$\sum_k v_{kj}\ d''_{ksr}$$

$$= \sum_\alpha \sum_\beta (c_\beta - c_\alpha) e_s(\alpha)\ e_r(\beta) \sum_\gamma \sum_{\gamma'} \frac{c^t_\gamma}{c_{\gamma'}}\ \bar{e}_j(\gamma)$$

$$L_{\gamma'\beta\alpha} \sum_k e_k(\gamma)\ \bar{e}_k(\gamma') \qquad (C.20)$$

and if all the EOF's are included (see (2.2.12b))

$$\sum_k e_k(\gamma)\ \bar{e}_k(\gamma') = \delta_{\gamma\gamma'} \tag{C.21}$$

Therefore

$$\sum_k v_{kj}\ d'_{ksr} = \begin{cases} d_{jsr} \text{ (as in B4)} & \text{if } t = 1 \\ d'_{jsr} \text{ (as in C1)} & \text{if } t = 2 \end{cases} \tag{C.22}$$

And finally

$$\sum_k v_{kj}\ g'_{ks} = \sum_\gamma \sum_{\gamma'} \frac{c^t_\gamma}{c_{\gamma'}}\ \bar{e}_j(\gamma)\ e_s(\gamma')\ im_{\gamma'} \sum_k e_k(\gamma)$$

$$\bar{e}_k(\gamma') \tag{C.23}$$

If all the EOF's are included

$$\sum_k v_{kj}\ g'_{ks} = \begin{cases} g_{js} \text{ (as in B3)} & \text{if } t = 1 \\ g'_{js} \text{ (as in C1)} & \text{if } t = 2 \end{cases} \tag{C.24}$$

It follows that both the energy (MSV) and ENS tendencies are identically zero only when all the EOF's are allowed in the model.

D. A technique for finding steady state solutions to special nonlinear systems

The search for solutions outlined in 4.3ci is only feasible if the ellipsoid of zero kinetic energy (KE) tendency is confined to a reasonably small volume of

phase space. In the following, a procedure is given which, for an arbitrary model truncation, provides the minimum value of κ that insures the surface of zero KE tendency is bounded (forms an elllipsoid) inside of which the KE tendency is positive and outside of which the KE tendency is negative. Furthermore, a method is outlined which provides a seemingly reasonable value of the frictional decay rate (κ_r) by reducing the volume of the zero KE tendency ellipsoid to a specified fraction of the volume of the constant MSV ellipsoid determined from the observations.

1. Choosing the frictional decay rate to insure that P_s is positive definite

From (4.3.9)

$$(\underset{\sim}{z} - \underset{\sim}{q})^T P_s (\underset{\sim}{z} - \underset{\sim}{q}) = \underset{\sim}{q}^T P_s \underset{\sim}{q} \qquad \text{(D.1)}$$

where

$$P_s = \kappa A - R_s \qquad \text{(D.2a)}$$

and

$$\underset{\sim}{q} = \frac{\alpha}{2} P_s^{-1} \underset{\sim}{z}^* \qquad \text{(D.2b)}$$

Since A is positive definite and R_s is symmetric, there exists a nonsingular matrix U (see Bellman, 1960, pp. 58-59) such that

$$U^T P_s U = \kappa I - \Lambda^* \qquad (D.3)$$

where Λ^* is a diagonal matrix of the generalized eigenvalues determined from

$$\det(R_s - \lambda_i^* A) = 0 \qquad (D.4)$$

If κ is chosen to be greater than the maximum λ_i^*, $U^T P_s U$ is positive definite. Since U may be written as a product of unitary and positive definite matrices (Bellman, 1960) it follows that P_s is also positive definite. As κ is reduced in magnitude so that it approaches max (λ_i^*), the smallest eigenvalue of $U^T P_s U$ approaches zero and, therefore, P_s also becomes singular.

2. A frictional decay rate (κ_r) based on energy constraints

The ellipsoid of zero KE tendency (D.1) may be written in the standard form

$$\frac{y_1^2}{b_1^2} + \frac{y_2^2}{b_2^2} + \ldots + \frac{y_N^2}{b_N^2} = 1 \qquad (D.5)$$

where

$$b_i = (\underset{\sim}{f}^T P_s \underset{\sim}{f}/\mu_i)^{\frac{1}{2}} \qquad (D.6)$$

$$\underset{\sim}{f} = \frac{\alpha}{2} P_s^{-1} \underset{\sim}{z}^* \qquad (D.7)$$

and the μ_i are the eigenvalues of P_s.

The ellipsoid of constant MSV of the observations is

$$\underset{\sim}{z}^T A \underset{\sim}{z} = \sum_k a_{kk} \lambda_k \equiv c_0 \qquad (D.8)$$

or

$$\frac{v_1^2}{d_1^2} + \frac{v_2^2}{d_2^2} + \ldots + \frac{v_N^2}{d_N^2} = 1 \qquad (D.9)$$

where

$$d_i = \sqrt{\frac{c_0}{\mu_i^*}} \qquad (D.10)$$

The λ_k are the variances of the data PC's, the μ_i^* are the eigenvalues of A, and $\underset{\sim}{z} = T \underset{\sim}{v}$, where T is the matrix

of eigenvectors of A.

In order to obtain a reasonable bound on the ellipsoid of zero KE, the ratio of the volumes of (D.5) and (D.9) are constrained so that

$$\prod_{i=1}^{N} b_i / \prod_{i=1}^{N} d_i = \gamma \tag{D.11}$$

or

$$\frac{\sum_{i=1}^{N} L_i^2/\kappa-\lambda_i^*}{\sum_{i=1}^{N} (\kappa-\lambda_i^*)^{\frac{1}{2}}} = 4c_0\gamma^{2/N} \tag{D.12}$$

where the λ_i^* are the generalized eigenvalues given in (D.4) and

$$\underset{\sim}{L} = \alpha U^T \underset{\sim}{z^*} \tag{D.13}$$

After some experimentation, γ was chosen to be 0.5. This value seemed to result in a reasonable size of the zero KE tendency ellipsoid relative to the observed MSV. The solution (κ_r) was determined numerically by re-writing (D.12) in the form $f(\kappa) = 0$ and decreasing κ from the value found in D1 until a sign change occurred. The final solution was determined by an algorithm found in IMSL (zbrent).

3. Discretization of the zero KE tendency ellipsoid

The search of the ellipsoid (D.5) is conducted over the points in the y_1 direction defined by

$$y_1 = \frac{M_1 - k_1}{M_1} b_1 \qquad \text{(D.14)}$$

where $k_1 \in 0, 1, 2, \ldots, 2M_1$, and M_1 is the number of gridpoints along the b_1 semiaxis (excluding the origin). For each y_1, the points along the successive axes are then

$$y_j = \frac{M_1 - k_j}{M_1} b_j \qquad \text{(D.15)}$$

where

$$k_j \in \begin{cases} M_j, M_j+1, \ldots, 2M_1-M_j & \text{for } 2 \leq j < N \\ M_j, 2M_1-M_j & \text{for } j = N \end{cases} \qquad \text{(D.16a)}$$

and

$$M_j = M_1 - \left(M_1^2 - \sum_{i=1}^{j-1} (M_1 - k_i)^2\right)^{\frac{1}{2}} \qquad \text{(D.16b)}$$

BIBLIOGRAPHY

Baines, P.G., 1976: The stability of planetary waves on a sphere. J. Fluid Mech., 73, 193-213.

Beers, Y., 1957: Introduction to the Theory of Error. Addision-Welsey, 66 pp.

Bellman, R., 1960: Introduction to Matrix Analysis. McGraw-Hill, 328 pp.

Bengtsson, L., 1981: Review of recent progress made in medium range weather forecasting. Problems and prospects in long and medium range weather forecasting. ECWMF Seminar, September 14-18.

Bodewig, E., 1959: Matrix Calculus. North-Holland Publishing Company, Amsterdam, 452 pp.

Brezowsky, H., H. Flohn and P. Hess, 1951: Some remarks on the climatology of blocking action. Tellus, 3, 191-194.

Bryson, R.A. and J.F. Lahey, 1958: The march of the seasons. Final Report, Contract AF 19-(604)-992, Dept. of Meteor., University of Wisconsin, March 1958.

Charney, J. and J. DeVore, 1979: Multiple flow equilibria in the atmosphere and blocking. J. Atmos. Sci., 36, 1205-1216.

Davis, R.E., 1976: Predictability of sea surface temperature and sea level pressure anomalies over the North Pacific Ocean. J. Phys. Oceanogr., 6, 249-266.

Draper, N.R. and H. Smith, 1966: Applied Regression Analysis. John Wiley and Sons, 407 pp.

Eliasen, E. and B. Machenhauer, 1969: On the observed large-scale atmospheric wave motions. Tellus, 21, 149-165.

Fechner, H. 1981: Klimatologie des Geopotentials der 500 mb-Fläche der Nordhalbkugel unter Verwendung

von natürlichen Orthogonalfunctionen in Wellenzahlenbereich. Internal Report, Institut für Meereskunde an der Universität Kiel, Abt. Meteorologie.

Frederiksen, J.S., 1982: A unified three-dimensional instability theory of the onset of blocking and cyclogenesis. J. Atmos. Sci., 39, 969-982.

Haltiner, G.J. and R.T. Williams, 1980: Numerical Prediction and Dynamic Meteorology. John Wiley and Sons, 477 pp.

Hartmann, D. and S. Ghan, 1980: A statistical study of the dynamics of blocking. Mon. Wea. Rev., 108, 1144-1159.

Holopainen, E.O. and A.H. Oort, 1981: On the role of large-scale transient eddies in the maintenance of the vorticity and enstrophy of the time-mean atmospheric flow. J. Atmos. Sci., 38, 270-280.

Holton, J.R., 1972: An Introduction to Dynamic Meteorology. Academic Press, 319 pp.

Jeckström, W., 1977: Eine Entwicklung des Geopotentialfeldes der 500 mb-Fläche im Winter der Nordhalbkugel in natürliche Orthogonalfunktionen und eine Interpretation der Ergebnisse im Zusammenhang mit tatsächlichen synoptischen grosskaligen Wetterlagen. Internal Report, Institut für Meereskunde an der Universität Kiel, Abt. Maritime Meteorologie.

Källén, E., 1981: The nonlinear effects of orographic and momentum forcing in a low-order, barotropic model. J. Atmos. Sci., 38, 2150-2163.

Kruse, H., 1983: A statistical-dynamical low-order spectral model for tropospheric flows. Hamburger Geophysikalische Einzelschriften, Max-Planck-Institut für Meteorologie in Hamburg.

Kutzbach, J.E., 1967: Empirical eigenvectors of sea-level pressure, surface temperature and precipitation complexes over North America. J. Appl. Meteor., 6, 791-802.

Kutzbach, J.E., 1970: Large-scale features of monthly mean Northern Hemisphere anomaly maps of sea-level pressure. Mon. Wea. Rev., 98, 708-716.

Lau, N-C., 1981: A diagnostic study of recurrent meteorological anomalies appearing in a 15-year simulation with a GFDL general circulation model. Mon. Wea. Rev., 109, 2287-2311.

Lorenz, E.N., 1972: Barotropic instability of Rossby wave motion. J. Atmos. Sci., 29, 258-264.

Lorenz, E.N., 1980: Attractor sets and quasi-geostrophic equilibrium. J. Atmos. Sci., 37, 1685-1699.

McWilliams, J.C., 1980: An application of equivalent modons to atmospheric blocking. Dyn. Atmos. Oceans, 5, 43-66.

Namias, J., 1950: The index cycle and its role in the general circulation. J. of Meteor., 7, 130-139.

North, G.R. and R.F. Cahalan, 1981: Predictability in a solvable stochastic climate model. J. Atmos. Sci., 38, 504-513.

North, G.R., T.L. Bell, R.F. Cahalan and F.J. Moeng, 1982: Sampling errors in the estimation of empirical orthogonal functions. Mon. Wea. Rev., 110, 699-706.

Platzman, G.W., 1960: The spectral form of the vorticity equation. J. Meteor., 17, 635-644.

Platzman, G.W., 1962: The analytic dynamics of the spectral vorticity equation. J. Atmos. Sci., 19, 313-328.

Preisendorfer, R.W., F.W. Zwiers and T.P. Barnett, 1981: Foundations of Principal Component Selection Rules. SIO reference series #81-4.

Rinne, J. and V. Karhila, 1975: A spectral barotropic model in horizontal empirical orthogonal functions. Quart. J. R. Met. Soc., 101, 365-382.

Rinne, J., V. Karhila and S. Järvenoja, 1981: The EOF's of the 500 mb height in the extratropics of the Northern Hemisphere. Internal Report, Dept. of Meteorology, University of Helsinki.

Sellers, W.D., 1957: A statistical-dynamic approach to numerical weather prediction. Scientific Report No. 2, Statistical Forecasting Project, MIT.

Silberman, I., 1954: Planetary waves in the atmosphere. J. of Meteor., 11, 27-34.

Simmons, A.J., J.M. Wallace and G.W. Branstator, 1982: Barotropic wave propagation and instability, and atmospheric teleconnection patterns. Unpublished manuscript.

Wallace, J.M. and R.E. Dickinson, 1972: Empirical orthogonal representation of time series in the frequency domain. Part I: Theoretical considerations. J. Appl. Meteor., 11, 887-892.

Wallace, J.M. and D.S. Gutzler, 1981: Teleconnections in the geopotential height field during the Northern Hemisphere Winter. Mon. Wea. Rev., 109, 784-812.

Weickmann, K.M., 1982: Intraseasonal fluctuations in near-global-scale modes of circulation and outgoing longwave radiation during Northern Hemisphere winter. Ph.D. Dissertation, Department of Meteorology, Center for Climatic Research, University of Wisconsin-Madison, 107 pp.

Young, J.A., 1968: Comparative properties of some differencing schemes for linear and nonlinear oscillations. Mon. Wea. Rev., 96, 357-364.

Acknowledgments

I wish to thank Gerald Herman for his help and guidance throughout this study. I had many helpful discussions with John Young, particularly in regard to the normal mode analysis. John Kutzbach helped to clarify some aspects of the use of EOF's in a model and Klaus Weickmann helped me greatly with the interpretation of the EOF's. Much of this work was started while visiting the Max-Planck-Institut für Meteorologie, in Hamburg. Klaus Hasselmann and Dirk Olbers suggested the use of EOF"s in a model. Harald Kruse helped me greatly with the spectral model formulation and also parovided the basic data set used in this study. I am grateful to Milton Halem and the staff of the modeling and simulation facility at Goddard Space Flight Center for providing the facilities and support needed to carry out this work.